

**INFLUENCE OF ELECTROMAGNETIC STIMULATION ON  
NEOCORTICAL NEURONS AND NETWORK: A  
SIMULATION BASED STUDY**

**WU TIE CHENG**

*(B. Eng. (Hons.), NUS)*

**A THESIS SUBMITTED**

**FOR THE DEGREE OF DOCTOR OF PHILOSOPHY**

**DEPARTMENT OF MECHANICAL ENGINEERING**

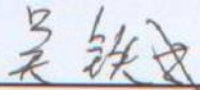
**NATIONAL UNIVERSITY OF SINGAPORE**

**2016**

## DECLARATION

I hereby declare that this thesis is my original work and it has been written by me in its entirety. I have duly acknowledged all the sources of information which have been used in the thesis.

This thesis has also not been submitted for any degree in any university previously.



---

Wu Tie Cheng

13/01/2016

## **Acknowledgement**

Foremost, I would like to express my sincere gratitude to my supervisor Prof. Lee Kim Seng for the continuous supervision of my Ph.D study and research. His patience and support helped me overcome many crisis situations and finish this dissertation. I could not have imagined having a better advisor and mentor for my Ph.D study.

Great thanks should be given to Prof Li Xiaoping, who has always been there to listen and give advice. I am deeply grateful to him for the long discussions that helped me sort out the technical details of my work. I am also thankful to him for carefully reading and commenting on countless revisions of my manuscripts.

Dr. Fan Jie's insightful comments and constructive advices at different stages of my study inspired many of my ideas in my research. In addition, I would like to acknowledge Dr. Yang Daoguo, Dr. Hao Weidong, Dr. Jiang Xin, Dr. Tan Jie, and Mr. Li Xiaoming for their contributions to the various experiments I have conducted.

I am also indebted to the members of the Neuroengineering Lab, who have kindly offered me their help and support. Particularly, I would like to acknowledge Dr. Shen Kaiquan, Dr. Rohit Tyagi, Dr. Bui Ha Duc, Dr. Yu Ke, Dr. Wang Yan, Dr. Ye Yan, Dr. Shao Shiyun, Dr. Khoa Weilong, Dr. Wang Yue, Dr. Ng Wu Chun, Mr. Ng Khoon Siong, Mr. Qu Di, Mr. Zheng Hao, and Mr. Li Zhe.

Special thanks should be given to my parents and my wife for their love and support throughout the years. Words are not enough to express what these have meant to me.

Finally, I want to thank NUS for the research scholarship granted to me.

## Table of Contents

Acknowledgement .....	i
Summary .....	vi
List of tables.....	ix
List of figures.....	x
List of abbreviations .....	xiii
Chapter 1 Introduction .....	1
1.1 Motivation.....	1
1.2 Research objectives.....	2
1.3 Thesis organization .....	3
Chapter 2 Literature review .....	5
2.1 EM stimulation for neurological disorders .....	5
2.1.1 Non-invasive stimulation .....	5
2.1.2 Invasive stimulation .....	8
2.1.3 Clinical application .....	9
2.2 Current understandings of EM stimulation .....	13
2.2.1 Direct measurement of neuronal activities.....	13
2.2.2 Motor cortex: cytoarchitecture and stimulation effectiveness .....	15
2.2.3 Motor threshold.....	17
2.2.4 Epidural recording of pyramidal tract .....	18
2.2.5 EEG and neuroimaging.....	21
2.3 Hypothesis on the working mechanism of EM stimulation .....	22
2.3.1 High resolution profile of electric field.....	22
2.3.2 Network model.....	24
2.3.3 Simulation of the biophysical interaction between neurons and electric field .....	28
2.3.4 Repertoire and drawbacks of existing models.....	32
Chapter 3. Simulation of membrane potential dynamics of neurons induced by EM stimulation.....	34
3.1 Mathematical formalization .....	34
3.2 Numerical computation.....	36
3.2.1 Solving the model with Crank-Nicolson method.....	36
3.2.2 Discretization – mathematical convergence and intracellular potential uniformity .....	37
3.3 Representation of the membrane.....	40

3.4 Segmentation and registration of axonal components .....	44
3.5 Measurement of stimulation thresholds and polarization lengths .....	46
CHAPTER 4 Measurement of responses of pyramidal cells to long-duration uniform field stimulation .....	48
4.1 Pyramidal cells .....	48
4.2 Stimulus orientation and duration .....	52
4.3 Statistical analysis .....	52
4.4 Results .....	53
4.4.1 Anisotropy of stimulation thresholds and polarization lengths .....	53
4.4.2 Locations of initiation points .....	55
4.4.3 Influence of cell type .....	56
4.4.4 Transmission of initiation points in association of pulse duration .....	56
4.4.4 Comparison of simulation results with in-vitro data .....	57
4.5 Discussion .....	58
4.5.1 Competition between activation-capable components .....	59
4.5.2 The initiation points .....	61
4.5.3 Verisimilitude of cable theory-based simulation .....	64
4.6 Concluding remarks .....	64
CHAPTER 5 Measurement of TMS thresholds and sensitivity to morphological features .....	66
5.1 Stimulation waveforms of commercially available device .....	66
5.2 Treatment of axon morphology .....	68
5.2.1 PCA based unravelling .....	68
5.2.2 Determination of orders of axon segments .....	70
5.2.3 Manipulation of diameter and synapses .....	70
5.2.4 Statistical analysis .....	70
5.3 Results .....	71
5.3.1 Thresholds of different configurations .....	71
5.3.2 Distinction among PCs .....	72
5.3.3 Sensitivity of thresholds to aborization and tortuosity .....	73
5.3.4 Influence of diameter and synapses .....	74
5.4 Discussion .....	75
5.4.1 LII/III pyramidal neurons .....	77
5.4.2 LV pyramidal neurons .....	77
5.4.3 Influence of cell morphology .....	78

5.5 Concluding remarks .....	80
Chapter 6 Responses of inhibitory neurons to EM stimulation .....	81
6.1 Nest basket cell morphology .....	81
6.2 Determination of axonal membrane properties .....	82
6.2.1 Membrane properties and ion channels.....	82
6.2.2 Search algorithm .....	86
6.2.3 Initialization of the population .....	86
6.2.4 Feature based error functions .....	87
6.2.5 Domination rank .....	88
6.2.6 Breeding of new individuals .....	90
6.2.7 Local search algorithm.....	92
6.3 Measurement of thresholds .....	93
6.4 Statistical analysis .....	93
6.5 Results.....	94
6.5.1 Reduction of feature errors by the search algorithm .....	94
6.5.2 Membrane properties of inhibitory neurons.....	96
6.5.3 Thresholds of the NBC .....	97
6.5.4 Correlation between threshold and ion channel conductances.....	97
6.5.5 Correlation between threshold and spiking features .....	98
6.5.6 Threshold anisotropy.....	98
6.6 Discussion.....	101
6.6.1 Validity of the optimization approach.....	101
6.6.2 Influence of membrane properties and ion channels on thresholds .....	102
6.6.3 Thresholds to paired stimulation.....	103
6.7 Concluding remarks .....	104
CHAPTER 7 Conclusion and recommendation for future work .....	105
7.1 Comparison with existing models.....	105
7.2 Contributions.....	107
7.3 Limitations .....	107
7.4 Conclusions.....	109
7.5 Recommendation for future works .....	110
References.....	112
List of publications .....	130

## Summary

Non-invasive electromagnetic stimulation has shown promising effects in treating neurological disorders, but its working mechanism is still largely unknown. Previous researches have adopted computer simulations to investigate the biophysical interactions between the applied electric field and the target cells. Notwithstanding the observations – the multitude of factors capable of changing the stimulation efficacy – derived from these models, a comprehensive examination of the reactions of neocortical cells towards electromagnetic stimulation is still lacking. To fill the knowledge gap, a novel numerical computation scheme was developed in the present study. The segmentation and registration of axonal components empowered the simulation with the capability to host realistic neuronal morphologies; the adapted physiological model, which comprised a detailed description of the membrane properties and the ion channels, enabled neurons from different categories to have spiking patterns highly coherent with *in vitro* recordings; employment of the dynamic discretization strategy ensured the simulation is mathematically and physically valid; the simulation was then applied on a number of pyramidal cells to investigate their responses to electric fields in the light of statistical analysis.

The results showed that the stimulation thresholds of neurons – the minimal field intensity to induce action potential firing – had limited anisotropy but a considerable sensitivity to stimulus duration. The type of the cell played an important role in the numerical value of the threshold. The initiation points were dispersed all over the neurons but were more frequently located at the terminals of the axonal segments. For simulation results from certain angles



and pulses where experiment data was available, a high affinity between the *in vitro* and *in silico* recordings was noted.

To relate the simulation results to real-life applications of neuromodulation, pulses of commercially available transcranial magnetic stimulation (TMS) device were emulated and administered on the simulated neurons. Via measurements of stimulation thresholds, it was revealed that different waveforms activated neurons in different phases but under the same mechanism – depolarization of the terminals of the axon shafts. Moreover, the normalized motor thresholds obtained in clinical trials were discovered to be coherent with the values from simulation, which further confirmed the validity of the modelling approach.

Sensitivity analysis was further conducted on cells with manipulated axonal morphologies. With reduced arborization or increased tortuosity, the susceptibility of cell was elevated to produce lower thresholds, as both features could effectively hinder the intracellular flow introduced by the external field. Increment of the diameters of all the cellular segments could render a similar effect.

In supplement to the pyramidal cells, the author also studied the reactions of inhibitory neurons. Absent were the membrane properties and ion channel densities, an genetic algorithm-based optimization strategy was deployed to explore the combinations of various parameters and to extract the most successful ones in reproducing the membrane potential dynamics of fast spiking inhibitory cells documented *in vitro*. The relatively higher thresholds appeared to acknowledge that interneurons were unlikely to be the targets of

direct kindling; indirect activation through synaptic transmission might be a more plausible explanation to the inhibitory effects induced by stimulation.

## List of tables

Table 1 Review on experimental trials of EM stimulation on mental disorders. Only the tests showing positive responses are listed. ....	9
Table 2 Review on experimental trials of EM stimulation on neurological disorders. ....	11
Table 3 Membrane properties of components of PC. N.A.: not applicable, i.e. the channel is not inserted to the specific segments. ....	44
Table 4 Summary of two types of PCs tested in the simulation. Standard deviations are enclosed in parentheses. a: curve index is calculated as the distance between the two ends of a segment divided by the overall length, and is used to quantify tortuosity. Differences between layers are evaluated with one-way ANOVA: * = $p < 0.05$ ; ** = $p < 0.01$ . ....	50
Table 5. Comparison of the present model and the existing ones. ....	106

## List of figures

- Figure 1 Schematic diagram of (a) TES (b) tDCS & (c) TMS. Note that although the physical setup of TES and tDCS are basically the same, the electric currents running through the electrodes are different. The former employs a brief yet tremendous current, which directly induces neuronal activations; while the latter applies a mild long-lasting current, which modifies the excitability but not the activity of the neurons..... 6
- Figure 2 Design of a typical TMS device. The circuit is shown in (a). The major variation on design lies under the “stimulating coil”. The most common coil used in clinical trials and academic studies is the (b) “figure of eight” coil.8
- Figure 3 Implementation of the computation scheme on PCs with realistic cell morphologies. For each tested neuron, its morphology is firstly segmented and registered to different categories, including the apical dendrites, basal dendrites, soma, axon initial segment, axon hillock, myelinated axon, and nodes of Ranvier. The compartment number in each segment is then determined in an iterative manner. In the end, the compartment numbers are applied, the ion channels and other membrane properties are attached according to their categories, and the stimulation response to a pulse with specific direction and waveform is documented..... 39
- Figure 4 Convergence and uniformity scores of a tested cell at the end of the iteration. The morphology of a L2/3 PC is superimposed on the extracellular potentials, which is plotted in false color. The discrepancies between the two sets of MPs are plotted in black, while the intracellular potentials, i.e. the sum of MPs obtained with baseline compartment number (blue trail) and extracellular potentials, are plotted in red, with the unit of mV. .... 40
- Figure 5 Registration of axonal compartments. Part of the axon morphology is depicted; the axon shaft is coloured in red; the DS axis of the cell is sketched in a dashed line near the shaft; orders of axon collaterals are labeled next to each segment. .... 45
- Figure 6 Simulation trials for threshold measurement..... 47
- Figure 7 Z direction artifacts on a L5 PC. The front view (a) and the side view (b) of a neuron are presented. Note that the various V shape turns into the Z-direction which can only be perceived in the side view but not the front view.49
- Figure 8 Thresholds and AP initiation points with respect to field directions. (a) & (b) depict the thresholds of L2/3 & L5 PCs respectively. Values obtained with idealised and realistic axons are colored in black and red. .... 53
- Figure 9 Thresholds, initiation points and AP waveforms. (a) Thresholds and corresponding initiation sites of a L2/3 PC with respect to different field orientations. The axonal and dendritic components are colored in red and grey respectively. The dynamic of MP of soma under 0° stimulation (red) is overlaid with the firing patterns under 30 pA current injection to soma (black). Note that reducing the current amplitude would only delay the onset of APs until no activation could be initiated; the doublet spiking pattern is always

preserved. (b) Overlay of spiking patterns induced by 0° stimulation and 50 pA current injection to soma. Note that the initiation point of 0° stimulation is also located at the cell body..... 54

Figure 10 AP initiation points. Constitutions of three categories of AP initiation points, namely terminal of axon collateral, terminal of shaft axon, and cell body, obtained from L2/3 and L5 PCs with realistic axons are plotted in (a) & (b) respectively..... 55

Figure 11 Stimulation thresholds of L2/3 (a) and L5 (b) PCs with respect to pulse durations. The ratios of standard deviations are shown over the mean values. The initiation points are shown in (c), with the same notation as that in fig. 10c. The threshold-duration curve of a L5 PC is graphed in (d), with the corresponding initiation sites labelled. In addition to the durations in a & b, the thresholds for 0.2 ms, 2 ms, and 20 ms stimulation were also tested. The thresholds of 5 ms, 10 ms & 20 ms stimuli are magnified in the side window with the linearly interpolated values marked with open squares and dashed lines..... 57

Figure 12 Comparison between thresholds (a) and polarization lengths at soma (b) measured in silico and in vitro. Simulated values are displayed in violin plots, with the kernel densities denoted by the shaded areas, mean values by open circles, and quartiles by bold bars. The ranges occupied by in vitro recordings are depicted in vertical bars, with the mean values (if available) labelled by filled squares. .... 59

Figure 13 Maximum depolarizations of the bending point and the terminal during 0°-100 ms stimulation with bending angle increased from 55° to 95°.. 63

Figure 14 A L2/3 pyramidal neuron (a) before and (b) after unraveling. As a result of the process, the Roll distances, i.e. the displacement from the segment terminal to the cell body, are shifted upwards, which can be contrasted using the histograms (c) before and (d) after the process..... 69

Figure 15 Box plot of thresholds to monophasic and biphasic TMS applied in two directions, overlaid on the MTs (of the Dantec stimulator) obtained in clinical studies (red) (Kammer et al. 2001). Note that the unit for MTs is the normalized square root of the stimulator output, which is “approximately proportional to the electric field induced”. .... 71

Figure 16 Activation rates of L2/3 & L5 PCs with respect to different field intensities. All values used are from A-P biphasic stimulation, i.e. the most efficient stimulation configuration..... 72

Figure 17 Sensitivity of thresholds to arborization (a) and tortuosity (b). Values are presented as percentage differences to neurons without manipulation on morphology. Measurements obtained from L2/3 PCs are labelled in grey; L5, red. The evolution of thresholds of a L2/3 PC with axon collaterals continually detached from the shaft is shown in (c). Note that the activation site is always located at the terminal of the axon shaft. .... 73

Figure 18 Sensitivity of thresholds to changes in cell diameters. (a) shows the thresholds of L2/3 & L5 PCs to 0°-100 ms stimulation. Three different types of manipulation were test: expanding all diameters to two folds; expanding all diameters to three folds; and expanding diameters of axonal terminals to two folds. (b) depicts the thresholds of the same cells to monophasic P-A TMS stimulus. .... 74

Figure 19 Thresholds of cells with a straight axon, a branched axon and a 30° bent axon to 0° & 30° 100ms stimulation. The dendritic components of the three cells are the same. .... 80

Figure 20 The morphology of the tested nest basket cell in (a) front view and (b) side view. Axonal components are plotted in red; the dendritic and somatic ones are colored in black. The neuron has 51 basal dendrites (average diameter 1.0 μm, length 36.42 μm) and 127 axonal segments (average diameter 0.3 μm, length 61.22 μm). .... 82

Figure 21 Sum of feature errors vs generation. (a) The error sums of the 10 fittest solutions within each generation are averaged and plotted against the number of iterations. (b) Distribution of the feature errors after the searching. Note that the error of last feature, the number of APs at the absence of current injection, is omitted as the value is always zero for all selected solutions. .... 95

Figure 22 Distribution of ion channel maximum conductance values. The ion channels attached to the axonal components are colored in red, whereas the ones attached to the cell body are in black..... 96

Figure 23 Correlation map of the spiking features and the stimulation thresholds. The upper panels show the scatter plots of different pairs of parameters; the lower panels exhibit the corresponding correlation values, \*: p < 0.05, \*\*: p < 0.01, \*\*\*: p < 0.001..... 99

Figure 24 MPs and thresholds of two fittest solutions. (a) MPs of the NBC in response to current injection. (b) The thresholds of the two solutions towards 12 different field directions. As the NBC lacks a clear axon shaft, the 0° is labeled as the opposite of the y axis of the coordinate system in which the morphology was reconstructed. .... 100

## List of abbreviations

AHP	after hyperpolarization
AMT	active motor threshold
AP	action potential
A-P	anterior-posterior
DBS	deep brain stimulation
dIPFC	dorsolateral prefrontal cortex
DS axis	dendritic-somatic axis
D-wave	direct wave
ECT	electroconvulsive therapy
EEG	electroencephalogram
EM	electromagnetic
EMG	electromyogram
EPSP	excitatory post-synaptic potential
FDA	United States Food and Drug Administration
FEM	finite element analysis
fMRI	functional magnetic resonance imaging
GABA	$\gamma$ -aminobutyric acid
GABA <sub>A</sub> receptor	A type GABA receptor
HH	Hodgkin-Huxley
HSD	honest significant difference
IPSP	inhibitory post-synaptic potential
I-wave	indirect wave
L2/3	neocortex layer 2/3
L4	neocortex layer 4
L5	neocortex layer 5
L-M	lateral-medial

MCS	motor cortex stimulation
MP	membrane potential
MT	motor threshold
NBC	nest basket cell
NSGA	non-dominated sorting genetic algorithm
P-A	posterior-anterior
PC	pyramidal cell
PCA	principle component analysis
PET	positron emission tomography
PTN	pyramidal tract neurons
RLC	resistor-inductor-capacitor
RMT	resting motor threshold
rTMS	repetitive TMS
SBX	simulated binary crossover
SICF	short interval intracortical facilitation
SICI	short interval intracortical inhibition
STDP	spike-timing-dependent plasticity
STN	subthalamic nucleus
tDCS	transcranial direct current stimulation
TES	transcranial electric stimulation
TMS	transcranial magnetic stimulation



# Chapter 1 Introduction

## 1.1 Motivation

Electromagnetic (EM) stimulation has been used in medical treatments for various brain-related conditions for a long history. The modalities of stimulation that are still being applied and studied include electroconvulsive therapy (ECT), transcranial electric stimulation (TES), trans-cranial magnetic stimulation (TMS), transcranial direct current stimulation (tDCS), deep brain stimulation (DBS) and motor cortex stimulation (MCS). Although their target areas and instrumentation are different, these treatments all share the same underlying principle: the application of an electric field on neurons to modulate their activities. However, the detailed mechanism of these treatments is still unknown, which has restricted the development of stimulation technologies.

The difficulties in understanding the mechanism lie in three major aspects – what is the intensity of the electric field supplied; how the field changes the neuron activities; and how the modulated neurons influence each other to give rise to therapeutic effect. The first issue has been tackled with the development of head models and numerical calculations of the electric field; the third issue has been investigated with the connectome model between neurons; the second issue – the intermediate link between the applied field and the neuronal responses – has remained largely unaddressed.

To fill in the knowledge gap, cell activities are to be monitored, and the most commonly adopted method is by insertion of electrodes which has been proved infeasible under stimulation environment – not only the recording

suffers from stimulation induced artifacts, but the introduction of the electrode would also alter the applied field. In substitution, researchers have established mathematical models to simulate the induced polarization of membrane and the subsequent neuronal firing. In general, these theoretical models are based on the fundamental assumption that the neuron can be treated as a long cable and that the membrane potential (MP) can be calculated according to the traditional cable theory. Results have been calculated on simplified morphologies such as an infinitely long axon or a simplified branched dendritic tree. These preliminary researches provided important insights into the basic principles of how the electric field induces neuron membrane polarization, but they lacked the precision and explanatory power to provide information on some of the key points concerning stimulation efficacy – the threshold for neuronal excitation, the location of activation and the difference between cell groups.

In this project the author works on extending and improving the simulation approach to explore the interaction between the applied electric field and the target neurons. By studying the cellular responses to stimulation and by identifying the factors that can influence neuronal excitability in the light of neurons with realistic morphology and physiological properties, the author aims to unravel the mechanism underlying the modulation and in turn the therapeutic effect.

## **1.2 Research objectives**

The aims of the present study were to develop a novel simulation scheme for measurement of the neuronal response towards EM stimulation. In detail, the aims could be decomposed into:

1. To develop a simulation model that is physically and mathematically valid and can be ubiquitously applied to neurons without compromising realistic morphology and physiological properties.
2. To quantify the cellular responses towards stimulation, including the thresholds and polarization lengths, and to validate the approach via comparison of the values with experimental data.
3. To investigate the influence of field direction, pulse waveform, cell morphology and membrane conductance on the susceptibility of the cell.

In order to achieve these objectives, a series of tests were applied on the subject cells, which comprised three major steps. The first step was to determine the appropriate mathematical formalization, morphological treatment, membrane conductance values, discretization scheme, and validation methods used in the computation to ensure validity of the simulation. Secondly, responses of the target cells were measured with the model and were analyzed statistically. The obtained values were compared with the results recorded in previous experiments to further consolidate the model. Lastly, sensitivity analysis was conducted on all the subjects with a selection of varying parameters to reveal the influence of these features. This workflow was sequentially conducted on pyramidal cells (PCs) with rectangular stimulation pulses, PCs with TMS pulses and an inhibitory cell with various stimuli. Results obtained are reported in the present manuscript.

### **1.3 Thesis organization**

This thesis contains seven chapters:

Chapter 1 presents a brief introduction to the topic and outlines the research objectives of this study.

Chapter 2 extensively reviews published literature on the design and application of EM stimulation. This chapter also surveys the existing understandings and established models concerned with the working mechanism of stimulation.

Chapter 3 details the mathematical formalization of the computation, the general design of the simulation model, the implementation on neurons, as well as the validation tests.

Chapter 4 discusses the responses of pyramidal cells towards long duration uniform field stimulation and the impact of field direction and pulse duration. Results are further compared with data from previous *in vitro* experiments.

Chapter 5 describes the susceptibility of cells to TMS stimuli and the influence of cell morphological features, including tortuosity, arborization, diameter, and synapse bouton formation.

Chapter 6 presents a novel approach to search for membrane conductance values of an inhibitory neuron. The susceptibilities of inhibitory cells are also documented.

Chapter 7 summarizes the major findings of the research and suggests several recommendations for future work.

## **Chapter 2 Literature review**

### **2.1 EM stimulation for neurological disorders**

EM stimulation has been applied on patients to harvest therapeutic effects for over a hundred years. The earliest example, ECT, dates back to the 17th century when it was utilized by clinicians to treat epilepsy as it was believed capable of “resetting” the brain, and hence it could help the patients recover from seizure. Due to the side effects associated with the technology, the treatment was only given to patients with severe neurological disorders. In the 1980s, the development of EM theories and manufacturing devices gave rise to new modalities of stimulation, namely transcranial electrical stimulation (TES), transcranial direct current stimulation (tDCS), transcranial magnetic stimulation (TMS), deep brain stimulation (DBS) and motor cortex stimulation (MCS). According to the way the magnetic field is delivered, these modalities can be classified into two categories – non-invasive and invasive stimulation.

#### **2.1.1 Non-invasive stimulation**

ECT was proven effective in treating epilepsy and major depression, but could frequently trigger adverse effects including muscle cramp, seizure onset and memory loss. In addition, general anesthesia must be administered prior to the treatment, and the patient must be hospitalized during the whole session. To overcome the drawbacks, a new technique was developed to deliver the effective electric field to the cortex without anesthesia – transcranial electrical stimulation. To direct the stimulation, two electrodes are attached to the scalp, one to the cranial suture (cathode) and the other to the temporal area (anode), and a high voltage brief pulse is applied, which would force current to flow

through the skull and the cortical tissue underneath, exciting the relevant area (fig. 1a) (Merton et al., 1980).

TES has shown promising effects in treating neurological disorders and can be applied without anesthesia; few side effects have been documented. However, as the electric current passes through the scalp and the muscle underneath the electrodes, the nociceptors would inevitably be activated and the whole process can be intolerably painful.

tDCS has a similar setup as TES with two major differences: the electrodes are relocated on the left and right lobes; the power supplied is a long duration DC current through the brain (fig. 1b). As the current is very small compared to TES, no neuron is directly activated during the process. Instead, the effect is believed to be a long lasting hyperpolarization/polarization of the cell membrane and the subsequent alteration of cortical excitability.

In 1985, a new device was developed, which could deliver electric field through electromagnetic induction without inducing pain (Barker et al., 1985).

The modality, i.e. TMS, utilizes an RLC circuit (fig. 2a) in which a magnetic

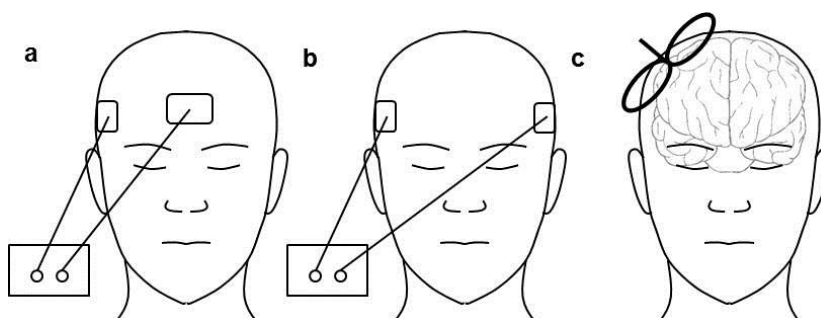


Figure 1 Schematic diagram of (a) TES (b) tDCS & (c) TMS. Note that although the physical setup of TES and tDCS are basically the same, the electric currents running through the electrodes are different. The former employs a brief yet tremendous current, which directly induces neuronal activations; while the latter applies a mild long-lasting current, which modifies the excitability but not the activity of the neurons.

field is generated by a pulse current in the loop which in turn gives rise to an electric field in the brain tissue through electromagnetic induction (fig. 1c). Since TMS is painless and has little side effect – the only known being having a 0.4% chance to induce seizure on patients already suffering from epilepsy (Reis et al., 2008) – it immediately gained popularity among clinicians. Subsequent development immediately followed – new waveform was explored, in which two effective phases instead of one is comprised in a single pulse; novel coil design was advanced by placing two circular coils tangential to each other, which helps to focus the electric field to a smaller area to achieve more uniform stimulation field (fig. 2b)(Jalinous, 1991); repetitive application of stimulation without human intervention was realized, in which a train of pulses are delivered repetitively with the frequency specified by the physician (rTMS). The improvement on hardware empowered the researchers to test different stimulation setups on treatment of multiple neurological disorders, and finally it was discovered that the application of high frequency (>130Hz) stimulation to the dorsolateral prefrontal cortex (dlPFC) could significantly alleviate the symptoms associated with refractory depression. This specific stimulation protocol has become the most common application of TMS and has obtained FDA approval.

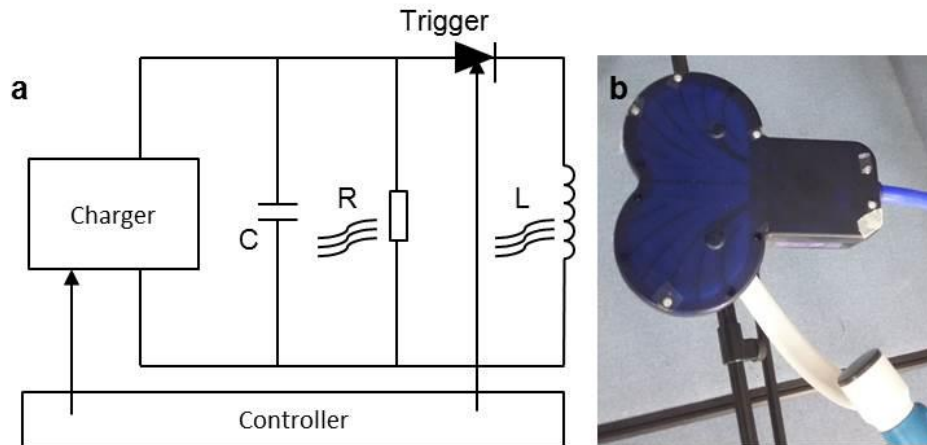


Figure 2 Design of a typical TMS device. The circuit is shown in (a). The major variation on design lies under the “stimulating coil”. The most common coil used in clinical trials and academic studies is the (b) “figure of eight” coil.

### 2.1.2 Invasive stimulation

Invasive stimulation features the insertion of electrodes into the brain and the excitation of the surrounding tissues. It has long been practiced by researchers to investigate the functions of various areas and by doctors to probe the onset loci of epilepsy, during which the electrode is only temporarily inserted and no long term stimulation was administered. The therapeutic application of invasive electrical stimulation is exemplified by DBS (Limousin et al., 1995). The technique involves implantation of a lasting electrode to the subthalamic nucleus (STN) and the delivery of high-frequency pulse trains to the target area for weeks. It is believed that, via repetitive stimulation, micro-lesions would be induced onto the hyperactive STN and the whole cortico-limbic-striatal pathway would be modulated, hence the motor symptoms of Parkinson’s disease could be alleviated. DBS is considered as one of the most effective ways in treating treatment-resistant Parkinson’s disease and is widely used on patients who cannot respond to pharmaceutical intervention.



Compared with DBS, MCS targets the motor cortex instead of a deep brain nucleus; an array of electrodes, rather than a single one, is inserted (Tsubokawa et al., 1991). The therapy has shown promising effects in dealing with movement and pain disorder but the working mechanism is unclear.

### 2.1.3 Clinical application

Aside from the approved applications, the aforementioned stimulation modalities have also been tried in various off-label tests to treat other brain related diseases. A brief review of studies performed on mental disorders and showing positive responses is set out in table.1.

Table 1 Review on experimental trials of EM stimulation on mental disorders. Only the tests showing positive responses are listed.

Name	Description	Neuromodulation	Reference
Addiction (tobacco, alcohol, heroine, etc.)		rTMS, tDCS, DBS	Barr et al. (2011)
Alzheimer (dementia)		rTMS, tDCS, DBS	Schulz et al. (2013) Laxton et al. (2012)
Anorexia nervosa	Immoderate food restriction, irrational fear of gaining weight	DBS	Wu et al. (2012)
Anxiety disorder(exclude PTSD)		DBS, rTMS	Baek et al. (2012); George et al. (2008); Sturm et al. (2003)
Attention deficit disorder (ADHD)	Difficult to concentrate, hyperactivity, uncontrollable impulsiveness	rTMS, TMS*	Schulz, Gerloff et al. (2013);Richter et al. (2007)
Autism	Poor interaction or communication skill, restricted and repetitive	rTMS, dTMS	Schulz, Gerloff et al. (2013); Park (2003) Bersani et al. (2012)

	behavior		
Binge eating disorder	Uncontrollable carving for food	tDCS	Goldman et al. (2011) Reddy et al. (2000)
Bipolar disorder	Phasic alternation of maniac and depression	ECT, dTMS	Papadimitriou et al. (2007); Bersani, Minichino et al. (2012)
Catatonia	Sudden loss of ability to move	ECT	Rohland et al. (1993)
Delirium	Lowered alertness, altered sleep cycle, decreased short-term memory, seeing hallucinations	ECT	Dudley et al. (1972)
Depression		tDCS, ECT, DBS	Schulz, Gerloff et al. (2013) Moreines et al. (2011)
Epilepsy		DBS, tDCS, rTMS	Zhong et al. (2011) Ardesch et al. (2007) Faria et al. (2012) Cincotta et al. (2003) Lunde et al. (2006) DeGiorgio et al. (2006)
Learning disorder		tDCS	Pinchuk et al. (2012)
Mania	Irritable mood, arousal or energy level	rTMS, ECT	George et al. (2009); Karmacharya et al. (2008)
Migraine	Intolerable headache	rTMS	Wassermann et al. (2012) Hord et al.

			(2003)
Obsessive compulsive disorder		rTMS, DBS	George, Padberg et al. (2009) George et al. (2008); Sturm et al. (2003)
Post-traumatic stress disorder		rTMS, ECT, DBS	Wassermann et al. (2012) Langevin et al. (2010); Margoob et al. (2010)
Schizophrenia		rTMS, dTMS, ECT, tDCS	Schulz, Gerloff et al. (2013) Bersani, Minichino et al. (2012) Chanpattana et al. (2000) Brunelin et al. (2012)
Tinnitus	Hearing hallucination	rTMS, tDCS, DBS	Wassermann et al. (2012) Vanneste et al. (2011) Cheung et al. (2010)

\*: for diagnosis

In addition to mental disorders, neurological disorders where mental function is intact but the sensory or motor pathway is impaired represent another major category of brain disorders on which stimulation has been administered. A list of trials is given in table. 2.

Table 2 Review on experimental trials of EM stimulation on neurological disorders.

Name	Description	Neuromodulation	Reference
Amyotrophic lateral sclerosis	Progressive inability to move, speak, swallow and breathe	TMS*, rTMS	Horiuchi et al. (2002); Vucic et al. (2011)
Chronic pain		DBS, MCS, rTMS, tDCS	Plow et al. (2012)

Coma (persistent vegetative state)		DBS	Yamamoto et al. (2005)
Dystonia	Sustained muscle contraction	DBS, TMS*	Gubellini et al. (2009) Quartarone et al. (2009)
Essential tremor		DBS	Gubellini, Salin, Kerkerian-Le Goff, and Baunez (2009)
Huntington's disease	Genetic disease, uncoordinated movement, leading towards cognition problem and finally death	DBS, TMS*, rTMS	Gubellini, Salin, Kerkerian-Le Goff, and Baunez (2009) Tasset et al. (2012) Groiss et al. (2012)
Multiple sclerosis	Autoimmune disease causing movement and cognition disability	tDCS, TMS*	Mori et al. (2010) Ziemann et al. (2011)
Parkinson's disease		DBS, TMS*, ECT, rTMS	Gubellini, Salin, Kerkerian-Le Goff, and Baunez (2009) Popeo et al. (2009); Schulz et al. (2013) Perretti et al. (2011)
Tourette's syndrome	Chronic motor and vocal tic, usually taking places among children and adolescents	TMS*, DBS	Gubellini, Salin, Kerkerian-Le Goff, and Baunez (2009) Gilbert et al. (2005)

\*: for diagnosis

EM stimulation has also been applied for non-therapeutic effects. The aim of the stimulation was to harvest the facilitatory effect of stimulation to accelerate the rehabilitation or the learning process (M. Kandel et al., 2012; Miniussi et al., 2008; Reis et al., 2008; Schulz et al., 2013). Due to ethical concerns, they are usually characterized by small sample sizes and limited stimulation dose, and the results are subject to reproducibility of the test data and interpretation of the responses.

## **2.2 Current understandings of EM stimulation**

The clinical studies listed above, often empirical and subjective, could help doctors and clinicians explore the novel application of stimulation but could not provide cellular or network level information of the stimulation efficacy. In solving the problem, researchers have conducted experiments on isolated cells and documented the corresponding stimulation-evoked activities. Another approach was to administer stimulation on subjects and to monitor motor or neuronal responses downstream to the target area, usually being motor cortex. In addition, neuroimaging techniques have also been exploited.

### **2.2.1 Direct measurement of neuronal activities**

The most straightforward way to investigate the responses of cortical neurons is to observe their cellular activities under stimulation. Although this procedure can be technically demanding, it has been adopted in a few researches where the neurons of animal origins were collected and cultured in an artificial environment; an electric field was produced by an array of electrodes placed on the opposite sides of the culture; and finally the MP dynamics were measured in correlation to different amplitudes of electric field. In one early attempt, Svirskis et al. (1997) utilized motor neurons of turtles

and successfully proved that the changes in MPs evoked by stimulation matched what was calculated from the cable theory. However, since the cell was collected from the spinal cord of reptiles, the stimulation-evoked responses could be expected to be quite distinct from those of the cortical neurons of mammals. Despite the validation of the mathematical model, the report gave little information on the effectiveness of the stimulation modalities that are used for therapeutic effects.

Radman et al. (2009) adopted the similar method but used brain slices from Wistar rat somatosensory cortex. Various parameters concerning EM stimulation, including the threshold values of the different groups of cells, the optimal field direction and the polarizations at soma, were extracted from the electrophysiological recordings under a 100 ms-uniform field stimulation. The results had three indications: the LV pyramidal cells have lower thresholds than L2/3 PCs; the maximum efficacy is characterized by alignment between the cell and the field; the polarization is linearly proportional to field and can be quantified with polarization length.

Notwithstanding the findings derived, the direct measurement approach suffers from multiple limitations. All the existing studies were conducted *in vitro*, hence the neurons could only be from non-human animals. Besides, the slice preparation and clamping can be extremely delicate; synaptic connection could be undermined; the neurons may suffer from incompleteness. On the other hand, should the test be performed *in vivo*, the subject must be anesthetized hence the excitability may be suppressed; the structural intactness of the skull would be compromised; due to the inserted electrodes, the field profile may be altered. Last but not least, no matter where the experiment is taking place, the

application of a short duration pulse which is characteristic to almost all suprathreshold stimulation modalities could introduce high amplitude artifacts on the measuring electrodes, rendering the readings unreliable. In the light of these technical constraints, researchers have adopted indirect approaches as substitutions.

### **2.2.2 Motor cortex: cytoarchitecture and stimulation effectiveness**

Motor cortex has been a common target in therapeutic application of EM stimulation – MCS is named after its implantation to motor cortex; tDCS has also been applied on the very cortical region to facilitate motor rehabilitation. For TMS, although the common target for repetitive mode stimulation is the dlPFC, the dosage of each single pulse is marked as percentage of the minimum pulse intensity to evoke motor response when applied to the hand area of the primary motor cortex, namely the motor threshold (MT). Moreover, the motor cortex has direct control over the motor output at the cortical level and its activation can be observed directly (limb movement), therefore, it has been a common target for research practices as it can provide straightforward assessment to the effectiveness of the stimulation as well as the cortical excitability.

The cytoarchitecture of motor cortex generally follows the common structure of mammalian neocortex, which comprises the superficial molecular layer (L1), the deeper external granule and external pyramidal layer (L2/3) which contains small or medium pyramidal cells, the internal granule layer (L4) featuring stellate cells, and the internal pyramidal layer and the multiform layer (L5/6) characterized by large pyramidal cells. Compared with other cortical areas, the motor cortex is distinguished by the absence of a prominent

L4 and the stellate cells. Furthermore, L5/6 is much thickened. Like the other cortical regions, the majority of the intracortical excitatory transmission is mediated by PCs, named after their triangular cell bodies. However, a special type of neurons – the pyramidal tract neurons (PTNs), or the Bezt cells according to the name of their discoverer – are exclusively presented in the L5/6 layer of the motor cortex. Physiologically, these cells have irregularly large cell bodies, fast spiking firing patterns and direct projections to the pyramidal tract of the spinal cord which is the cellular substrate of the cortico-spinal relays, i.e. the motor output of the cortex (Chen et al., 1996). Electrophysiological analysis of the region further revealed ultra-strong connectivity between the L2/3 PCs and the L5 cells, by which a single superficial layer neuron could monosynaptically trigger the firing of inferior layer neurons (Anderson et al., 2010; Weiler et al., 2008). Nearly all inhibitory neurons identified in the cortex, including the basket cells, bipolar cells, double bouquet cells, bitufted cells, Martinotti cells and chandelier cells are present in the motor cortex, but the majority of the inhibitory transmission is mediated by basket cells (Gupta et al., 2000; Markram et al., 2004).

The somatotopic map of the somatosensory cortex is echoed in the motor cortex, so that a segment of the cortex is responsible for the motor control of a specific part of the body. In the TMS and TES stimulation trials, the most common target has been the hand area of the motor cortex, which makes a 45° angle with the sagittal plane and locates at the middle of the central fissure. In a few cases, the leg area has also been targeted to contrast the influence of field direction.



### **2.2.3 Motor threshold**

MT, as mentioned before, is the dosimeter used in rTMS and TES application to normalize the individual variance and to provide a quantitative assessment of cortical excitability. The value of MT is defined as the minimum stimulator output (in percentage) that can produce a 50  $\mu$ V peak-to-peak spike on the electromyogram (EMG) of the target muscle in at least 50% of all the trials. Two types of MTs are measured in clinical trials – resting motor threshold (RMT) and active motor threshold (AMT), with the former evaluated when the subject is at rest and the latter when the muscle is voluntarily contracted. In general, the reading of AMT is lower than RMT for a single patient although the reading can vary greatly among different subjects.

The MT is influenced by various other factors. Amplitudes of MTs to different angles, i.e. the anisotropy, were graphed in previous studies (Balslev et al., 2007; Werhahn et al., 1994); the correlation between the value and the coil-scalp distance was mapped (McConnell et al., 2001; Stokes et al., 2007); the effect of pulse duration on MT was validated (Rothkegel et al., 2010). MT measurement has also been adapted to assess the performances of different stimulators, where a new coil or new circuit design is deployed and the corresponding MT is compared with a commercially available one (Roth et al., 2014). In a comprehensive study of the MTs, Kammer et al. (2001) conducted the measurement for four different stimulator coils from two different manufacturers. Based on the results they had the following conclusions: 1, for monophasic – over damped – stimulation, the posterior-anterior (P-A) configuration is most effective; 2, for biphasic – underdamped – stimulation, the anterior-posterior (A-P) configuration has the highest efficacy; 3, evoking

EMG changes by A-P biphasic stimulation is more versatile but is still quite similar to the that by P-A monophasic stimulation, which hints that the second phase of biphasic stimulation work equivalently as the first phase of monophasic stimulation in exciting neurons; 4, the MT values of biphasic stimulation are lower than monophasic pulses, which could be attributed to the fact that the second phase the biphasic pulse has longer duration than the first phase of the monophasic pulse; 5, although a significant individual variance is present in the thresholds of different subjects, the general trend of each patient – being biphasic A-P < biphasic P-A < monophasic P-A < biphasic A-P – is almost preserved in all of the tested individuals.

#### **2.2.4 Epidural recording of pyramidal tract**

Epidural recording refers to the monitoring of neuronal activities of the pyramidal tract in the spinal cord, which is the downstream area to the motor cortex. In brief, all the recordings were taken from patients who had spinal cord stimulators implanted for the treatment of intractable dorsolumbar pain. The electrodes were most commonly implanted in the epidural space either at C1 – C2 level or at the thoracic level. Recordings were made of descending activity 2 to 3 days after implantation during the trial screening period before connection to the final implanted stimulator. Simultaneous EMG recordings can also be made from a variety of hand and leg muscles during TMS or TES of the scalp.

For TES, the lowest intensities of anodal stimulation at AMT recruit an early descending volley, which has a latency of 2 – 2.6 ms when recorded from the high cervical cord. In humans, this latency is compatible with direct activation of the pyramidal tract axons just below the grey matter, and hence this wave is

referred to as a D-wave. At higher stimulus intensities, a later small wave appears in some of the subjects that has the same latency as the lowest threshold volley recorded following magnetic stimulation with a posterior-anterior induced current in the brain.

On the other hand, when monophasic TMS – “magnetic stimulation” – is applied in the p-a direction, the initial spike has a delay of some 1.5 ms longer than the TES. The longer delay suggests that the activation happens upstream of the neuron fiber. Together with the fact that this spike is subject to modulation of cortical activity, it was conjured that the spike is produced by indirect synaptic activation in the cortex, hence I-wave. Only when the stimulation intensity is raised above the AMT would the D wave be triggered with TMS.

If the orientation of the induced current in the brain is changed so that it runs in a lateral to medial direction, EMG responses in some subjects get earlier by about 1 – 2 ms. It has usually been presumed that this is because a lateral-medial (L-M) orientation of the coil begins to recruit D-waves more easily than the P-A direction.

The pyramidal tract volleys are influenced by multiple factors including muscle state and pharmaceutical intake. Voluntary contraction has no effect on the amplitude of the D-wave recruited by TES or L-M magnetic stimulation. However, voluntary contraction does increase the size and number of the I-wave volleys. During strong contractions, the effect can be substantial, and all I-waves are affected. A maximum contraction can increase the total amplitude of the I-wave volleys by up to 50%. Interestingly, the effect on the size of

descending waves is not paralleled by a comparable effect on the threshold for evoking descending activity. The value remains unchanged regardless of the cortical activities.

The opposite effect on the recruitment of descending volleys occurs when the excitability of the motor cortex is decreased. Administration of the GABA agonist lorazepam suppresses the recruitment of later I-waves by TMS, without affecting the threshold for producing recognizable volleys.

When TMS pulses are given in pairs, separated from each other for a few milliseconds, the resultant epidural volleys can be more complex than the superposition of two individual trials of recording. Based on the amplitudes of the pulses and the intervals, the overall effect can be either inhibitory or facilitatory, reflected by short interval intracortical inhibition (SICI) or short interval intracortical facilitation (SICF).

SICI was first reported by Kujirai et al. (1993). They found that a small subthreshold conditioning stimulus could suppress the response to a later suprathreshold test stimulus when the interval between stimuli was less than 5 ms. When the control stimulus alone is applied, 4 I-waves in epidural recordings and a substantial peak in EMG can be recruited; on the other hand, the application of the conditioning pulse, which is 80% of AMT, cannot give rise to a single I-wave or any distinguishable peaks in the EMG. However, if the conditioning pulse is administered prior to the conditioning trace, with an interval of 1-4 ms, the I-waves evoked by the control stimulus is abolished and the EMG peak is significantly depressed. The inhibition effect is dependent on the interval, where the briefer the interval, the stronger the inhibition. Note

that the first I-wave, i.e. the I1-wave, is not influenced by the inhibition effect and stays constant with regard to different stimulations.

Since the conditioning stimulus was below AMT, the authors suggested that the interaction was occurring at a cortical level and that the conditioning stimulus was suppressing the recruitment of descending volleys by the test stimulus. Interestingly, the I1-wave is virtually unaffected by the SICI effect, with the most sensitive wave being the I3 and later volleys. Administration of lorazepam, an agonist at the GABA<sub>A</sub> receptor increases the amount of intracortical inhibition and also increases the inhibition of later descending I-waves.

Short interval paired pulse facilitation describes the phenomenon that if two stimuli are given at an intensity at or above active motor threshold, facilitation can be observed between them when the intervals between the shocks are around 1.3, 2.5 and 4.3 ms. This interaction between the stimuli is thought to be due to the interaction of I-wave inputs in the periodic bombardment of pyramidal neurons. Yet again, in SICF, only the I2 & I3-waves are clearly facilitated; the I1-wave is unchanged.

### **2.2.5 EEG and neuroimaging**

In supplement to the aforementioned methods, researchers have also adopted various other measurement modalities to probe the impact of stimulation activities. The recent examples include electroencephalogram (EEG) tests (Ding et al., 2014; Faria et al., 2012), functional magnetic resonance imaging (fMRI) trials (Bestmann et al., 2003; Fox, Halko, et al., 2012) and the less frequent positron emission tomography (PET) (Krieg et al., 2013). The

adoption of these modules empowers the investigators to view the stimulation efficacy in the context of the brain network instead of focusing on the response of a few specific areas and has successfully pinpointed the inter-cortical modulation effect of stimulation. However, the neuroimaging modalities have a relatively poor time resolution (~1-2s); the EEG based study suffers from the stimulation-evoked artifact, and hence are unable to provide reliable readings instantly after the administration; these modalities are better suited to long term evaluations instead of analysis demanding temporal precision.

### **2.3 Hypothesis on the working mechanism of EM stimulation**

As mentioned in the earlier section, direct observation of cell activities under stimulation has low feasibility and can suffer from various types of artifacts. Indirect measurements, on the other hand, generate immense amount of data concerned with the stimulation-evoked responses. These observations nevertheless are macroscopic, hence could not be straightforwardly interpreted in the light of cell activity, network communication and metaphysical signal processing. Due to these issues, computer simulation has been adopted to mitigate the difficulties in experimental setting and to elucidate the working mechanism of EM stimulation.

#### **2.3.1 High resolution profile of electric field**

With the development of numerical computation schemes, researchers have attempted to solve the electric field that is induced by the stimulation on the geometry of the human brain and to use the high resolution field profile to predict the geometrical extent and the onset location of the stimulation. In general, a 3D head model, either derived from a standard atlas or reconstructed from patient neuroimaging data, is placed under the stimulation coil with a

specific relative angle and coil-scalp distance. The electromagnetic properties of the materials enclosed with the model, including the electric conductivities and dielectric permittivities, are derived from animal or post-mortem studies and applied to the structures in the head, specifically the scalp, the skull, the cerebrospinal fluid, the gray matter and the white matter. The electric field is calculated firstly by computing the electric current running in the circuit and then by solving the Maxwell equations governing the magnetic induction and electric conduction from the stimulator to the whole head model. In a few studies, a customized “coherence” value is provided according to the orientation of the neuronal fibers and the local electric field to assess the cortical excitability. The explanatory capacity of the calculation enables researchers to visualize the electric field produced by stimulation, and moreover to compare the efficacies of different configurations (Nadeem et al., 2003; Nummenmaa et al., 2014). The field strength of MT, the onset locations of activation and the spatial expansion of the effective stimulation area has been tested with this approach (Thielscher et al., 2002). Furthermore, the impact of head/stimulator geometry, quantified as the dependence of the field strengths on coil-scalp distance, the thickness of the skull, the presence of lesions and various other parameters, were also investigated (Grant et al., 2010; Miranda et al., 2012; Wagner et al., 2006; Wagner et al., 2007). Nevertheless, the nature of the model determines that the method can supply limited information on the interaction between the field and the neurons in the cortex, where a number of neurons with distinctive morphologies and physiological properties are present and are interconnected.

### **2.3.2 Network model**

Neuronal network is based on physiological data. A “perfect” neuronal network would have realistic neurons, structures and synaptic dynamics and thus would be the ultimate tool to analyze brain. Nonetheless, tremendous amount of information needs to be collected to construct such a network, making it infeasible in real life. Several simplified neuronal networks have been published as substitutes. They are used to study information processing at network level and the role of each physiological element in this process.

Neymotin et al. (2011) studied the input-output transformation taking place in a single column and its dependence on the connection strengths within the column. Tsodyks et al. (1998) used a similar network with synaptic strength correlated to presynaptic firing frequency to demonstrate that excitatory post-synaptic potential (EPSP) facilitation and depression actually represents different aspects of neuronal activities. Davison et al. (2006) used network model to show that spike-timing-dependent plasticity (STDP) is crucial for multi-modality sensory information fusion. Cutsuridis et al. (2010) encoded STDP on different types of neurons in hippocampus CA1 to reproduce the information encoding and retrieval process, which is crucial to the memory system. Haeusler et al. (2007) compared computation capabilities of networks having a biological laminar structure and random connection and showed that laminated structure could actually enhance a network’s performance. Kerr et al. (2012) mimicked brain damage by removing part of neurons in a normal functioning network and studied how electrical stimulation can restore brain function.



The network developed by Traub et al. (2005) is the most comprehensive model in explaining physiological signals. Distinct morphologies and membrane mechanisms were assigned to different types of neurons. Furthermore, electric couplings were added to enrich the connection mechanisms. The resultant model could exhibit multiple physiological phenomena including gamma oscillation, sleep spindle and epileptogenic bursts. Lang et al. (2011) contributed a novel way to generate a comprehensive neuronal network model from microscopic observations on the fly so that the neurons and the connections could be direct duplicate of the studied brain.

Network level simulation has been extensively used in exploring the stimulation effectiveness and has shed some light on cortical activities induced by the externally applied field. A number of models was focused on a specific phenomenon encountered during experiment, such as the silence period (Miyawaki et al., 2005) and the summation effect of later I-waves on  $\alpha$ -motor neurons (Thickbroom, 2011). On the other hand, researchers have also attempted to provide comprehensive models aimed at reproducing a wide spectrum of the observations in previous studies simultaneously.

Di Lazzaro et al. (2012) advanced a theoretical model which was based on the cytoarchitecture of the motor cortex. The authors proposed that the stimulation recruits L2/3 PCs directly which in turn activate the output PTNs in L5 due to their strong connectivities to these cells. The inhibitory neurons were suggested to be insensitive to direct stimulation but receive excitatory transmission from pyramidal cells. Besides, the L2/3 cells also receive reciprocal excitatory transmission from the L5 cells and the later I-waves are the direct results of the oscillation of the balance between excitatory and

inhibitory activities in the cortex. The model explains the insensitivity of early I1-wave to SICI, the enhancement of inhibition effect of GABA agonists, and the alternation of I-waves associated with the change of field directions.

The model by Esser (2005) was based on the Traub model but was enriched with a detailed connectome of the cells within the motor cortex and the relays from other cortical and subcortical areas. According to the design of the model, the TMS pulse indiscriminately activates a proportion of all the synapses that are hosted in the motor cortex, regardless of the location of the hosting cell. The synapses activate the L5 cells, leading to the first I1-wave; the L2/3 cells are spontaneously excited, which further transmit excitatory inputs to L5 cells, resulting in re-activation and the later I-waves. On the other hand, in the scenario of SICI, the conditioning pulse would recruit a smaller number of synapses. They would not be able to trigger cascading excitatory oscillations but the local inhibition which underlies the following suppression of I-waves. In addition, the model also has the merit to reproduce the dependence of the I-wave amplitude on the pulse intensity as well as the modulation effect of various pharmaceutical agents.

In a recent model by Rusu et al. (2014), it is asserted that the I-waves simply reflect the balance between the excitatory and inhibitory inputs received by the PTNs. The model consisted of a multi-compartment PTN with realistic dendritic formation as well as a number of single-compartment PCs and inhibitory cells, the synapses of which are dispersed all over the dendrites. The authors argued that the I1-wave is caused by proximal excitatory synapses, whereas the later ones resulted from the EPSPs from the distant synapses located on the apical dendrites, which take time to travel to the cell body.

During SICI stimulation, the conditioning pulse activates a small number of excitatory and inhibitory inputs. The excitatory EPSPs decay rapidly, yet the IPSPs would remain effective when the control pulse takes place thus inhibiting the I-waves.

In spite of the insights uncovered, the aforementioned models all suffered from certain drawbacks. It attributed the SICI effect to the cumulative stimulation effect which takes place exclusively on inhibitory neuron. Yet neither the phenomenon nor its electrophysiological basis has been acknowledged. The second model could reproduce the SICI effect, but the robustness of the I1-wave, whose amplitude is not influenced by administration of GABA enhancive chemicals, is largely intangible. The morphologically detailed PTN used in the third model has its membrane conductance values tailored to give it an intrinsic firing rate of 667 Hz, a frequency exactly coherent to the I-waves. Unfortunately, neuron with so high a firing frequency has never been identified in mammalian central nervous system.

A comparison of the models would further reveal the contradicting premises taken during the simulation process. The assumption of the first model, that synapses from L2/3 have higher excitability, and the hypothesis of the second and the third model, that the synapses of distinct neurons have indistinguishable excitability, are mutually exclusive. The observations reproduced – the I-waves, the SICI effect and the pharmaceutical modulation, etc. – only demonstrate the flexibility of the repertoire of the cortical network, that with proper manipulation of the connectivity and the excitability, the stimulation responses can be recreated with a multitude of totally distinctive

ways. Without the understanding of the interaction between stimulation-induced field and the neurons, it is virtually impossible to judge which speculation has the most proximity to the real situation. A thorough understanding of the influence of electric field on the cells, or reciprocally the direct response of neurons to stimulation, is the prerequisite of higher level studies of the stimulation effectiveness.

### **2.3.3 Simulation of the biophysical interaction between neurons and electric field**

Early simulation studies have largely been focused on providing mathematical formalism to the dynamics of MP induced by the external field. For instance, McNeal (1976) established the cable theory-based approach to evaluate the MP changes induced by externally applied electric field. The computation was deployed on two neighbouring nodes of Ranvier linked by a myelinated compartment; the structure was placed 2mm beneath a monopolar electrode; simplified ion channels and membrane properties were attached; the whole set of equation was solved manually for 1ms. The authors successfully demonstrated the MP dynamics of the two nodes under stimulation and in the meantime investigated the dependence of the MPs towards the duration of the pulse, displacement to the electrodes and the diameter of the neuron fiber.

After the invention of TMS, Nagarajan et al. (1993) developed on the basis of the previous simulation by supplementing the computation of the electric field induced by TMS. The results of the stimulation reconfirmed the correlation between the stimulation effectiveness and the cell size/pulse duration. Comparison of the cells with distinct spatial extents hinted that the shorter cells could have higher susceptibility. In the end, the efficiencies of the two

waveforms of TMS – monophasic and biphasic stimulation – were contrasted, with the latter found to be more effective.

Thereafter, the same approach has been transformed on a more sophisticated cell model to mimic the neurons in cortex (Rattay, 1999). The new model contained four major components, namely the dendrites, the soma, the myelinated axon and the unmyelinated axon.

The efficacy of the electrode stimulation and the magnetic stimulation were compared; the preferential activation of the axon over any other components was highlighted; the impact of cell-field coherence was revealed; and the possible scenario in which individual synapses would be excited without activation of the axon was proposed.

The first model that attempted to differentiate the various categories of neurons in the cortex was contributed by Salvador et al. (2011). The investigator placed several cells with simple yet distinctive morphologies – a short cylinder, a long cylinder, a long cylinder with a 90° bend, a U shape, and a bifurcated cylinder joint by a collateral – within a motor cortex model in representative of the different cortical neurons and evaluated their susceptibility to the applied stimulation. Aside from the reconfirmation of the previous observations, the model pinpointed that the PCs with a bending or terminal could have the highest responsiveness to stimulation; existence of the axon collaterals could hinder activation; and the interneurons might be difficult to get activated. In addition, the calculation of the electric field according to the material properties and the shape of the cortex model also

enabled the assessment of the impact of the geometrical factors, such as the hampering effect of tissue heterogeneity.

Apart from the numerical computation, modellers have also taken another strategy in computing the MPs modulated by stimulation, i.e. reduction of the original model and subsequent deduction of analytical solution to the governing equations. Due to the constraints associated with the method, the computations were usually performed on highly simplified neuronal structures, and the ion channels were strategically modified, sometimes even unable to give rise to action potentials (APs). The observations made in these studies were highly specific, such as the polarization of cylindrical or spherical neuronal segments (Cartee et al., 1992), the preferential activation of shunted dendrites to sinusoidal stimulation of certain frequencies (Monai et al., 2010), and the mathematical equivalence of a symmetrical dendritic tree to a cylindrical rod model (Tranchina et al., 1986).

With the rapid development of computation capacity and numerical stimulation technique, researchers have established models with cell morphologies and membrane properties closely imitating the real neurons.

McIntyre et al. (2004) solved the cable equation to simulate the effect of DBS. They first adopted finite element method (FEM) to get potential distribution on brain tissue near the bipolar electrodes and later used this potential distribution to calculate membrane potentials. They discovered that under DBS, axon compartments would fire in response to stimuli; the firing frequencies would be exactly the stimulation frequency. However, the somatic compartments would not share the same firing pattern, due to the fact that the

transmission of AP from axon to soma is prohibited. This effort represents the first quantitative analysis of DBS and lays the foundation for future analysis.

The simulation strategy that combines the head model and the cell model was also elaborated, with the simple cell geometry being replaced with realistic morphologies. Wongsarnpigoon et al. (2012) placed PCs with realistic dendritic structures in the cortex and examined cellular activation triggered by TES. With various configurations of stimulation, the susceptibilities of cells at different locations, the influence of electrode geometry, and the impact of various placement schemes were identified.

Kamitani et al. (2001) calculated the membrane potential induced by a uniform electric field. Their strategy was to attach current sources to all compartments of the neurons, which has the magnitude exactly equal to inlet/outlet current difference. Making use of the simulation, the authors successfully demonstrated the kindling process of the AP and the subsequent after-hyperpolarization (AHP), which was speculated to be responsible for the silence period.

Pashut et al. (2011) calculated the electric field dynamics in a specific area of brain and fed field information to a single neuron model. Based on extracellular potential, membrane potentials were calculated on each compartment. The test performed on a cell with realistic dendritic and somatic structures asserted that the circular TMS may activate cells via evoking APs at the cell body, instead of the commonly acknowledged axon. By continuously abolishing the dendritic sections, the damping effect of the neuronal segments directly connected to cell bodies were exposed at the same time. Furthermore,

the researchers constructed a cell with bent axon. By measuring the stimulation threshold of arbitrary cell, it was demonstrated that activation and a bending point was very difficult to achieve.

#### **2.3.4 Repertoire and drawbacks of existing models**

Making use of strategically simplified cell models, these previous simulation works have provided constructive insights into stimulation-evoked cell activation. Notwithstanding the isolated factors that can characterize the stimulation effectiveness, for realistic neurons on which the various elements could interact with the physiology, morphology, and are interweaved with each other, an inclusive account for their responses to stimulation is still lacking. Many of the critical questions concerned with the effectiveness of stimulation have not been systematically investigated: What stimulation intensity is required for activation? How would the effectiveness change with field direction and pulse waveform? Is there a difference in the excitabilities among various neurons? And if yes, which type is the most sensitive? Furthermore, taking distinct premises in simulation, conflicting conclusions have been drawn regarding the activation mechanism – soma, axon bending point and terminal have been asserted to be the initiation point of action potentials. Without a framework incorporating the repertoire of these works, which proposition has the highest validity remains unanswered.

To answer the aforementioned questions and address the identified issues, here the author presents a different simulation approach, in which minimum simplification of the membrane currents and morphology was introduced. The model was implemented on a multitude of pyramidal cells (PCs) and their responses to various stimuli were statistically examined. It is hoped that by



taking this approach, a more comprehensive sketch of cellular response to stimulation can be provided.

## Chapter 3. Simulation of membrane potential dynamics of neurons induced by EM stimulation

In this study, the author adopted the method in which the neuron is considered as a structure comprised of interconnected 1D segments with specific geometries in 3D space; the numerical computation methods, i.e. finite different method, is deployed in 1D according to the modified cable equation. Adoption of this method allows for relatively accurate results to be obtained with intermediate computation burden.

### 3.1 Mathematical formalization

AP, which is the dominant mechanism of signal transmission in human brain, is defined as a prominent spike in the MP of the cell. MP is calculated as

$$V_m = V_i - V_e \quad (1)$$

where  $V_i$  is the voltage of the intracellular plasma and  $V_e$  is potential of the extracellular environment. The cell plasma contains various types of ions thus can be considered as a weak conductor, the current flowing in the plasma is calculated as

$$I_i = -\frac{dV_i}{R_i dx} \quad (2)$$

where  $I_i$  is the intracellular current and  $R_i$  is the intracellular resistance along the current direction. When an external electric field  $E$  is applied on the neuron, the potential of the extracellular environment is changed, according to

$$E = -\frac{dV'_e}{dx} \quad (3)$$

where  $V'_e$  is the new extracellular potential induced by stimulation. As a result, the intracellular current is then given by

$$I'_i = -\frac{dV'_i}{R_i dx} = -\frac{d(V_m + V'_e)}{R_i dx} = -\frac{dV_m}{R_i dx} + \frac{E}{R_i} \quad (4)$$

The transmembrane current, i.e. the current flowing through cell membrane, is the first order derivative of the intracellular current, given by

$$I_m = -\frac{dI'_i}{dx} = \frac{d^2V_m}{R_i dx^2} - \frac{dE}{R_i dx} \quad (5)$$

The cell membrane is equivalent to a circuit in which a conductor is connected in parallel to a capacitor, hence the current flowing through the membrane can be calculated with

$$I_m = \frac{V_m}{R_m} + C_m \frac{dV_m}{dt} \quad (6)$$

where  $R_m$  is the membrane resistance, and the  $C_m$  is the capacitance.

Combining equation (5) & (6) would give

$$\frac{V_m}{R_m} + C_m \frac{dV_m}{dt} = \frac{d^2V_m}{R_i dx^2} - \frac{dE}{R_i dx} \quad (7)$$

which is the equation governing the MP dynamics under the influence of an external electric field.

To get the MP values of the target cell, the governing equation needs to be solved on the corresponding morphology, with the membrane resistance/conductance determined according to the dynamics of passive and active ion channels.

## 3.2 Numerical computation

### 3.2.1 Solving the model with Crank-Nicolson method

Due to the complexity of the cell morphology and non-linearity of the ion channels, it is almost impossible to have an analytic solution of the governing equation on a real neuron and thus numerical computation is utilized. Under the assumption that MPs and distributions of ion channels are more or less homogeneous within a limited space, the neuronal morphology is firstly discretized into multiple compartments; the evolution of MPs are evaluated at nodes bounding the compartments; the term  $\frac{dE}{R_1 dx}$  at the right hand side, which is introduced to describe the sum of extra transmembrane current of the compartment  $I_{comp}$ , can then be approximated as the derivative of the axial current induced by the applied field (Kamitani et al., 2001),

$$I_{comp} = I_a(e') - I_a(e'') = \frac{E(e')}{R_a(e')} - \frac{E(e'')}{R_a(e'')} \quad (8)$$

where  $e'$  and  $e''$  denote the two nodes bounding the compartment. If one end is a neuronal terminal,  $I_a(e^t)$  equals to 0 as current cannot flow through. If one end of the compartment is a bifurcation point, the  $I_{comp}$  values of the three compartments connected to that point are given by

$$I_{comp}^i = A^i \times \sum_{j=1}^3 I_a^j(e^0) / \sum_{j=1}^3 A^j, i = 1,2,3. \quad (9)$$

where  $A$  is the cross-sectional area of the compartment,  $i$  &  $j$  are indices of the 3 connected compartments, and  $e^0$  is the end of the compartment that is not attached to the bifurcation points. In other words, for any one of the three compartments connected to a branching point, its compartment current is given by the product of its cross sectional area and the overall current flowing

towards the branching point – the sum of axial currents of the three compartments – divided by the sum of the cross sectional areas of all compartments. The calculation is based on a rule of thumb, assuming that the intracellular potentials within a branching geometry has limited variability, and the compartment current was only determined by the axial resistance, which is inversely proportional to the cross-sectional area.

The computation scheme was implemented on NEURON (Hines et al., 2001) using Crank-Nicolson method (Crank et al., 1947) with HOC scripts; the compartment currents were attached as a distributed mechanism using model description language NMODL.

### **3.2.2 Discretization – mathematical convergence and intracellular potential uniformity**

In order to ensure that the calculation was valid after the implementation of the calculation scheme, supplementary examinations were taken following two principles: mathematically, simulated MPs should converge with increasing number of compartments; physically, a piece of conductive material should have uniform internal potentials when reaching steady state inside an electric field (for details see fig. 10).

In carrying out the test, the cell membrane was assumed to be insulating; a baseline compartment number was determined for each segment. This baseline was either the first integer greater than the ratio of the segment length over the minimum distance between two neighboring geometry defining points, or the one calculated using the  $d-\lambda$  rule, whichever being smaller (Hines et al., 2001). The MPs after a 300 ms-100V/m stimulation was then calculated with the baseline compartment number and another one two folds greater than the

baseline. The comparison between the two sets of MPs (fig. 4, black trail) would reveal whether simulation was converging; meanwhile, the intracellular potential (red trail), i.e. the sum of MPs obtained with baseline compartment number (blue trail) and extracellular potential would be monitored to confirm the uniformity of intracellular potential.

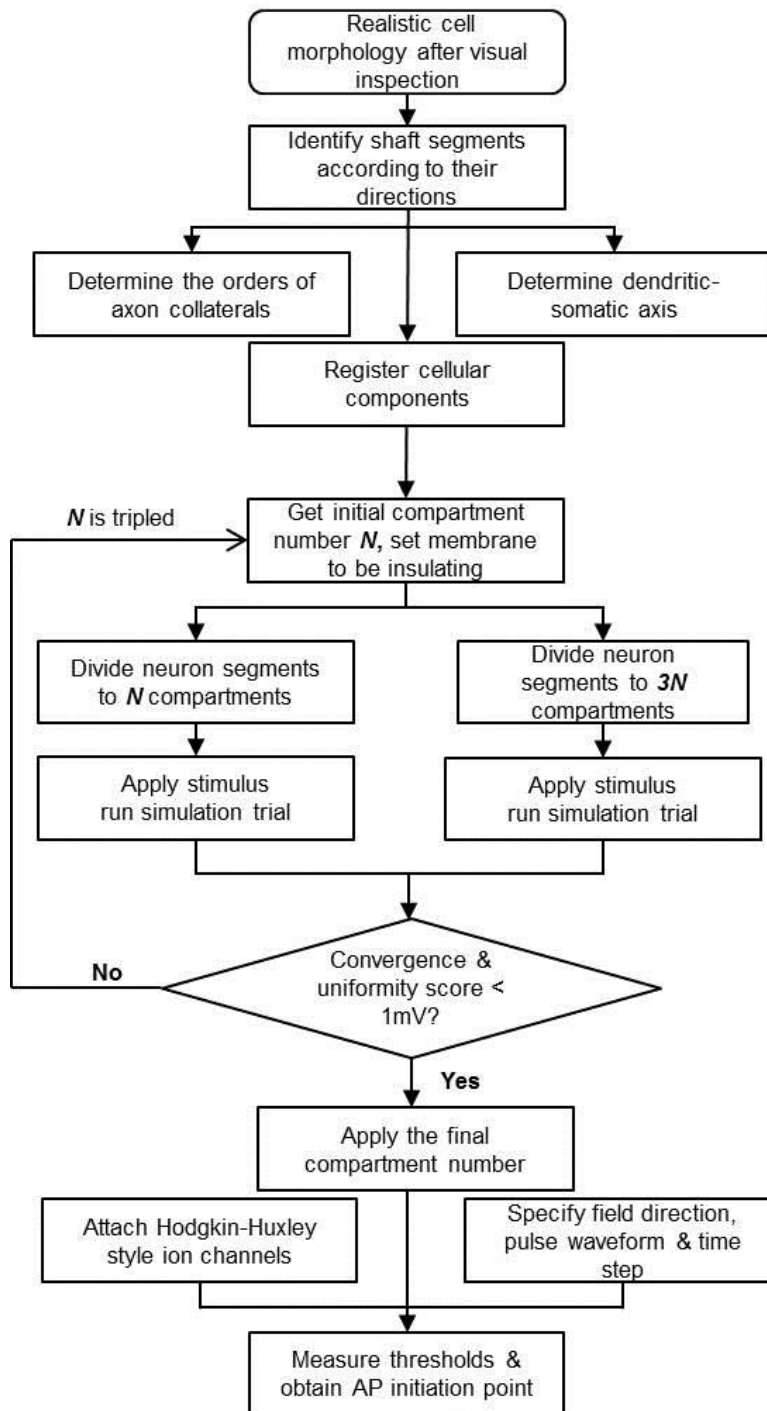


Figure 3 Implementation of the computation scheme on PCs with realistic cell morphologies. For each tested neuron, its morphology is firstly segmented and registered to different categories, including the apical dendrites, basal dendrites, soma, axon initial segment, axon hillock, myelinated axon, and nodes of Ranvier. The compartment number in each segment is then determined in an iterative manner. In the end, the compartment numbers are applied, the ion channels and other membrane properties are attached according to their categories, and the stimulation response to a pulse with specific direction and waveform is documented.

If either the convergence or the uniformity score which were quantified as the maximum difference between the two sets of MPs and the standard deviation of the intracellular potentials respectively, was greater than 1 mV, the entire process would be iterated with the compartment numbers tripled. For all the PCs, the final compartment numbers should restrain the convergence & uniformity scores within 1 mv and hence were deemed as adequate for later simulation of MPs.

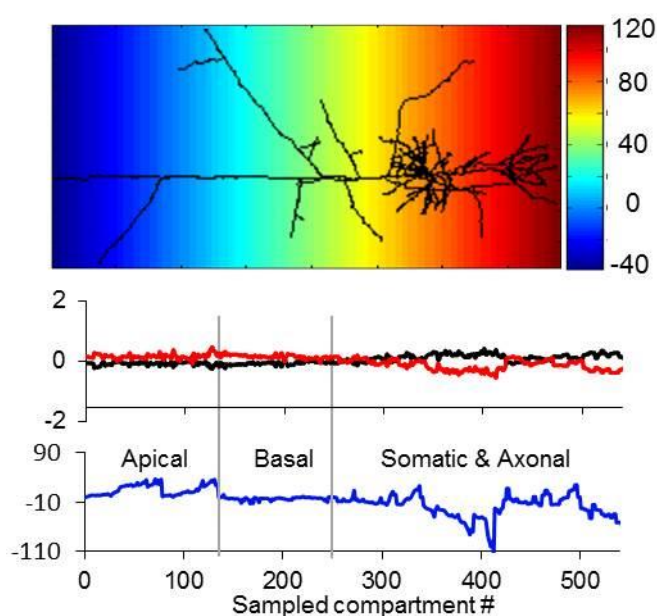


Figure 4 Convergence and uniformity scores of a tested cell at the end of the iteration. The morphology of a L2/3 PC is superimposed on the extracellular potentials, which is plotted in false color. The discrepancies between the two sets of MPs are plotted in black, while the intracellular potentials, i.e. the sum of MPs obtained with baseline compartment number (blue trail) and extracellular potentials, are plotted in red, with the unit of mV.

### 3.3 Representation of the membrane

In the first attempt of the model, a relatively simple membrane conductance model was adopted. The dendrites – both basal and apical – were set to be passive whereas the soma as well as the axon followed the Hodgkin-Huxley (HH) model (Hodgkin et al., 1952). In this model, two ion channels were



attached to the membrane; the voltage gated sodium channel sensitive to depolarization of the membrane potential was responsible for the onset of APs. On the contrary, the potassium channel would respond to the opening of the sodium channels open subsequently to bring about a hyperpolarization membrane current to reestablish the original membrane potential.

The HH model is easy to implement and was adopted in the preliminary tests. However, the simplicity of the model is obtained at the expense of the various details of the neuron morphology, most prominently being the myelin sheath. Myelin sheaths are non-conductive wrappings formed on the axon in order to facilitate AP transmission and accelerate the transmission speed.

To preserve this morphological feature of the pyramidal cells, a new mode was also studied (Mainen et al., 1996). All the ion channels in this model followed the HH style formalization,

$$I = \bar{g} \cdot m^x \cdot h^y (V_m - E) \quad (10)$$

where  $\bar{g}$  is the maximum conductance,  $E$  is the Nernst potential for different ions ( $E_{pas} = -65 mV$ ,  $E_k = -90 mV$ ,  $E_{Na} = 50 mV$ ,  $E_{Ca} = 140mV$ ),  $m$  and  $h$  are activation and inactivation variables, the dynamic of which are described by

$$\frac{dm}{dt} = \frac{(m_\infty - m)}{\tau_m} \quad (11)$$

$$\frac{dh}{dt} = \frac{(h_\infty - h)}{\tau_h} \quad (12)$$

The number of channels was significantly increased; the sodium conductance is given by

$$\alpha_m = \frac{0.182 \cdot (V + 25)}{1 - e^{\frac{-(V+25)}{9}}} \quad \beta_m = \frac{-0.124 \cdot (V + 25)}{1 - e^{\frac{-(V+25)}{9}}}$$

$$\alpha_h = \frac{0.024 \cdot (V_m + 40)}{1 - e^{\frac{-(V_m+40)}{5}}} \quad \beta_h = \frac{-0.0091 \cdot (V_m + 65)}{1 - e^{\frac{-(V_m+65)}{5}}}$$

$$m_\infty = \frac{\alpha_m}{\alpha_m + \beta_m} \quad h_\infty = \frac{\alpha_h}{\alpha_h + \beta_h}$$

$$\tau_m = \frac{1}{T_{adj}(\alpha_m + \beta_m)} \quad \tau_h = \frac{1}{T_{adj}(\alpha_h + \beta_h)}$$

$$N_m = 3 \quad N_h = 1$$

The potassium channel includes: 1, voltage gated potassium channel;

$$\alpha_m = 0.02 \frac{(V_m - 25)}{1 - e^{\frac{-(V_m-25)}{9}}} \quad \beta_m = -0.002 \frac{(V_m - 25)}{1 - e^{\frac{-(V_m-25)}{9}}}$$

$$m_\infty = \frac{\alpha_m}{\alpha_m + \beta_m} \quad \tau_m = \frac{1}{T_{adj}(\alpha_m + \beta_m)}$$

$$N_m = 1 \quad N_h = 0$$

2, muscarinic potassium channel ;

$$\alpha_m = 0.0001 \frac{(V_m + 30)}{1 - e^{\frac{-(V_m+30)}{9}}} \quad \beta_m = -0.00011 \frac{(V_m + 30)}{1 - e^{\frac{-(V_m+30)}{9}}}$$

$$m_\infty = \frac{\alpha_m}{\alpha_m + \beta_m} \quad \tau_m = \frac{1}{T_{adj}(\alpha_m + \beta_m)}$$

$$N_m = 1 \quad N_h = 0$$

3, calcium activated potassium channel.

$$\alpha_m = 0.01([Ca^{2+}]_i) \quad \beta_m = 0.02$$

$$m_{\infty} = \frac{\alpha_m}{\alpha_m + \beta_m} \quad \tau_m = \frac{1}{T_{adj}(\alpha_m + \beta_m)}$$

$$\tau_m = 1 \quad N_m = 1$$

In addition, calcium currents were also recruited, with the conductance given by

$$\alpha_m = \frac{0.055(V_m + 27)}{1 - e^{\frac{-(V+27)}{3.8}}} \quad \beta_m = 0.94 e^{\frac{V_m+75}{17}}$$

$$m_{\infty} = \frac{\alpha_m}{\alpha_m + \beta_m} \quad \tau_m = \frac{1}{T_{adj}(\alpha_m + \beta_m)}$$

$$\alpha_h = 0.000457 e^{\frac{-(V_m+13)}{50}} \quad \beta_h = \frac{0.0065}{e^{\frac{-(V_m+15)}{28}} + 1}$$

$$N_m = 2 \quad N_h = 1$$

The decay of intracellular calcium concentration is given by

$$\frac{d[Ca^{2+}]}{dt} = -\frac{10^5 \times I_{ca}}{96485} - \frac{[Ca^{2+}] - 0.0001}{0.2}$$

The adjustment of temperature is given by

$$T_{adj} = q_{10}^{\left(\frac{T-23}{10}\right)}, \quad q_{10} = 2.3 \quad (13)$$

where  $T$  is the room temperature under which the experiment is conducted. In our situation, the value was set to 37°C.

The maximal conductance values of the channels at specific neuronal components, including the dendrites, the cell body, the initial segment of axon, the axon hillock, the myelinated axon, and the nodes of Ranvier, together with

the axial resistance, membrane capacitance/resistance are given in Table. 3. The model showed merits in giving different neurons distinct firing patterns, each highly coherent to what was documented from electrophysiological experiments, but failed to preserve the morphological features of the axon.

Table 3 Membrane properties of components of PC. N.A.: not applicable, i.e. the channel is not inserted to the specific segments.

	Dendrites	Soma	Hillock	Initial Segment	Myelinated axon	Nodes of Ranvier
$R_a(\Omega \cdot cm)$	150	150	150	150	150	150
$g_m(pS/\mu m^2)$	0.033	0.033	0.033	0.033	0.033	200
$C_m(\mu F/cm^2)$	0.75	0.75	0.75	0.75	0.02	0.75
$\bar{g}_{Na}(pS/\mu m^2)$	20	20	30000	30000	20	30000
$\bar{g}_{K_v}(pS/\mu m^2)$	N.A.	200	2000	2000	N.A.	N.A.
$\bar{g}_{K_m}(pS/\mu m^2)$	0.1	0.1	N.A.	N.A.	N.A.	N.A.
$\bar{g}_{K_{Ca}}(pS/\mu m^2)$	3	3	N.A.	N.A.	N.A.	N.A.
$\bar{g}_{Ca}(pS/\mu m^2)$	0.3	0.3	N.A.	N.A.	N.A.	N.A.

### 3.4 Segmentation and registration of axonal components

In the original model, the axon of the cell was replaced by an idealised one, which constitutes a number of long cylinders connected in series. To empower the computation with realistic neuronal morphologies, the cell model was transformed to accommodate complex axon tortuosity and ramifications. In the meantime the dendritic-somatic axis of the whole cell, the segments constituting the axon shaft and the orders of axonal collaterals were also determined. A detailed illustration of this transformation is given in fig. 5.

The axon shaft (colored in red) was firstly identified in an iterative manner. At the beginning, the only axonal segment directly connected to the cell body was labelled as the first shaft segment; its direction was obtained by principle component analysis (PCA) on all the points included. The calculation of segment directions was then carried out on the child segments. The one most parallel to the parent would be also labelled as a shaft segment and the above procedures were repeated until it reached a terminal or a major turning.

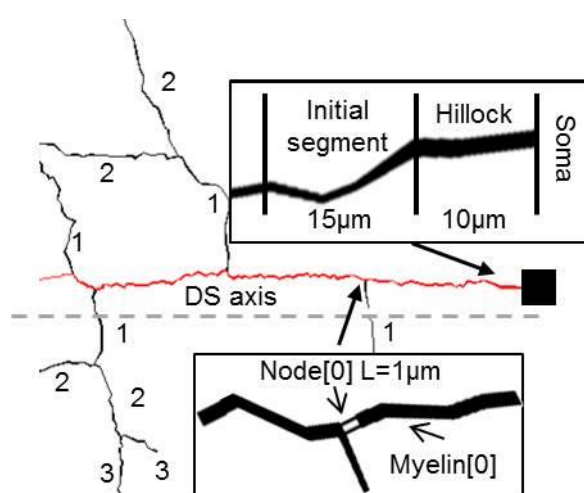


Figure 5 Registration of axonal compartments. Part of the axon morphology is depicted; the axon shaft is coloured in red; the DS axis of the cell is sketched in a dashed line near the shaft; orders of axon collaterals are labeled next to each segment.

The dendritic-somatic (DS) axis of the cell was computed after all segments had been identified, by PCA of the whole shaft. Following this process, the orders of the collateral segments (numbers labelled beside) were determined – collaterals connected to the shaft would have order of 1; segments linked to order 1 collaterals would be assigned with order 2 and so on. In the end, registration of axonal components, including the hillock, the initial segment, the myelinated segments and nodes of Ranvier, were conducted on the axonal morphology. The components were segmented from morphology: the first 10

$\mu\text{m}$  of the initial shaft segment was marked as the axon hillock; the following section with the length of  $15 \mu\text{m}$  was then converted to the initial segment; thereafter, the remaining segments were identified as covered by myelin, the nodes of Ranvier were located to segment ends where the axon bifurcates or terminates (Grill et al., 2008). After the registration of different components, the corresponding membrane properties and ion channels were attached. The ion channels that were presented in the dendritic components, namely the muscarinic potassium channel, the calcium-dependent potassium, the voltage-gated sodium channel and the high-voltage-activated calcium channel, were attached to apical and basal dendrites as distributed mechanisms with the region-specific maximum conductance values applied. Likewise, the channels and the corresponding maximum conductance values of the cell body, the hillock, the initial segment of axon, the nodes of Ranvier and the myelins were applied on the segments that were registered under these categories. The geometry of the hillock and the nodes of Ranvier were altered – the diameter of one end of the hillock, which connected to soma, was fixed at  $40\% \times$  soma diameter, the other end remained unchanged, the diameters of the compartments in between were linearly interpolated from the two ends; the diameters of the nodes of Ranvier were 90% of the original sizes.

### **3.5 Measurement of stimulation thresholds and polarization lengths**

The author measured AP thresholds, with regard to different field directions, pulse durations and morphologies, via running a series of simulation trials (fig. 6). In the beginning of a single trail, axial current induced by stimulation was set to zero, and the MP was allowed to evolve for 10 ms without the intervene of applied stimuli. The stimulation then came into effect, changing the axial

current accordingly and driving the MP changes. The trial was then continued until the end, which was 110 ms after the onset, with the number of APs noted. Meanwhile the MPs of all segments were monitored; the activation point was marked to the compartment which showed the earliest AP. The intensity of the field was fixed within a single trial but was varied across trials; the AP threshold was the minimum field strength in V/m to trigger at least 1 AP.

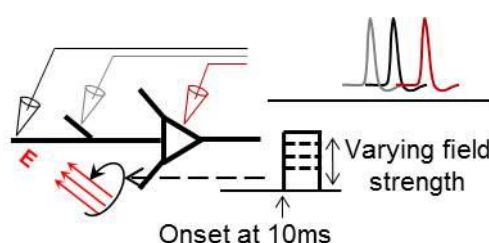


Figure 6 Simulation trials for threshold measurement.

The half-interval search method was adopted in finding the threshold for a specific pulse duration and field direction. For example, in searching for the threshold of a PC to a  $0^\circ$ -100ms stimulus, an initial field strength of 70V/m was applied in the simulation trial. If an AP was triggered, the strength would be reduced by 40 V/m and another trail would be initiated. Should no spike was recorded, the strength would be increased but by 20 V/m – half of the original search interval. This procedure was repeated until the search interval was reduced to 1V/m and the minimum strengths value that could give rise to AP firing was identified. For short duration ( $<10$ ms) and TMS waveform stimulation, the initial strength and the search interval were 270V/m and 100V/m respectively.

## **CHAPTER 4 Measurement of responses of pyramidal cells to long-duration uniform field stimulation**

PCs, otherwise regarded as the principle cells in the cortex, have been specifically attended in the investigation of the EM stimulation mechanism. In the canonical cytoarchitecture of the mammalian neocortex, PCs make up the majority of the excitatory connections, with the exception of stellate cells in L4. In the primary motor cortex where the L4 is missing, PCs are the sole mediator excitatory transmissions. As the effectiveness of EM stimulation, upon administration on the motor cortex, is characterized by excitatory responses such as involuntary limb movement, it is generally believed that EM stimulation influences the motor cortex via direct interference on the cellular activities of the PCs.

In the present study, the author deployed the simulation scheme described in Chapter 2 on a number of PCs that were harvested from animal subjects. It was aimed that, through monitoring the cellular responses towards stimulation, the stimulation thresholds, the initiation points and the somatic polarization lengths, a comprehensive account of the stimulation effectiveness and its sensitivity to parameters as field direction and pulse duration can be provided. The inclusion of PCs from two different categories in the subject pool also gave us the opportunity to assess the inter-layer differences. Last but not least, the results *in silico* were compared with data from *in vitro* experiments to further substantiate the validity of the approach.

### **4.1 Pyramidal cells**

Morphologies of 40 neurons with relatively complete axon trees were downloaded from NeuroMorpho.org (Ascoli et al., 2007). These morphologies



had been reconstructed from biocytin-stained somatosensory cortex slices of Wistar rats (Wang et al., 2002). Among them, 27 were labeled as from L2/3, and the remaining were identified as from L5 PCs. The author employed manual inspection on all the downloaded neurons to ensure that they were free from reconstruction artifacts, such as axon connecting back to soma, irregularities in diameters, etc. However, distortion in the z-direction, which was probably introduced by stacking of slices, appeared to be inevitable for most cells. An example of such artifacts is shown in fig. 7. Under certain circumstances, a V-shape turn (circled geometry) could be produced in the z-direction, which gives the hosting neuron an abnormal susceptibility. As a matter of fact, in the previous version of the simulation where HH model was used to represent axons, one of the cells had a threshold as low as 1 V/m, which was clearly not possible *in vivo*. Few cells – with relatively simple

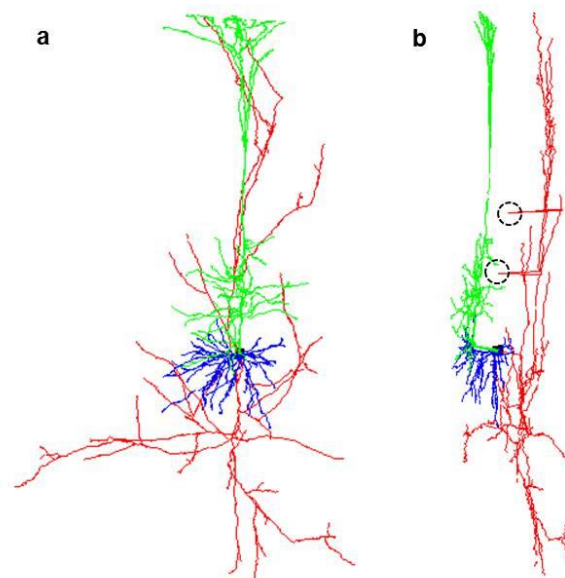


Figure 7 Z direction artifacts on a L5 PC. The front view (a) and the side view (b) of a neuron are presented. Note that the various V shape turns into the Z-direction which can only be perceived in the side view but not the front view.

morphologies – did not suffer from such artifacts, but the number was too small for statistical analysis. In order to prevent the distorted morphology from contaminating the simulation results while maintaining an adequate number of samples, all neurons were squashed from 3D to 2D. The squashing process has the potential to affect the length of different segments in different ways, and thus would not preserve the original electrotonic structures of the cells. Nevertheless, the thresholds from the 3D intact neurons were examined to be almost the same as the 2D version. Due to these reasons, 2D neurons were used in simulation.

A short statistical description of these two types of neurons after the process is provided in Table 4. Generally, the L5 cells were larger in size, demonstrated by the average diameters of segments, and more complex in geometry, evident by the greater number of axonal and dendritic segments.

Table 4 Summary of two types of PCs tested in the simulation. Standard deviations are enclosed in parentheses. a: curve index is calculated as the distance between the two ends of a segment divided by the overall length, and is used to quantify tortuosity. Differences between layers are evaluated with one-way ANOVA: \* =  $p < 0.05$ ; \*\* =  $p < 0.01$ .

		Layer 2	Layer 5
Soma	Diameter ( $\mu\text{m}$ )	16.71 (2.51)	27.23 (3.89) **
Axon	Number of segments	29.59 (20.79)	56.23 (32.09)**
	Length ( $\mu\text{m}$ )	82.66 (106.51)	81.77 (110.31)

	Curve index (%) †	93.55 (7.30)	93.84 (7.52)
	Diameter (µm)	0.37 (0.20)	0.46 (0.59)**
	Arborization points	14.30 (10.40)	27.62 (16.04)**
	Maximum order of collaterals	3.85 (2.03)	7.69 (2.72)
Apical Dendrite	Number of segments	37.22 (16.88)	141.00 (86.86)**
	Length (µm)	41.74 (36.96)	37.18 (60.29)*
	Curve index (%)	86.28 (11.97)	90.18 (11.82)**
	Diameter (µm)	0.83 (0.53)	0.97 (1.04)**
	Arborization points	18.11 (8.44)	70.00 (43.43)**
Basal Dendrite	Number of segments	35.52 (14.58)	51.54 (29.45)*
	Length (µm)	38.48 (32.73)	44.95 (49.60)**
	Curve index (%)	87.16 (11.59)	91.20

			(9.87)**
	Diameter ( $\mu\text{m}$ )	0.79 (0.43)	0.89 (0.69)**
	Aborization points	15.33 (7.14)	22.46 (13.90)*

## 4.2 Stimulus orientation and duration

The measurement was carried out for each neuron in 12 different angles, from  $-150^\circ$  to  $180^\circ$  with interval of  $30^\circ$ , and with angle fixed at  $0^\circ$  from various pulse durations, ranging from 0.1 ms to 100 ms. Additionally, the thresholds of cells for TMS pulses were filed; the strengths of TMS pulses were always marked as the peak intensity of the first phase. The time step of each trial was associated with the pulse duration: 5  $\mu\text{s}$  time step for 10-100 ms stimuli, 1  $\mu\text{s}$  for  $< 10$  ms and TMS pulses. The time steps were determined from pilot trials conducted on a selected population of cells such that further reduction of the values would produce a no more than 1% difference in the obtained thresholds

## 4.3 Statistical analysis

Multi-way ANOVA with repeated measures was used to detect the differences in measured thresholds. Post hoc analysis was conducted with Tukey's honest significant difference (HSD) method to quantify the significant effects ( $p < 0.05$ ). Sensitivities of threshold to field direction and pulse duration were studied with multi-way ANOVA for with-in subject analysis, and were quantified using pairwise t-test, variance modified with Bonferroni-Holm correction. All tests were performed with R 3.1.1.

## 4.4 Results

### 4.4.1 Anisotropy of stimulation thresholds and polarization lengths

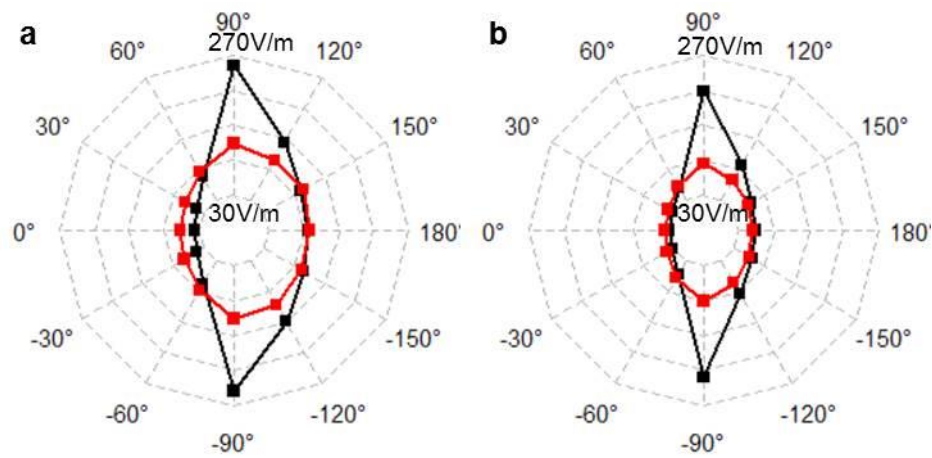


Figure 8 Thresholds and AP initiation points with respect to field directions. (a) & (b) depict the thresholds of L2/3 & L5 PCs respectively. Values obtained with idealised and realistic axons are colored in black and red.

Fig. 8a&b depict the stimulation thresholds with regard to different field directions. Measurements obtained from all angles had a symmetrical distribution across the DS axis – the average thresholds recorded with the field rotated clockwise or counterclockwise were indistinguishable as long as the numerical degree was the same. But this axial symmetry was rarely spotted in a single neuron (fig. 9a). The anisotropy of cells with realistic morphologies was less prominent, compared with the ones with arbitrary axons (cells with arbitrary axons:  $p < 0.01$  between all angles except its counterpart across the DS axis; cells with realistic morphologies:  $p < 0.05$  from  $0^\circ$ ,  $\pm 30^\circ$  to other angles).

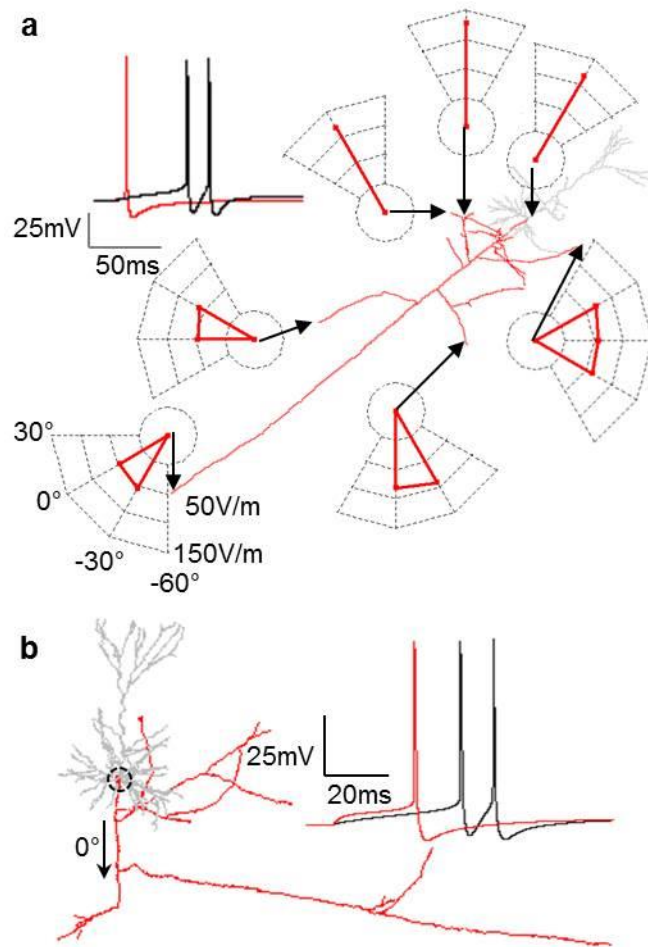


Figure 9 Thresholds, initiation points and AP waveforms. (a) Thresholds and corresponding initiation sites of a L2/3 PC with respect to different field orientations. The axonal and dendritic components are colored in red and grey respectively. The dynamic of MP of soma under  $0^\circ$  stimulation (red) is overlaid with the firing patterns under 30 pA current injection to soma (black). Note that reducing the current amplitude would only delay the onset of APs until no activation could be initiated; the doublet spiking pattern is always preserved. (b) Overlay of spiking patterns induced by  $0^\circ$  stimulation and 50 pA current injection to soma. Note that the initiation point of  $0^\circ$  stimulation is also located at the cell body.

The minimum threshold was located at  $0^\circ$ , which is in line with the observation that monophasic TMS has the lowest MT when applied in the P-A direction by activating neurons located on the sulcal wall. The maximum value was from either  $+90^\circ$  or  $-90^\circ$ , although due to the large variance, it was not significantly different from other angles. The ratio between the maximum and the minimum was 2 (L2/3) & 2.5(L5) for realistic cells, much smaller than that

of cells with arbitrary axons. The mild anisotropy and the small gradient with regard to field direction seems to agree with the MTs and motor responses recorded from TMS experiments, which was only marginally changed by slight deviations in field directions.

#### 4.4.2 Locations of initiation points

The composition of AP initiation points on arbitrary axon was highly monotonic: between  $\pm 60^\circ$  the terminal of axon shaft, others the soma. But with realistic axons a more dispersed picture was presented (fig. 10). The presence of the terminal of axon shaft extended to  $+90^\circ$ , but the monopoly in directions from  $-60^\circ$  to  $+60^\circ$  was no longer preserved; activation from soma was marked in almost all angles; but the majority of initiation points were occupied by terminals of axon collaterals, and APs kindled there could always transmit back to soma. Quite unexpectedly, the firing pattern was uniform across all initiation mechanisms. Even for neurons which showed a doublet firing pattern during current injection to soma, the application of a single pulse can only

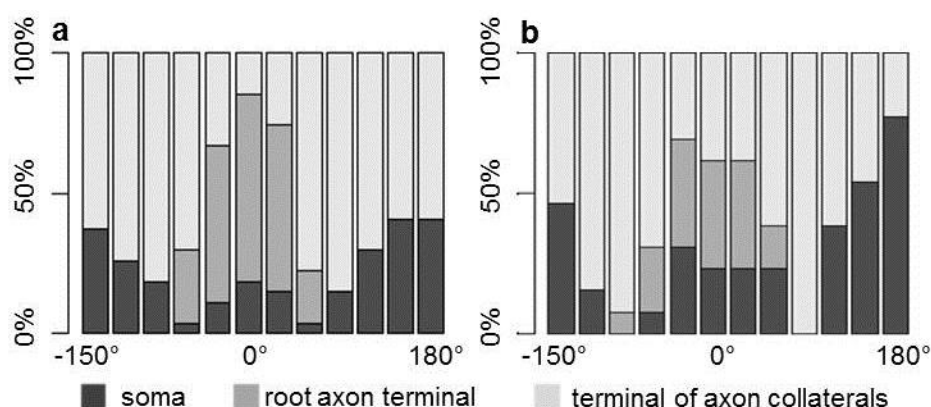


Figure 10 AP initiation points. Constitutions of three categories of AP initiation points, namely terminal of axon collateral, terminal of shaft axon, and cell body, obtained from L2/3 and L5 PCs with realistic axons are plotted in (a) & (b) respectively.

produce one AP, regardless of the initiation site (fig. 9a&b).

#### **4.4.3 Influence of cell type**

Further revealed by the statistical analysis was the difference between layers: L5 PCs always had lower thresholds ( $p < 0.001$ ), except when the field was perpendicular to the cells. Interestingly, thresholds from cells with arbitrary axons were not always different from neurons with realistic axons ( $p < 0.01$  for  $\pm 30^\circ$ ,  $\pm 90^\circ$ ,  $\pm 120^\circ$  &  $0^\circ$ ). The lack of significant difference at  $\pm 60^\circ$  might be explained with the interactions between the threshold values at these two angles; but for other angles, it was observed that a substantial amount of activation points were located at the soma. The similarity could be caused by the fact that, when AP was initiated at the cell body, dendritic components which were preserved in all neurons played a more important role than axon.

#### **4.4.4 Transmission of initiation points in association of pulse duration**

Fig. 11 shows the threshold values vs pulse lengths. With the duration gradually decreasing, the difference in thresholds between different layers ( $p < 0.05$  for 1 ms,  $p < 0.01$  for all other durations) were magnified. Likewise fast expanding was the standard deviation, which almost stayed proportional to the mean values throughout the various pulse durations. The AP initiation sites, as shown in fig. 11c, were not stationary. With pulse duration decreased to 0.1 ms, many of the initiation sites were relocated from cell bodies to the terminals of axon shaft, but the constitution of terminals of axon collaterals remained almost unchanged. Fig. 11d provides one such example, which also illustrates a change of gradient accompanying the relocation. On the other hand, shift of activation point and the non-smoothness were never observed on cells with arbitrary axon.



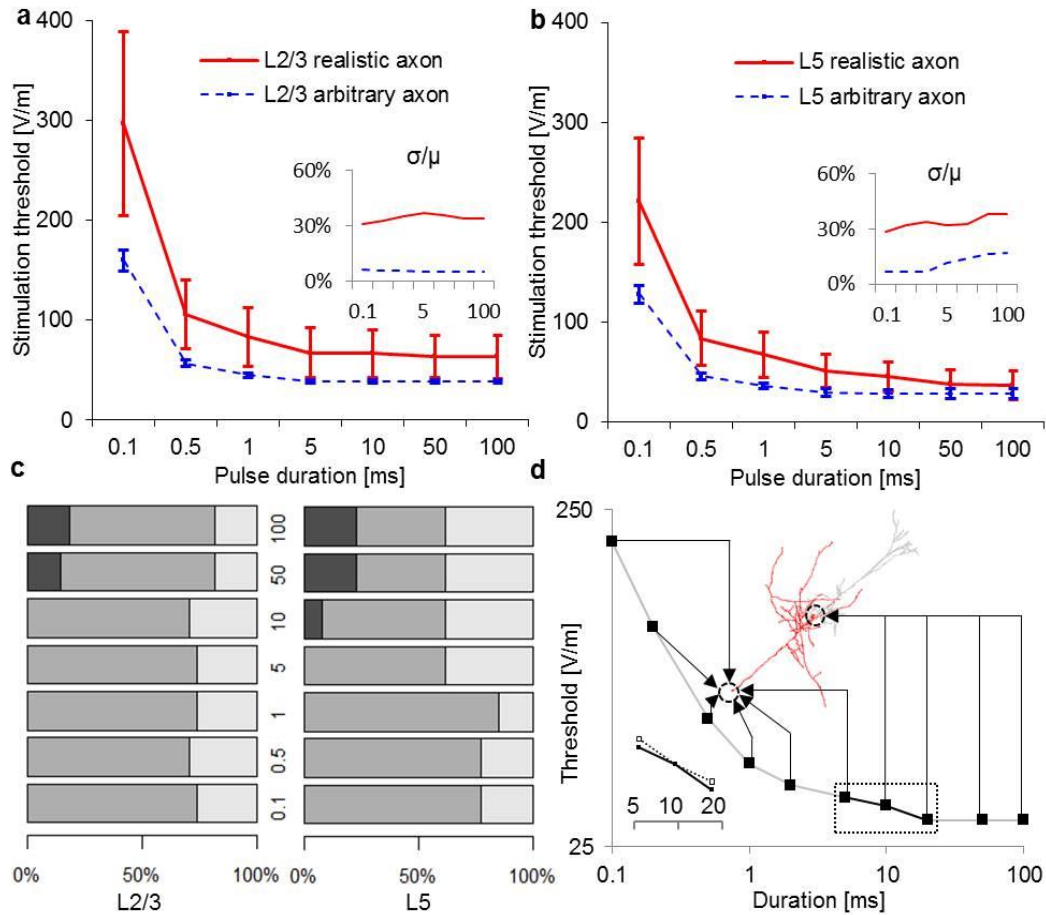


Figure 11 Stimulation thresholds of L2/3 (a) and L5 (b) PCs with respect to pulse durations. The ratios of standard deviations are shown over the mean values. The initiation points are shown in (c), with the same notation as that in fig. 10c. The threshold-duration curve of a L5 PC is graphed in (d), with the corresponding initiation sites labelled. In addition to the durations in a & b, the thresholds for 0.2 ms, 2 ms, and 20 ms stimulation were also tested. The thresholds of 5 ms, 10 ms & 20 ms stimuli are magnified in the side window with the linearly interpolated values marked with open squares and dashed lines.

#### 4.4.4 Comparison of simulation results with in-vitro data

For one of the tested field directions,  $0^\circ$ , the thresholds of L2/3 as well as L5 PCs *in vitro* had been documented in a former experiment. In brief, cortical neurons were collected from rat brain slices; a uniform electric field was supplied using two arrays of electrodes; the field direction was from higher to lower layer of the cortex; stimulation thresholds were recorded with the pulse duration fixed at 100 ms; polarization lengths, quantified as the amount of MP changes produced by a unit of field strength before AP firing, were also

monitored. As the experiment setup was equivalent to our simulation, these cellular responses were utilized to consolidate our model. The qualitative assessment that L2/3 PCs have higher thresholds was reproduced in our simulation.

Moreover, a visual inspection of the thresholds and polarization lengths recorded *in vitro* versus *in silico* is given in fig. 12. On the limited data available, the overlap between the *in vitro* readings and simulation results apparently suggest that validity is improved by the introduction of realistic morphology.

#### **4.5 Discussion**

In this study, the author developed a simulation scheme which can host highly detailed physiology and morphological properties of neurons and can be implemented on two groups of PCs, one from L2/3 and the other from L5. The stimulation thresholds of simulated cell were then measured with different input parameters and manipulation of cell morphology; the corresponding AP initiation points were also documented. Several findings are worth noting: the variance among PCs, the minor anisotropy in thresholds, the non-smooth strength-duration curve, and the dependency of the activation site on pulse length. Unprecedented by previous simulation works, they seem unique to the presented model. But by studying the localization of the initiation sites and the disparities between the thresholds obtained from arbitrary and realistic axons, it might be recognized that the excitability is shaped by the competition between all activation-capable segments, and the subsequent interplay of various factors – the alignment between the segment and the field, the diameter, the pulse waveform, and the topology.

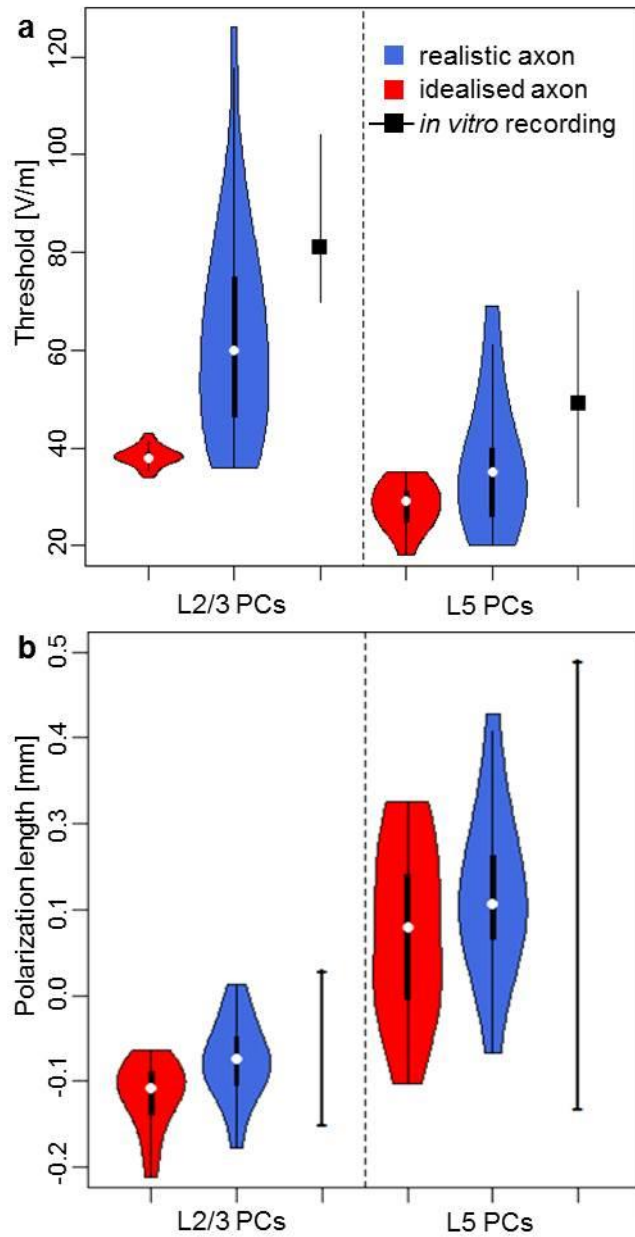


Figure 12 Comparison between thresholds (a) and polarization lengths at soma (b) measured in silico and in vitro. Simulated values are displayed in violin plots, with the kernel densities denoted by the shaded areas, mean values by open circles, and quartiles by bold bars. The ranges occupied by in vitro recordings are depicted in vertical bars, with the mean values (if available) labelled by filled squares.

#### 4.5.1 Competition between activation-capable components

Among all axonal components, the terminals, the bifurcation points and the initial segments connected to soma represent morphological discontinuities

which allow stimulation to induce changes in MP. With active ion channels attached, these segments are potential candidates for activation. Dispersed all over the axon, each of them has a specific local geometry hence a unique predisposition – the better parallelism/greater diameter/longer pulse duration, the more likely to initiate AP. For a stimulus with a particular waveform and direction, for each of the candidates a minimal intensity is required for AP initiation; the threshold of the whole cell is indeed the minimum of the “minimal intensities”, obtained from the candidate most favored by the applied pulse.

In the light of numerous potential initiation sites, the influence of the factors becomes manifold. The threshold is no longer directly associated with the alignment between the cell and the field as in the case of arbitrary morphology. Instead, the effect is reduced to select the ones with the optimal conformities in orientation. The size plays a pivotal role in the value of the threshold – the difference between cells, being L5 PCs larger than L2/3, and within cells, being the axon collaterals marginally smaller than the shaft, were reflected in the measured thresholds. Similarly complicated is the relation between the initiation site, the threshold and pulse duration. With arbitrary axon, the initiation site is stationary and the strength-duration curve is smooth and similar to the “chronaxy-rheobase” curve intrinsic to current injection. But with realistic morphology, sometimes more than one aligned segments are present for a specific direction. Although for each of them the correlation between threshold and duration may still be smooth, exactly the same strength-duration curve is not possible due to their distinct geometries. If they intercept with one another, the activation point is different before and after the

interception point; the threshold-duration function is composed of the lowest segment of all the curves.

#### **4.5.2 The initiation points**

The majority of the AP activation points identified in the presented study were located to the termination points of axonal segments, either of the shafts or collaterals. This is coherent with the deduction in previous researches that the terminal presents the most effective type of morphological discontinuities in raising local membrane potential (Arlotti et al., 2012; Nagarajan et al., 1993; Pelletier et al., 2015; Rahman et al., 2013; Rattay, 1999). Regarding which type of terminal is the major activation site, it seems that the terminal of shaft is only favored when the pulse is brief and, more importantly, when the field is parallel to the neuron. But since pyramidal cells *in vivo* are only coarsely aligned and a substantial amount of them are activated from collaterals even when perfect alignment is achieved and pulse length is close to the values used in TMS and TES, it might be expected that activation through this mechanism makes up for a substantial proportion the stimulation-evoked excitation.

The localization of initiation point to the terminals could explain the previous observation, that by voluntary contraction the amplitude of the descending volleys in the pyramidal tract is enhanced, but the minimum stimulator output required to initiate the volley is not influenced by this process. Presumably, the excitation of terminals release excitatory transmitters to the PTNs; during voluntary contraction, the soma MP of PTNs are slightly depolarized hence the same amount of transmitter release could subsequently lead to enhanced descending volleys; but the excitability of the terminals is independent of soma MP, thus maintaining the original threshold.

Soma has been argued as another potential location to host AP initiation, because the dendritic and somatic components are geometrically asymmetric in pyramidal neurons (Pashut et al., 2011; Yi et al., 2014). Although several cases of soma-initiated AP firings were recorded in long-duration stimulation, their distribution across angles implies that they are contingent on the combination between the cell and the field, in which none of the terminals have a good alignment with the applied field. In fact, this is probably the situation presented in the earlier research regarding cell activation by circular TMS – an arbitrary axon with no collaterals was used and all firing-capable components were arranged in the same direction; the field was produced by the round coil, and could not be aligned to the cell; consequently, the cell body became the preferred site of initiation. On the contrary, when the field is quasi-uniform and is aligned with the cell, as in the scenario of our simulation, the activation points were always located at the terminals.

A number of the tested PCs had bent axon shafts (for instance, fig. 16b), but APs were never observed to be triggered nearby; twisting arbitrary axon has shown no effect on threshold. These facts manifestly suggest that bending, at least when confined within myelinated segments, can hardly give rise to spikes. Hence the only possible scenario for APs to be evoked at a bending point, which has been asserted as the activation mechanism for PTNs, is when the axon takes a sharp turn at a node of Ranvier. With this geometry, the bending point could be taken as equivalent to a terminal, as both can cut off the axial current induced by stimulation. Notwithstanding the mathematical equivalency, several prerequisites are necessary for the proposed scenario to take place: the

bending must be abrupt, and again the cell should be strictly parallel to the field, both hard to be fulfilled.

To test the feasibility of activation under this situation, the author measured the polarization lengths of the terminal and the bending point of an idealized neuron (fig. 13). The bending point and the terminal present in the simplified neuron have the same length, diameter and membrane properties. Throughout all the tested angles, the bending point has lower depolarization values than the nearby terminal in response to the subthreshold stimulation until the bending angle is greater than  $80^\circ$ , which could not be expected from cells in vivo. Moreover, histological studies have identified extensive axon collaterals attached to the PTNs, which will further impede firing. Together, all these factors would render activation of the bending point on PTNs difficult to be achieved, which may explain the absence of D wave in the motor responses caused by PA direction-MT intensity TMS pulses.

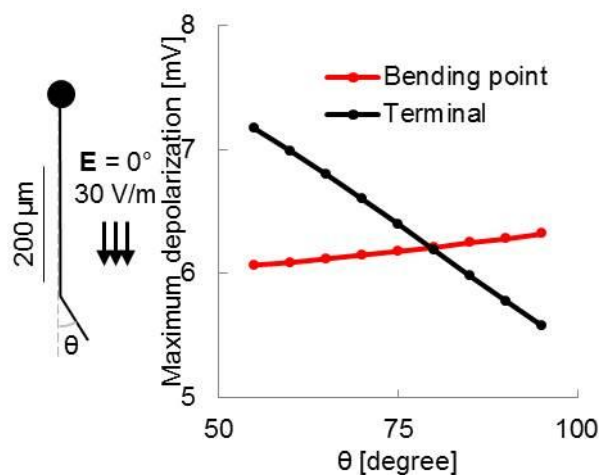


Figure 13 Maximum depolarizations of the bending point and the terminal during  $0^\circ$ -100 ms stimulation with bending angle increased from  $55^\circ$  to  $95^\circ$ .

### **4.5.3 Verisimilitude of cable theory-based simulation**

Recently the accuracy of the cable theory-based simulation approach in capturing the dynamics of MP has been challenged. As the influence of the field produced by the spontaneous activity of the neuron is ignored during calculation, the membrane potential values, especially those close to the cell body, could suffer from distortion. Contrary to the proposed bias, between the simulated and experimentally measured neuronal excitability a high resemblance is recorded: not only the qualitative difference was preserved, but the threshold and polarization length values were very close as well. The similarity in numerical values together with the paralleled patterns of TMS thresholds seems to imply that, when an adequate knowledge regarding cell physiology and morphology is available, the cable-theory based numerical calculation strategy can give quantitatively accurate prediction of neuronal responses to stimulation. The proposed verisimilitude would then allow simulated cell responses to be integrated into the neural circuitry to evaluate the roles played by different groups of neurons in the induced effectiveness and elucidate the underlying mechanism of stimulation modalities. Nonetheless, the number of cells reported in the *in vitro* study was small; this hypothetical capability of the simulation would require further consolidation.

### **4.6 Concluding remarks**

The simulated thresholds had a minor anisotropy and reached the minimum when the field direction was parallel to the dendritic-somatic axis; L5 PCs always had lower thresholds but a significant variance was also present within layers; reducing pulse length can magnify the threshold values as well as the variance. The dependence of the initiation sites on both the orientation and the



duration of the stimulus implied that the cellular excitability might be understood as the result of the competition between various firing-capable axonal components, each with a unique susceptibility determined by the local geometry. Due to their higher excitabilities, the terminals of axonal components are more likely to be the activation initiation point than the cell body or bending points. Moreover, the measurements obtained in simulation intimately resemble the recordings in physiological and clinical studies, which suggests that, with a minimum simplification of the neuron model, the cable theory-based simulation approach can have sufficient verisimilitude to give quantitatively accurate evaluation of cell activities in response to the externally applied field.

## **CHAPTER 5 Measurement of TMS thresholds and sensitivity to morphological features**

In chapter 4 the author examined the influences of field direction and pulse duration on the susceptibility of the cell. The results consolidated the simulation as a useful tool in reproducing cellular activities evoked by stimulation and also shed new light on the working mechanism of the electromagnetic stimulation. Nevertheless, it was observed that the pulse waveform has a major impact on the stimulation efficacy, as the threshold values, together with the location of initiation points, could be totally distinct with the different durations. The minimum duration tested in Chapter 3 was 0.1 ms, a number very close to the lengths of TMS pulses. Yet, in real life application, the pulse waveform is very distinct from the rectangular pulses evaluated. For TMS, the RLC circuit generates rather irregular pulse waveforms which comprise two “phases”. To accommodate the realistic stimulation pulse and in turn to empower the simulation to study and to explain the observations made in clinical tests, the stimulation thresholds of cells towards TMS pulses were measured. Additionally, the influence of axon geometry, which has been largely undermined in previous studies, further addressed in this section via manipulation of cell morphology.

### **5.1 Stimulation waveforms of commercially available device**

Theoretical calculations of the electric field induced by magnetic stimulation have been presented in previous studies (Nagarajan et al., 1993). For a circular coil, the vector potential  $A$  in a plane parallel to the coil at a distance  $d$  has only an azimuthal component  $A_\phi$ , which can be expressed as a function of elliptic integral:

$$A = A_{\phi} = \frac{\mu I}{\pi \alpha} \sqrt{\frac{a}{r}} \left[ \left(1 - \frac{\alpha^2}{2}\right) K(\alpha) - E(\alpha) \right] \quad (14)$$

$$\alpha = \sqrt{\frac{4ar}{a^2 + (a+r)^2}} \quad (15)$$

where  $K$  and  $E$  are complete elliptic integrals of the first and second kind respectively,  $a$  is the radius of the coil, and  $r$  is the distance of the measurement point from the axis of the cylindrical symmetry. The induced electric field is given by the partial derivative of the vector potential with respect to time,

$$E_i = -\frac{\partial A}{\partial t} \quad (16)$$

which can be further decomposed into a temporal component and a spatial component.

$$E_i = -\frac{dI}{dt} \times \frac{\mu}{\pi \alpha} \sqrt{\frac{a}{r}} \left[ \left(1 - \frac{\alpha^2}{2}\right) K(\alpha) - E(\alpha) \right] \quad (17)$$

The spatial component is purely decided by the geometrical parameters and is independent of the stimulus waveform. As a result, the spatial distribution of the induced electric field from a multi-turn coil is the superposition of the fields due to each turn in the coil; the induced field of a figure of “8” coil is the superposition of the field profiles of two circular coils. In the present study, the spatial component was set as a pseudo parameter, so that its product with the peaks of the waveforms would be the field intensity specified by the user.

The temporal component is dependent on the manufacture’s design of the RLC circuit. In this study, the author adopted the waveforms of the monophasic and the biphasic pulses of a Magstim Rapid<sup>2</sup> stimulator.

For the monophasic, i.e. overdamped stimulus

$$\frac{dI}{dt} = (\delta w_n + w_d) \exp(-\delta w_n + w_d t) - (\delta w_n - w_d) \exp -(\delta w_n - w_d t)$$

(18)

for the biphasic, i.e. underdamped stimulus

$$\frac{dI}{dt} = \exp(-\delta w_n t) \cdot (w_d \cos(w_d t) - \delta w_n \sin(w_d t))$$

(19)

where  $\delta$ ,  $w_n$ ,  $w_d$  are the damping ratio, resonant frequency damped frequency of oscillation respectively. For the monophasic pulse, the product of the first two parameters  $\delta w_n$  were measured to be  $9.09 \text{ ms}^{-1}$ , the third parameter  $w_d$  was  $7.23 \text{ ms}^{-1}$ ; for the biphasic pulse,  $\delta w_n$  was  $1.27 \text{ ms}^{-1}$ ,  $w_d$  was  $12.51 \text{ ms}^{-1}$ .

## 5.2 Treatment of axon morphology

### 5.2.1 PCA based unravelling

Neurons included in the present study usually have segments – especially the long ones – that are tortuous. The tortuosity could be intrinsic, being the natural result of neuronal growth, or produced by tissue shrinkage during the collection process. To quantify the influence of segment tortuosity on the responsiveness of neuron to EM stimulation, the author has adopted an unraveling procedure that smooth the neuronal segments while retaining their overall length (Anwar et al., 2009).

The unraveling was performed using a moving window algorithm for each segment: assume that the window was of size  $N$  and that it was running on a branch of  $M$  points. The window was centered on the first point of the branch to be corrected (call this point's index  $p$ ), taking the  $N/2$  previous points and  $N/2$  next points. Hence all the points between  $p-N/2$  and  $p+N/2$  were fitted by

a direction vector  $\vec{D}_p$  using PCA. At the boundaries (if  $p < N/2$  or  $p+N/2 > M$ ) the window was truncated.

The moving window ran first on the tortuous neuron, computing all the direction vectors for each segment in the branch, and then updated the directions of the segments. Starting from the first one and moving to the end, the segments were aligned with the main direction computed for that point and the coordinates of the point P+1 then became:

$$\begin{pmatrix} \hat{x}_{p+1} \\ \hat{y}_{p+1} \\ \hat{z}_{p+1} \end{pmatrix} = \begin{pmatrix} \hat{x}_p \\ \hat{y}_p \\ \hat{z}_p \end{pmatrix} + \|\vec{V}_p\| \frac{\vec{D}_p}{\|\vec{D}_p\|}, \quad \vec{V}_p = \begin{pmatrix} \hat{x}_{p+1} - \hat{x}_p \\ \hat{y}_{p+1} - \hat{y}_p \\ \hat{z}_{p+1} - \hat{z}_p \end{pmatrix} \quad (20)$$

The window size was adjusted to various numbers (3,5,7,9) to increase the reach of the neuron segments as well as to decrease in the tortuosity of the segments. Examples of a cell before and after the unraveling process (window size 5), together with the corresponding histograms of soma-terminal distances, are presented in fig. 14.

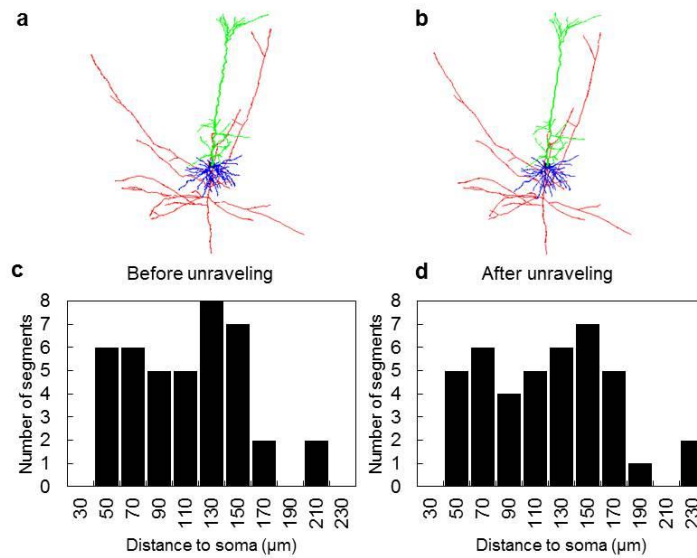


Figure 14 A L2/3 pyramidal neuron (a) before and (b) after unraveling. As a result of the process, the Roll distances, i.e. the displacement from the segment terminal to the cell body, are shifted upwards, which can be contrasted using the histograms (c) before and (d) after the process.

### **5.2.2 Determination of orders of axon segments**

Arborization was removed by deleting high-order axonal collaterals but preserving low-order ones. The treatment produced 6 different groups of cells, differentiated by the maximum order of the remaining collaterals. The group with the maximum order, i.e. 5, had collaterals with orders no greater than 5; the group with the minimum order, i.e. 0, had just the axon shaft but no collaterals.

### **5.2.3 Manipulation of diameter and synapses**

In real life, stimulation is usually administered on human subjects, the neuron of which can be substantially greater in size compared with the ones recruited in the present test. Furthermore, one would expect synaptic boutons, e.g. widening of diameter, at the axon terminals. Since the model predicted a very large number of APs originating from axon terminals, new experiments were conducted, in which the influence of size was studied via increasing the diameters of all the segments by one and two folds; in another test, the axonal terminals were expanded by one fold to mimic the widening of diameters in synapses.

### **5.2.4 Statistical analysis**

Multi-way ANOVA with repeated measures was used to detect differences in measured thresholds. Sensitivities of threshold to TMS pulse waveform and morphological features were studied with multi-way ANOVA for within-subject analysis, and were quantified using pairwise t-test, variance modified with Bonferroni-Holm correction. All tests were performed with R 3.1.1.

## 5.3 Results

### 5.3.1 Thresholds of different configurations

The thresholds for the four configurations of TMS are illustrated in fig. 15. The trends in simulated thresholds closely approximated the MTs measured on human subjects (Kammer et al., 2001). Statistical analysis revealed significant effects of layer, waveform and orientation of the field ( $p < 0.001$ ). An interaction effect was also identified between the waveform and the orientation ( $p < 0.001$ ), which makes the higher thresholds associated with the A-P monophasic stimulus and the lower values with the same orientation but the alternative waveform intelligible.

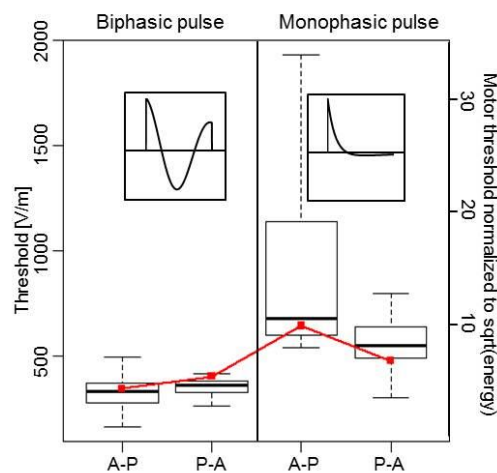


Figure 15 Box plot of thresholds to monophasic and biphasic TMS applied in two directions, overlaid on the MTs (of the Dantec stimulator) obtained in clinical studies (red) (Kammer et al. 2001). Note that the unit for MTs is the normalized square root of the stimulator output, which is “approximately proportional to the electric field induced”.

All of the activation points were located at the terminals of the axonal segments. For P-A direction monophasic pulse, the activation sites were almost the same with 0.1 ms rectangular pulse with two exceptions of relocation from the shafts to the collaterals. The activation sites of A-P biphasic stimulation were also similar, but 3 more initiation sites were shifted

to axon collaterals, which seemed to be excited by the first phase of the pulse. For the other two configurations, A-P monophasic stimuli almost always excited PCs via axon collaterals (37/40), whereas the effect of P-A biphasic pulse was less uniform, with almost half of the neurons activated from the axon collaterals (22/40).

### 5.3.2 Distinction among PCs

Fig. 16 plots the activation rate of two categories of PCs with respect to field intensities. Both curves have a linearly increasing trend, yet the L5 PCs have a lower starting point, which implies that they could respond to electric fields of weak intensities. L2/3 PCs on the other hand had higher thresholds and were unlikely to have any activity changes when the intensity was low. The distinction between PCs reflected the observations made previously from rectangular pulses that the ones from L5 had lower thresholds due to their greater sizes. Nonetheless, it should be noted that the distinction was only marginal, and hence the stimulation intensity window in which a single category of neuron could be activated might be very narrow.

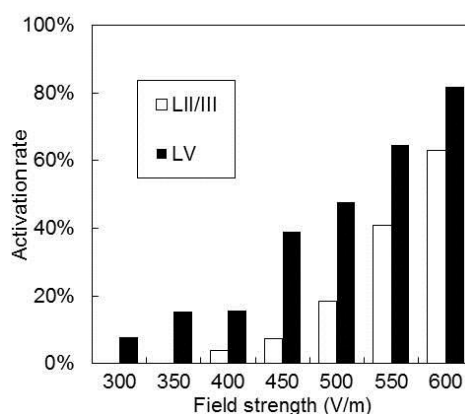


Figure 16 Activation rates of L2/3 & L5 PCs with respect to different field intensities. All values used are from A-P biphasic stimulation, i.e. the most efficient stimulation configuration.



### 5.3.3 Sensitivity of thresholds to arborization and tortuosity

The effect of the two morphological features is demonstrated in fig. 17.

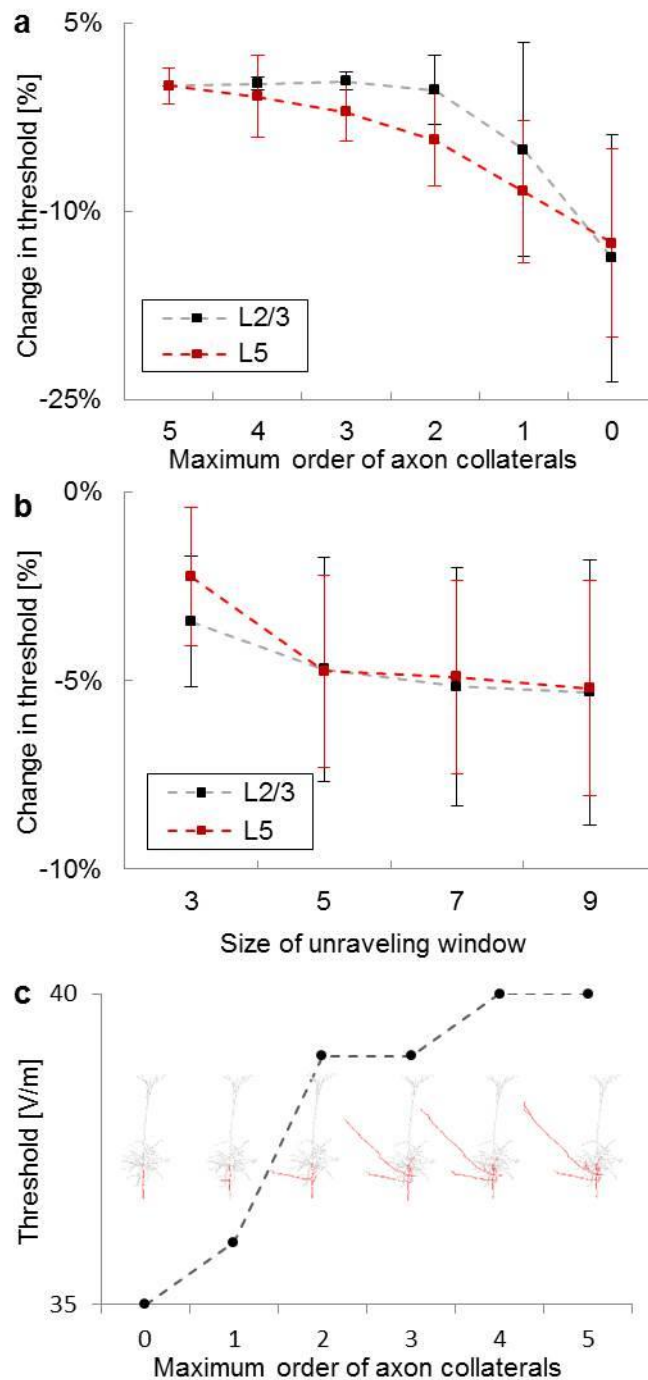


Figure 17 Sensitivity of thresholds to arborization (a) and tortuosity (b). Values are presented as percentage differences to neurons without manipulation on morphology. Measurements obtained from L2/3 PCs are labelled in grey; L5, red. The evolution of thresholds of a L2/3 PC with axon collaterals continually detached from the shaft is shown in (c). Note that the activation site is always located at the terminal of the axon shaft.

Detachment of order 1 collaterals, i.e. the ones directly connected to the shaft, was the most effective ( $p < 0.01$ ), which could cut the threshold by 3.9 V/m on average; manipulation of higher order collaterals had no significant effect. For some neurons, the decrement was due to the removal of the initiation segment. But as illustrated in fig. 17c, eliminating segments that were not directly activated could also have a substantial influence. Similarly, diminishing segment tortuosity could also decrease the threshold but with less efficacy. Although the effect was significant until window size reached seven, the reduction was merely 0.9 V/m per-expansion of the moving window.

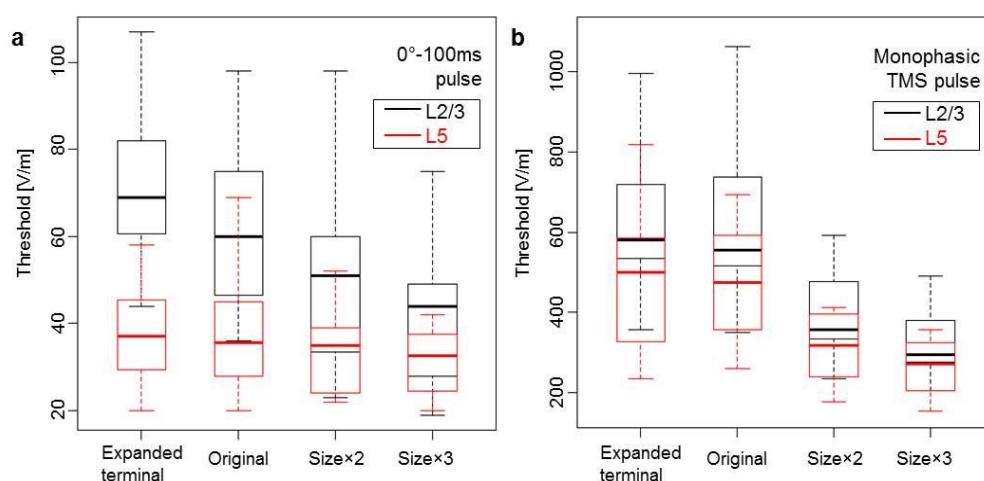


Figure 18 Sensitivity of thresholds to changes in cell diameters. (a) shows the thresholds of L2/3 & L5 PCs to 0°-100 ms stimulation. Three different types of manipulation were test: expanding all diameters to two folds; expanding all diameters to three folds; and expanding diameters of axonal terminals to two folds. (b) depicts the thresholds of the same cells to monophasic P-A TMS stimulus.

### 5.3.4 Influence of diameter and synapses

Fig. 18 shows the influence of cell diameter on the threshold values. In general, expanding the size of the cellular components could substantially reduce the numerical values of the thresholds ( $p < 0.01$ ), regardless of the pulse waveform applied. This was coherent with the inverse correlation between the diameter and the threshold revealed in previous study and could explain the

differences between layers, that larger L5 PCs have smaller thresholds. Furthermore, the finding could be used to make sense of the discrepancy between the MT and the simulated thresholds. Combining physiological recordings with computer simulation, the intensity of MT was estimated to be below 100 V/m (Thielscher et al., 2002), which was much lower than the thresholds documented in the present study. An explanation on the difference was that the PCs of human subjects were much larger than those of rats, and the distinctions in sizes were directly reflected on the thresholds.

#### **5.4 Discussion**

In this chapter, the author attempted to quantify the responses of cortical neurons towards various configurations of TMS. The results obtained were once again highly coherent with the findings from studies on patients, which might serve as the explanations to these phenomena. For instance, measurements of MTs have established that the biphasic stimulation has better efficiency among the two waveforms; monophasic stimulus has the highest efficacy when the field is in P-A direction (Mills et al., 1992) and the stimulus in this configuration preferentially activates neurons located in the sulcal wall of the motor cortex (Krieg et al., 2013). In our simulation, PCs always had lower thresholds to biphasic pulse. Besides, for monophasic pulse, the lower thresholds were observed when the field direction was from apical dendrites to axon, which is exactly the field-cell combination presented in the optimal stimulation setup.

In addition to the similarities in trends of thresholds and MTs, our simulation may be used to make sense of the observation that the sub-dural recording waveforms are associated with the field directions. It was noted in stimulation

trials that when monophasic stimulation is applied in P-A direction, I1-wave is always initiated at MT; A-P direction, I3-wave. On the other hand, A-P bipolar stimulation preferentially gives rise to I1-wave, whereas a diverse picture is presented with P-A bipolar pulse: some patients show I1-wave at MT while other produces I3-waves (Lazzaro et al., 2008).

Hypothesis of the working mechanism of TMS, arising from reviews of stimulation experiments and the canonical circuit of motor cortex, has attributed I1-wave to direct activation of L2/3 PC terminals (Di Lazzaro et al., 2012) and the subsequent interlayer transmission to PTNs embedded in the deeper layer. Correspondingly, when two configurations preferential to I1-wave were applied, the majority of the activation points were located at the terminals of the shafts, the most likely mediator of the interlayer excitatory transmission. The localization of the initiation point to the axon terminals could also explain the inertness of the MT to cortical activity: the excitability of the axonal components is not influenced by the MP at the soma or other segments hence the result of axonal excitation – the motor response – will have a highly stable threshold regardless of the synaptic transmissions in the cortex.

On the other hand, when A-P monophasic stimulation was applied, most of the initiation points were distributed at the terminals of axon peripherals, with many superficial to the soma. It is possible that during stimulation, these terminals are recruited for interlayer activation and the cells activated transmit excitatory input to the PTNs. As the transmission is bisynaptic, the relay is prolonged; the corresponding I-waves are delayed; the magnitudes of these I-waves are subject to the baseline activities of the relaying cells. Interestingly,

for the only configuration without a certain preference on the mechanism of activation, the compositions of the two categories of the activation points – the terminal of the shafts or the collaterals – were almost equivalent.

#### **5.4.1 LII/III pyramidal neurons**

As mentioned before, the activations of L2/3 pyramidal cells are believed to be responsible for the early I-wave. This hypothetical theory is somewhat contradictory to results obtained in our study. However, in spite of the lower activation rate of L2/3 PCs, their large population (Ren et al., 1992) and strong connectivity towards PTNs (Anderson et al., 2010) still mark them as highly probable drivers of the early I1-wave. Besides, a tremendous intra-group difference was observed among L2/3 cells that the highest threshold was almost two times the minimum. The difference indicates that the recruited excitatory input may be correlated to the field intensity in a large interval of stimulator output, which may account for the dose-dependency of the amplitude of I-waves (Di Lazzaro, 2004).

#### **5.4.2 LV pyramidal neurons**

Our simulation marks LV PCs as another potential target of TMS due to their low thresholds. Despite their high activation rates, whether L5 PCs are involved in shaping the evoked physiological responses remains arguable. It is generally agreed that the connectivity between L5 PCs and PTNs is low and the synaptic input is weak (Anderson et al., 2010; Neymotin et al., 2011; Thomson et al., 2002; Weiler et al., 2008). The sparse activation of LV pyramidal neurons caused by low intensity TMS may not be able to drive PTNs in the same layer to react to stimulation.

However, L5 PCs are still of key importance as they may be responsible for certain network-level effect. The interhemispheric inhibition discovered in motor cortex stimulation experiments provides early evidence that TMS can change activities of remote brain areas (Daskalakis et al., 2002; Ferbert et al., 1992). Experiments using repetitive TMS (rTMS) protocols further show that a large network of brain areas, including subcortical structures, can be modulated by stimulation of a single cortical area (Ding et al., 2014; Fox, Halko, et al., 2012; Strafella et al., 2001). And this modulation is vital for the therapeutic effect of rTMS (Fox, Liu, et al., 2012). Our simulation shows that the mediator of the projections to cortical and subcortical areas, i.e. L5 PCs, can be directly activated by TMS as their thresholds are usually lower than the output of the stimulator. Additionally, a substantial amount of the L5 PCs has thresholds lower than the minimum threshold of L2/3 PCs. They are enabled by the low thresholds to be recruited by pulses with intensities lower than MT, which may explain the modulation effect evoked by subthreshold rTMS (Bestmann et al., 2003; Siebner et al., 2003).

#### **5.4.3 Influence of cell morphology**

In the previous chapter, it was demonstrated that the activation of neurons by EM stimulation could be regarded as the manifestation of the competition between various firing-capable segments. In this chapter, with the analysis of the impact of the morphological features on stimulation susceptibility, it is further revealed that these potential initiation locations are not independent of each other. First of all, back-propagation was rarely hindered in the simulation, which implies that the synapses with minimum threshold, which might be responsible for the initial motor responses, could be from the same cell.

Secondly, the sensitivity analysis for bifurcation reveals that, segments that are not directly activated can act as current sinks to shunt the induced axial current. The ramifications of PCs are tremendous and variant; as a result, the mean and the variance of thresholds are both elevated.

To give a more straightforward demonstration of the competition and interference between the various activation-capable components, the thresholds of three simplified neurons – the first with a straight axon, the second with a branched axon, and the third with a 30° bent axon – were tested (fig. 19). When 0° stimulation was applied, the cell with the straight axon has a terminal aligned with the field, hence its threshold was the lowest, and the initiation point is located at the terminal of the shaft; if 30° stimulation was used, the terminal of the bent axon would be parallel to the field and its threshold was the minimum, and the initiation point is still the same. For the cell with the bifurcated axon, the initiation point was determined by the field orientation, however, whenever a terminal was in line with the field, the other branch would act as a current sink, and its thresholds were always larger than the other two cells, regardless of the field direction.

It is worth noting that the thresholds assessed with enlarged cells may not be representative of the susceptibilities of the real neurons that are larger in diameters. It was observed that an increase in the cell diameters by two folds could reduce the firing patterns of PCs under minimum current injection to singlet spiking. In other words, for the expanded cell to retain its firing pattern, the membrane conductances are expect to change, which renders the values used in simulation invalid.

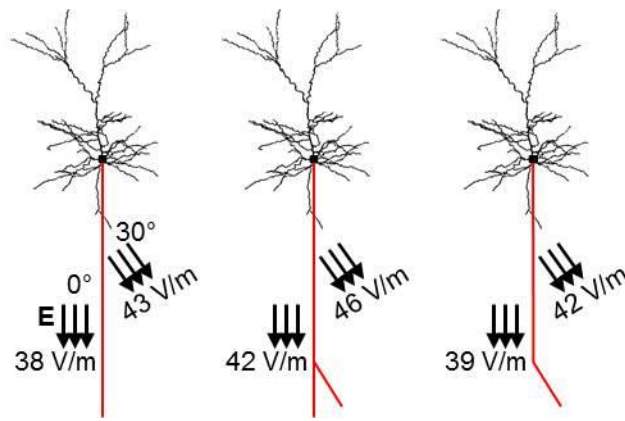


Figure 19 Thresholds of cells with a straight axon, a branched axon and a 30° bent axon to 0° & 30° 100ms stimulation. The dendritic components of the three cells are the same.

### 5.5 Concluding remarks

The simulation model is validated using MT values obtained in clinical tests.

Based on this model, a quantitative analysis of cortical neuron activation probability towards TMS has been conducted. The conclusions are as follows:

1. TMS-evoked activations are initiated at the terminals of the axons, the localization of which is correlated with the shape of the I-waves;
  2. L2/3 PCs can be activated by low intensity pulse hence might be responsible for TMS-evoked motor responses;
  3. L5 PCs may also be activated by TMS to give rise to network-level responses.
- Tests performed on neurons with manipulated morphologies further indicate that the various activation-capable neuronal components are not independent and that cell size is inversely correlated to thresholds.



## **Chapter 6 Responses of inhibitory neurons to EM stimulation**

Inhibitory neurons play pivotal roles in the modulation of cortical activities. Their suppressive output to excitatory cells, when transmitted timely, serve to reduce background noise, contrast informatic input, balance the susceptibility of the network, thus enables the signal processing. In neuromodulation, inhibitory neurons are no less important than their counterparts – the PCs – in shaping the stimulation effects. In spite of the recognition of their importance, the cellular responses of inhibitory cells have rarely been addressed in simulation studies.

In this section, the author aims to use computer simulation to study the interaction between the stimulation induced electric field and the inhibitory neurons. Unfortunately, the current understanding of inhibitory neuron is deficient – so far, high-fidelity models of any types of the inhibitory cells are still lacking. Hence, in place of a comprehensive study to which such models are indispensable, the measurement of cellular responses was conducted on a single cell with its membrane properties determined from a search algorithm.

### **6.1 Nest basket cell morphology**

Manual inspection was conducted on all the inhibitory neurons in the aforementioned cortical neuron database. Among all the inhibitory cells, a nested basket cell (NBC) (fig. 20) was selected for its relatively intact morphology in 3D space; the ion channels specific to the neuronal components were inserted; the maximum conductance values of all the channels were then obtained with a genetic search algorithm.

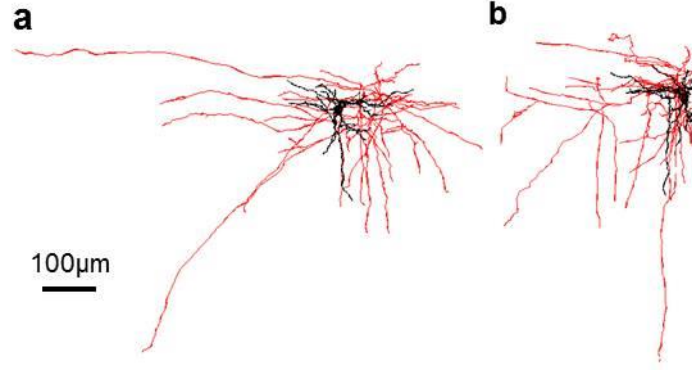


Figure 20 The morphology of the tested nest basket cell in (a) front view and (b) side view. Axonal components are plotted in red; the dendritic and somatic ones are colored in black. The neuron has 51 basal dendrites (average diameter 1.0  $\mu\text{m}$ , length 36.42  $\mu\text{m}$ ) and 127 axonal segments (average diameter 0.3  $\mu\text{m}$ , length 61.22  $\mu\text{m}$ ).

## 6.2 Determination of axonal membrane properties

### 6.2.1 Membrane properties and ion channels

The author set the axial resistance and the membrane capacitance of the whole cell to  $100 \Omega \cdot \text{cm}$  &  $1 \mu\text{F}/\text{cm}^2$  respectively. The dendritic membrane of the cell was set to be passive ( $PAS = 10^{-6} \text{ S}/\text{cm}^2$ ). For the cell body, a total of 10 types of ion channels were attached, all of which followed the HH style as described in equation (10), (11) & (12):

1, fast inactivating sodium channel  $Na_t$  (Hamill et al., 1991);

$$\alpha_m = \frac{0.182 \cdot (V_m + 38)}{1 - e^{\frac{-(V_m+38)}{6}}} \beta_m = \frac{-0.124 \cdot (V_m + 38)}{1 - e^{\frac{-(V_m+38)}{6}}}$$

$$\alpha_h = \frac{-0.015 \cdot (V_m + 66)}{1 - e^{\frac{-(V_m+66)}{6}}} \beta_h = \frac{0.015 \cdot (V_m + 66)}{1 - e^{\frac{-(V_m+66)}{6}}}$$

$$m_\infty = \frac{\alpha_m}{\alpha_m + \beta_m} h_\infty = \frac{\alpha_h}{\alpha_h + \beta_h}$$

$$\tau_m = \frac{1}{T_{adj}(\alpha_m + \beta_m)} \tau_h = \frac{1}{T_{adj}(\alpha_h + \beta_h)}$$

$$N_m = 3 \quad N_h = 1$$

2, persistent sodium channel  $Na_p$  (Magistretti et al., 1999);

$$\alpha_m = \frac{0.182 \cdot (V_m + 38)}{1 - e^{\frac{-(V_m+38)}{6}}} \quad \beta_m = \frac{-0.124 \cdot (V_m + 38)}{1 - e^{\frac{-(V_m+38)}{6}}}$$

$$\alpha_h = \frac{-2.88 \cdot 10^{-6} \cdot (V_m + 17)}{1 - e^{\frac{-(V_m+17)}{4.63}}} \quad \beta_h = \frac{6.94 \cdot 10^{-6} \cdot (V_m + 64.4)}{1 - e^{\frac{-(V_m+64.4)}{2.63}}}$$

$$m_\infty = \frac{1}{1 + e^{\frac{-(V_m+52.6)}{4.6}}} \quad h_\infty = \frac{1}{1 + e^{\frac{V_m+48.8}{10}}}$$

$$\tau_m = \frac{6}{T_{adj}(\alpha_m + \beta_m)} \quad \tau_h = \frac{1}{T_{adj}(\alpha_h + \beta_h)}$$

$$N_m = 3 \quad N_h = 1$$

3, fast inactivating potassium channel  $K_{fast}$  (Korngreen et al., 2000);

$$m_\infty = \frac{1}{1 + e^{\frac{-(V_m+10)}{19}}} \quad h_\infty = \frac{1}{1 + e^{\frac{(V_m+76)}{10}}}$$

$$\tau_m = \frac{0.34 + 0.92e^{-\left(\frac{V_m+81}{59}\right)^2}}{T_{adj}} \quad \tau_h = \frac{8 + 49e^{-\left(\frac{V_m+83}{23}\right)^2}}{T_{adj}}$$

$$N_m = 4 \quad N_h = 1$$

4, slow inactivating potassium channel  $K_{slow}$ ;

$$m_\infty = \frac{1}{1 + e^{\frac{-(V_m+11)}{12}}} \quad h_\infty = \frac{1}{1 + e^{\frac{(V_m+64)}{11}}}$$

$$\tau_m = \frac{1.25 + 175.03e^{0.025(V_m+10)}}{T_{adj}}, \quad V < -60$$

$$\tau_m = \frac{1.25 + 13e^{-0.026(V_m+10)}}{T_{adj}}, \quad V \geq -60$$

$$\tau_h = \frac{360 + (1010 + 24(V_m + 65))e^{-\left(\frac{V_m+85}{48}\right)^2}}{T_{adj}}$$

$$N_m = 2 \quad N_h = 1$$

5, fast non-inactivating  $K_v$  3.1 channel  $Kv_{3.1}$  (Rudy et al., 2001);

$$m_\infty = \frac{1}{1 + e^{\frac{-(V_m-18.7)}{9.7}}} \quad \tau_m = \frac{4}{T_{adj}(1 + e^{\frac{-(V_m+56.56)}{44.14}})}$$

$$N_m = 1$$

6, muscarinic potassium channel  $I_M$  (Bibbig et al., 2001);

$$\alpha_m = 0.0033e^{0.1(V_m+35)} \quad \beta_m = 0.0033e^{-0.1(V_m+35)}$$

$$m_\infty = \frac{\alpha_m}{\alpha_m + \beta_m} \quad \tau_m = \frac{1}{T_{adj}(\alpha_m + \beta_m)}$$

$$N_m = 1$$

7, calcium dependent small-conductance potassium channel  $SK$  (Kohler et al., 1996);

$$m_\infty = \frac{1}{1 + \left(\frac{0.00043}{[Ca^{2+}]_i}\right)^{4.8}}$$

$$\tau_m = 1, N_m = 1$$

8, A-type potassium channel  $I_A$  (Klee et al., 1995);

$$\zeta_m = -1.5 - \frac{1}{1 + \frac{\exp(V_m + 40)}{5}}$$

$$\alpha_m = e^{96.48 \cdot \zeta_m \cdot \frac{(V_m - 11)}{8.315(273.16 + T)}} \quad \beta_m = e^{53.4064 \cdot \zeta_m \cdot \frac{(V_m - 11)}{8.315(273.16 + T)}}$$

$$m_\infty = \frac{1}{\alpha_m + 1} \quad \tau_m = \frac{\beta_m}{0.05 T_{adj} (\alpha_m + 1)}$$

$$\alpha_h = e^{96.48 \cdot \frac{3(V_m + 56)}{8.315(273.16 + T)}}$$

$$h_\infty = \frac{1}{\alpha_h + 1} \quad \tau_h = 0.26(V_m + 50)$$

$$N_m = 1 \quad N_h = 1$$

9, hyperpolarization-activated cation current  $I_h$  (Kole et al., 2006);

$$\alpha_m = \frac{0.00643 \cdot (V_m + 154.9)}{e^{\frac{(V_m + 154.9)}{11.9}} - 1} \quad \beta_m = 0.00193 e^{\frac{V_m}{33.1}}$$

$$m_\infty = \frac{\alpha_m}{\alpha_m + \beta_m} \quad \tau_m = \frac{1}{\alpha_m + \beta_m}$$

$$N_m = 1$$

10, high-voltage-activated calcium channel  $Ca$  (Reuveni et al., 1993).

$$\alpha_m = -\frac{0.055(V_m + 27)}{e^{\frac{-(V_m + 27)}{3.8}} - 1} \quad \beta_m = 0.94 e^{\frac{V_m + 75}{17}}$$

$$m_\infty = \frac{\alpha_m}{\alpha_m + \beta_m} \quad \tau_m = \frac{1}{\alpha_m + \beta_m}$$

$$\alpha_h = 0.000457 e^{\frac{-(V_m + 13)}{50}} \quad \beta_h = \frac{0.0065}{e^{\frac{-(V_m + 15)}{28}} + 1}$$

$$N_m = 2 \quad N_h = 1$$

The decay of intracellular calcium concentration and  $T_{adj}$  were the same as in section 3.4. For axonal components, the A-type potassium, M-type potassium, high-voltage-activated calcium and calcium dependent small-conductance potassium channels were excluded as they were identified in previous studies to be absent in axon (Lai et al., 2006; Vacher et al., 2008). The maximum conductance values of the channels, as well as the passive conductance of the soma and axon membrane, were left undetermined, hence in total 18 variables were searched via optimization.

### **6.2.2 Search algorithm**

The genetic algorithms have been proved by existing studies (Druckmann et al., 2007; Hay et al., 2011) to be an effective method for constraining conductance-based compartmental models. Compared with other methods, the approach explores many solutions simultaneously, which could be used for statistical analysis of the influence of various channels on stimulation susceptibility. In light of this special merit of the approach, the author implemented a variant of the algorithm – the non-dominated sorting genetic algorithm (NSGA) (Srinivas et al., 1994) – on the NEURON platform for the optimization.

### **6.2.3 Initialization of the population**

At the beginning of the implementation, a group (7500) of individuals was initialized, each containing 18 randomly generated variables. The values of each variable followed a uniform distribution after logarithm transformation. The lower limits of all variables were  $1 \times 10^{-6} S/cm^2$ . The upper bounds

were  $1 \times 10^{-2} S/cm^2$  for membrane passive conductance,  $1 \times 10^{-1} S/cm^2$  for persistent sodium, high-voltage-activated calcium, calcium dependent small-conductance potassium, hyperpolarization-activated cation channels, and  $1 S/cm^2$  for all other channels. The conductance values contained in each individual were then applied on the cell and the MP dynamics in response to a 225 pA current injection to soma were subsequently collected. After the collection of MP was finished on all the individuals, 150 individuals that could give rise to at least 3 APs were selected as the initial population of the iteration and the fitness of each solution was evaluated.

#### **6.2.4 Feature based error functions**

The fitness metrics used in the study were features of the spiking response. The error functions employed could, therefore, be termed feature-based error functions. The error value was calculated as follows: for a given stimulus (e.g., depolarizing current step) the values of each feature – mean and standard deviation – were extracted from a previous experiment. Given the simulated MP to that same stimulus, the values of the features were extracted as in the experimental trace. Then the differences between the mean values of the experimental responses and the data from the model response were measured in units of the experimental standard deviation.

The error functions the author chose for the present study consisted six features extracted from the MP of the NBC soma in response: (1) spike rate; (2) accommodation index; (3) delay of the first spike; (4) average AP overshoot; (5) average depth of AHP; (6) half AP duration. Spike rate was calculated by dividing the number of spikes in the trace by the duration of the step current (0.5 sec). The accommodation index was defined by

$$A = \frac{1}{N-1} \sum_{i=2}^N \frac{(isi_i - isi_{i-1})}{(isi_i + isi_{i-1})} \quad (21)$$

where  $N$  is the number of spikes,  $isi$  denotes inter-spike interval and  $i$  is the index of the spike; latency to first spike is the time between stimulus onset and the beginning of the first spike (defined as the maximum of the second derivative of MP); average AP overshoot was calculated by averaging the absolute peak MP values of all APs. Average AHP depth was the mean of the minimum of the MP between two consecutive APs. Half AP duration was calculated by averaging the width of every AP at the midpoint between its onset and its peak. Values measured *in vitro* for NBCs were: spike rate  $36.1 \pm 9.97$  Hz; accommodation index  $0.0045 \pm 0.0023$ ; first spike delay  $12.3 \pm 3.17$  ms; AP overshoot  $13.6 \pm 3.48$  mV; AHP depth  $-51.4 \pm 2.15$  mV; half AP duration  $1.02 \pm 0.44$  ms (Druckmann et al., 2007).

In addition to the soma MPs, features of axon firings, characterized by the failure rate of transmission ( $0.74 \pm 1.43\%$ ) and the average transmission delay ( $0.91 \pm 0.24$  ms) were supplemented (Wang et al., 2002). Furthermore, as the NBCs typically host no intrinsic spiking, another feature – the AP firing rate at the absence of current injection – was adopted, with the mean and standard deviation arbitrarily set to  $0 \pm 1$  Hz.

### 6.2.5 Domination rank

The common method to establish a fitness evaluation function is to assign weights to and sum up all the feature-based errors. The implementation of the single fitness value was nevertheless discovered to be inappropriate for the present problem, because the practice could easily lead to early convergence to local minimums. To solve the problem, the author adopted another strategy



that allowed several potentially conflicting error functions to be used jointly (K. Deb et al., 2002).

The approach assessed the fitness of an individual via domination relations, which was determined with the following criteria that if both were fulfilled individual 1 was said to dominate individual 2:

$$f_j(x^1) \leq f_j(x^2) \text{ for all } j = 1 \dots n$$

$$f_k(x^1) \leq f_k(x^2) \text{ for at least one } k \in [1, n]$$

The domination rank among the whole population was given by the following procedures:

1. for each individual p in main population P
  - Initialize  $S_p = \emptyset$  ;. This set would contain all the individuals that is being dominated by p.s
  - Initialize  $n_p = 0$ . This would be the number of individuals that dominate p.
  - For each individual in q in P, if p dominates q, add q to the set  $S_p$ , otherwise  $n_p$  is increased by 1.
  - If  $n_p = 0$ , i.e. no individual dominates p then p belongs to the first front. Set rank of individual p to one, update the first front set by adding p to front one  $F_1 = F_1 \cup p$ .
2. This is carried out for all the individuals in the population P.
3. Initialize the front counter to one.  $i = 1$ .
4. Following is carried out while the  $i^{\text{th}}$  front is not empty
  - $Q = \emptyset$ . The set for storing the individuals in the  $(i+1)^{\text{th}}$  front.
  - For each individual in p in front  $F_i$

\* for each individual  $q$  in  $S_p$ ,  $n_q = n_q - 1$ .

\* If  $n_q = 0$ , then none of the solutions in the subsequent fronts would dominate  $q$ , hence set  $q_{rank} = i + 1$ , update  $Q$  with  $Q = Q \cup q$

--Increment the front counter by 1.

--Now the set  $Q$  is the next front and hence  $F_{i+1} = Q$

After the domination ranks of all the individual solutions were determined, a hybridization pool was then extracted from the original population following the tournament selection scheme, in which two individuals were randomly selected and the one with the lower rank would be retained. If the two individuals had the same rank, the selection would be random. The selection process was repeated until the number of individuals in the pool reached half of the initial population size. The breeding of the new individuals was then carried out.

### 6.2.6 Breeding of new individuals

The “breeding” procedure used in the algorithm comprised two different modes of changing the parameters, namely crossover and mutation. The probabilities of the two scenarios to take places were 90% and 10% respectively. The crossover scheme implemented was named simulated binary crossover (SBX) (Kalyanmoy Deb et al., 1995) and aimed at replicating the effect of the standard crossover operation in a binary genetic algorithm. Thus, an offspring would have different parameter values taken from each of the two parents and some might be slightly modified. The mathematical equation of this process is given by

$$C_{1,k} = 0.5[(1 - \beta_k)p_{1,k} + (1 + \beta_k)p_{2,k}] \quad (22)$$

$$C_{2,k} = 0.5[(1 + \beta_k)p_{1,k} + (1 - \beta_k)p_{2,k}] \quad (23)$$

where  $C_{i,k}$  is the  $i^{\text{th}}$  offspring's  $k^{\text{th}}$  variable,  $p_{i,k}$  is the selected parent and  $\beta_k$  is a value sampled from a random number with the density

$$p(\beta) = 0.5(\eta_c + 1)\beta^{\eta_c}, \text{ if } 0 \leq \beta \leq 1 \quad (24)$$

$$p(\beta) = 0.5(\eta_c + 1)\frac{1}{\beta^{\eta_c+2}}, \text{ if } \beta > 1. \quad (25)$$

This distribution was obtained from a uniformly sampled random number  $u$  between (0, 1).  $\eta_c$  is the distribution index specified by the user and was set to 5 in the present study.

$$\beta(u) = (2u)^{\frac{1}{(\eta_c+1)}}, \text{ if } 0 < u \leq 0.5 \quad (26)$$

$$\beta(u) = \frac{1}{[2(1-u)]^{\frac{1}{(\eta_c+1)}}}, \text{ if } 0.5 \leq u < 1. \quad (27)$$

The mutation scheme was named polynomial mutation,

$$c_k = p_k + (p_k^u - p_k^l)\delta_k \quad (28)$$

where  $c_k$  is the child and  $p_k$  is the parent with  $p_k^u$  being the upper bound on the parent component,  $p_k^l$  is the lower bound and  $\delta_k$  is a small variation which was calculated from a polynomial distribution by using

$$\delta_k = (2r_k)^{\frac{1}{(\eta_m+1)}} - 1, \text{ if } 0 < r_k \leq 0.5 \quad (29)$$

$$\delta_k = 1 - \frac{1}{[2(1-r_k)]^{\frac{1}{(\eta_m+1)}}}, \text{ if } 0.5 \leq r_k < 1 \quad (30)$$

$r_k$  is a uniformly sampled random number between (0, 1) and  $\eta_m$  is the mutation index specified by the user, which was set to 5 in the present project.

The “children” of the breeding process were once again assessed for error values and then combined with the existing population. Local search algorithm was then applied on the combined population to accelerate the converging process, which is naturally slow in genetic algorithms.

### 6.2.7 Local search algorithm

The local search algorithm adopted was named random derivative method, comprising the following steps:

1. A variable was randomly selected as the search direction; the population standard deviation  $\sigma_p^k$  of the variable was obtained.

2. A random number was sampled from a normal distribution, and added to the original value.

$$C'_k = C_k + r_k, r_k \sim N(0, \sigma_p^k) \quad (31)$$

3. The solution was applied on the NBC and the sum of the feature-based errors was calculated.

4. If the sum was lower than the sum of the old feature-based errors, the errors were updated; otherwise, the new variable was given by

$$C'_k = C_k - r_k \quad (32)$$

5. The sum of the new feature-based errors was calculated. If the value became lower, errors were updated; otherwise the search was discarded.

The local search was conducted on 10% of the individuals randomly selected from the population for five iterations. For 75% of the individuals undergoing local searches, the variables were updated together with the error values to

imitate Lamarckian evolution. The variables of the remaining 25% were not altered in the searching process, mimicking the Baldwinian evolution.

The above processes – evaluation of domination rank, selection of breeding pool, hybridization, local searching – were repeated until the termination criteria (all feature errors  $< 2$  or the best solution with the minimum sum of error stopped evolving for 10 iterations) were met or the maximum iteration number (1000) was reached.

### **6.3 Measurement of thresholds**

The solutions from the last 5 evolution iterations that had sum of feature errors  $< 15$  were applied on the NBC; measurements of their thresholds towards monophasic TMS were conducted in P-A and A-P directions. Furthermore, the thresholds towards paired stimuli were also documented in the P-A direction – two pulses were applied with the interval of 1 ms, with the strength of the first stimulus being 80% of the second one as in SICI. The threshold value was marked by the intensity of the second stimulus. In the end, the two individuals with the highest fitness were identified and their thresholds in 12 directions, as mentioned in chapter 3, were obtained.

### **6.4 Statistical analysis**

Pearson's product-moment correlation values between thresholds and ion channel conductances/spiking features were examined. One-way ANOVA was used to pinpoint the difference between the thresholds of the NBC and the L2/3 & L5 PCs. Post hoc analysis was conducted with Tukey's HSD method to quantify the significant effects ( $p < 0.05$ ).

## 6.5 Results

### 6.5.1 Reduction of feature errors by the search algorithm

Fig. 21a depicts the sum of feature errors in 250 iterations of the NSGA. The value was averaged across the 10 fittest solutions in each generation. Instead of a monotonically decreasing trend, several local maximums could be detected: the peak of error took place at the 9th iteration; several spikes were located around the 50th iteration. Since these local elevations were not presented in the previous studies in which local search was not employed, it appeared that they resulted from the local search algorithm – the random derivative method. A possible explanation to these spikes was that they represented the exploitation by the local search – when a new possible solution was generated by the genetic algorithm, the local search method would update the solution towards its local minimum. If any one of the features of the updated solution had the error value lower than the population, it would have a low domination rank, regardless of the other feature errors, and hence would have a higher chance of getting included in the breeding pool. The inclusion of these solutions would increase the population error sum for the particular iteration, but would also accelerate the exploration process and in turn the convergence of the optimization.

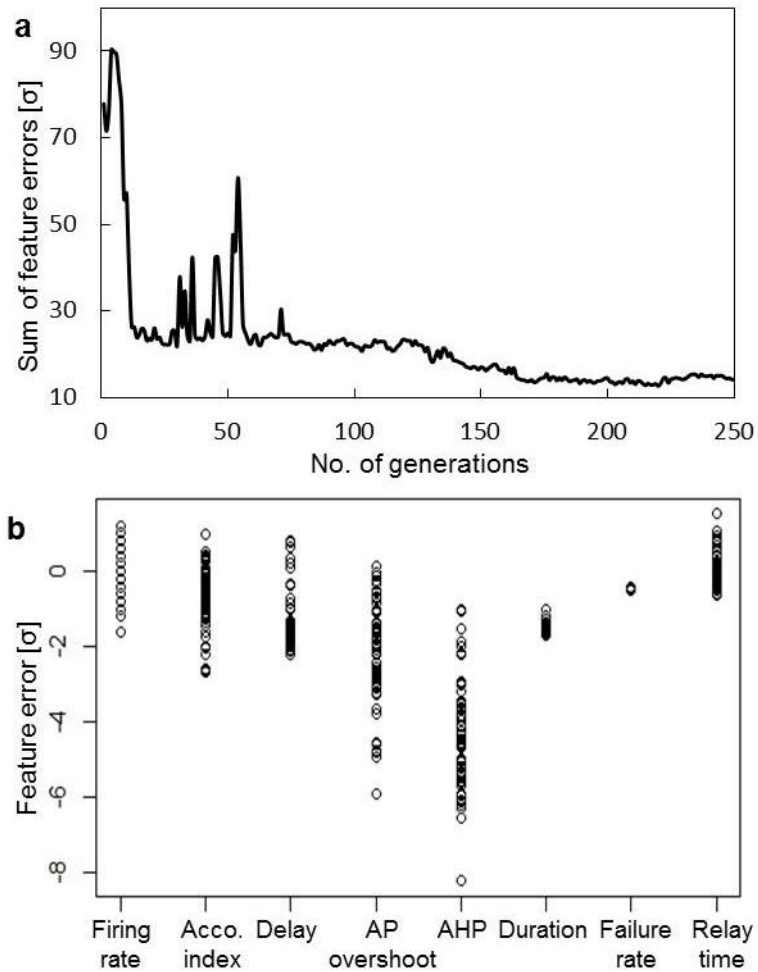


Figure 21 Sum of feature errors vs generation. (a) The error sums of the 10 fittest solutions within each generation are averaged and plotted against the number of iterations. (b) Distribution of the feature errors after the searching. Note that the error of last feature, the number of APs at the absence of current injection, is omitted as the value is always zero for all selected solutions.

As a matter of fact, the error value converged to the final solution within 200 iterations, a number much smaller than what has been documented in previous studies. The spiking features of the fittest solutions ( $n = 128$ ) from the last five iterations are plotted in fig. 21b. For the majority of the features, the identified solutions had error values well restrained under two standard deviations. The only exceptions were the AP overshoot and the AHP – none of the solutions had both error values controlled below two standard deviations simultaneously. Nevertheless, it was noted that these features were very sensitive to the size of the soma. It is possible that the discrepancies resulted from the different sizes

of the NBCs studied in the present study and in the *in vitro* experiment. In fact, in the study from which the morphology of the NBC was extracted, the overshoot and the AHP of spontaneous APs were recorded and the standard deviations were much greater – 15.3 mV and 5.3 mV respectively.

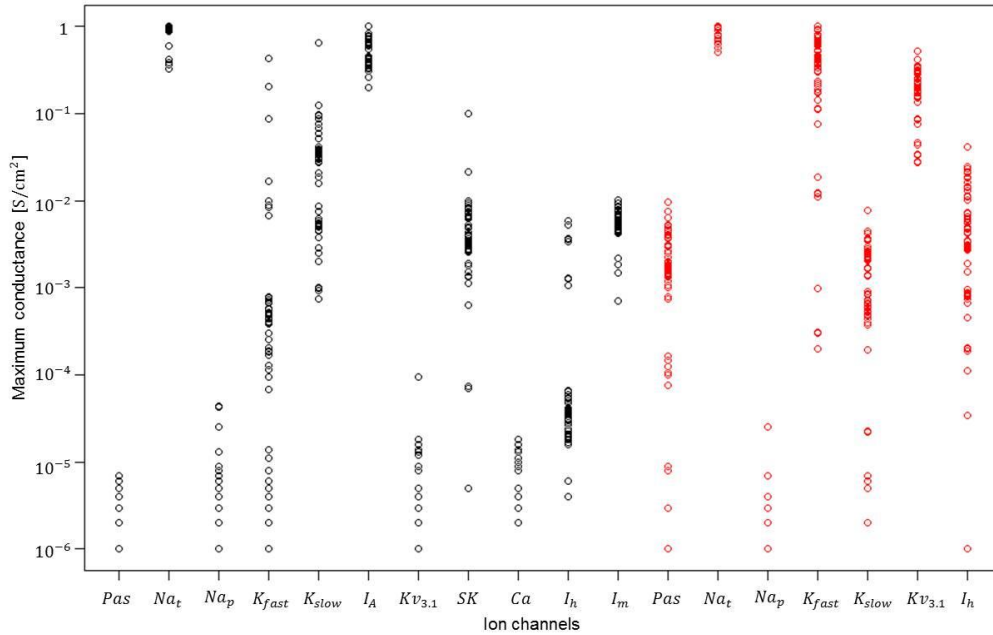


Figure 22 Distribution of ion channel maximum conductance values. The ion channels attached to the axonal components are colored in red, whereas the ones attached to the cell body are in black.

### 6.5.2 Membrane properties of inhibitory neurons

Fig. 22 shows the distributions of the maximum conductance values of all the ion channels attached to the NBC. A number of channels, including the fast & slow inactivating potassium channels in the cell body and the hyperpolarization-activated cation channel at the axon, had highly divergent distributions. On the contrary, the driving force of APs – the fast inactivating sodium channel, was highly uniform among solutions and was almost identical in soma and in axon. Interestingly, with this only exception, the compositions of membrane conductance at the two cellular components were quite distinct. In soma, the rectifying potassium current was mainly contributed by the A-



type potassium channel; the other channels played a rather insignificant role. In axon, the repolarization current was mediated by the fast inactivating and the fast non-inactivating potassium channel. The passive membrane conductance was also quite different: the value was close to zero in soma, but was substantial in axon. The varied constitution of the membrane conductance might be indicative of the distinct roles of the neuronal components: for the soma, generation of APs; for the axon, faithful transmission of APs.

### 6.5.3 Thresholds of the NBC

The average threshold of the acceptable solutions, when applied on the NBC, was  $3109.77 \pm 396.19$  V/m in P-A direction and  $4211.15 \pm 330.83$  V/m in A-P direction. Both values were tested to be significantly higher than that of PCs ( $p < 0.001$ ). For both stimulation directions, two activation initiation sites were presented – for P-A direction, 30 solutions shared an initiation site distinct from the others, whereas the number for A-P direction was only 2. Moreover, the failure rate of back-propagation reached 50% in P-A direction, although the transmission was never hindered in the opposite direction. The application of paired stimuli following the SICI protocol failed to reduce the stimulation thresholds. As a matter of fact, the thresholds were slightly elevated ( $3232.34 \pm 405.00$  V/m).

### 6.5.4 Correlation between threshold and ion channel conductances

Correlation analysis of the thresholds revealed several ion channels that could significantly influence the stimulation susceptibility of the cell: soma  $Na_p$  (0.29,  $p < 0.001$ ); soma  $Na_t$  (-0.24,  $p < 0.01$ ); soma  $K_{fast}$  (-0.36,  $p < 0.001$ ); soma  $K_{slow}$  (-0.20,  $p < 0.5$ ); soma  $I_A$  (-0.22,  $p < 0.05$ ); soma  $SK$  (-0.33,  $p < 0.001$ ); soma  $Ca$  (-0.41,  $p < 0.001$ ); soma  $I_m$  (0.32,  $p < 0.05$ ); axon  $Pas$

(0.92,  $p < 0.001$ ); axon  $Na_p$  (-0.23,  $p < 0.01$ ); axon  $K_{fast}$  (0.57,  $p < 0.001$ ); axon  $K_{slow}$  (0.47,  $p < 0.001$ ); axon  $Kv_{3.1}$  (0.31,  $p < 0.001$ ); axon  $I_h$  (0.2,  $p < 0.05$ ).

### 6.5.5 Correlation between threshold and spiking features

The correlations between the threshold and the spiking features are plotted in fig. 23. Most of the features, especially those regarding the waveforms of the APs, were highly inter-correlated: the highest correlations were between AP overshoot, delay of first AP and AHP; the accommodation index was correlated to all the values examined. On the other hand, only three features had significant impact on the thresholds, and two of them were concerned with the transmission properties of the axon.

### 6.5.6 Threshold anisotropy

Fig. 24a plots the MPs of the two solutions in response to current injection. The first solution (red) has the following conductance values: for soma  $Pas$   $10^{-6} S/cm^2$ ,  $Na_t$   $1 S/cm^2$ ,  $Na_p$   $4.4 \times 10^{-5} S/cm^2$ ,  $K_{fast}$   $8.8 \times 10^{-3} S/cm^2$ ,  $K_{slow}$   $9.8 \times 10^{-2} S/cm^2$ ,  $I_A$   $1 S/cm^2$ ,  $Kv_{3.1}$   $2.0 \times 10^{-6} S/cm^2$ ,  $SK$ :  $7.5 \times 10^{-5} S/cm^2$ ,  $I_h$   $5 \times 10^{-6} S/cm^2$ ,  $Ca$   $1.26 \times 10^{-3} S/cm^2$ ,  $I_m$   $1.49 \times 10^{-3} S/cm^2$ ; for axon soma  $Pas$   $10^{-6} S/cm^2$ ,  $Na_t$   $9.13 \times 10^{-1} S/cm^2$ ,  $Na_p$   $2 \times 10^{-6} S/cm^2$ ,  $K_{fast}$   $2.99 \times 10^{-4} S/cm^2$ ,  $K_{slow}$   $2.2 \times 10^{-5} S/cm^2$ ,  $Kv_{3.1}$   $7.5 \times 10^{-2} S/cm^2$ ,  $I_h$   $10^{-6} S/cm^2$ . The second solution (blue): soma  $Pas$   $4 \times 10^{-6} S/cm^2$ ,  $Na_t$   $1 S/cm^2$ ,  $Na_p$   $6 \times 10^{-6} S/cm^2$ ,  $K_{fast}$   $5.14 \times 10^{-4} S/cm^2$ ,  $K_{slow}$   $5.83 \times 10^{-3} S/cm^2$ ,  $I_A$   $6.23 \times 10^{-1} S/cm^2$ ,  $Kv_{3.1}$   $10^{-6} S/cm^2$ ,  $SK$ :  $7.32 \times 10^{-3} S/cm^2$ ,  $I_h$   $9 \times 10^{-6} S/cm^2$ ,  $Ca$   $2.4 \times 10^{-5} S/cm^2$ ,  $I_m$   $6.51 \times 10^{-3} S/cm^2$ ; for axon

soma  $Pas$   $1.79 \times 10^{-3} S/cm^2$ ,  $Na_t$   $7.88 \times 10^{-1} S/cm^2$ ,  $Na_p$   $4 \times 10^{-6} S/cm^2$ ,  $K_{fast}$   $6.30 \times 10^{-1} S/cm^2$ ,  $K_{slow}$   $5.34 \times 10^{-4} S/cm^2$ ,  $Kv_{3,1}$   $2.91 \times 10^{-1} S/cm^2$ ,  $I_h$   $6.18 \times 10^{-3} S/cm^2$ . The first solution has the following spiking features: firing rate 36Hz, accommodation index 0.0016, delay of first AP 14.73 ms, AP overshoot 2.31 mV, AHP -57.83 mV, AP half duration 0.28 ms, failure rate of transmission 0.03%, average relay time 0.79 ms; the second solution: firing rate 36Hz, accommodation index 0.0043, delay of first AP 6.93 ms, AP overshoot 9.78 mV, AHP -63.64 mV, AP half duration 0.37 ms, failure rate of transmission 0%, average relay time 0.93 ms.

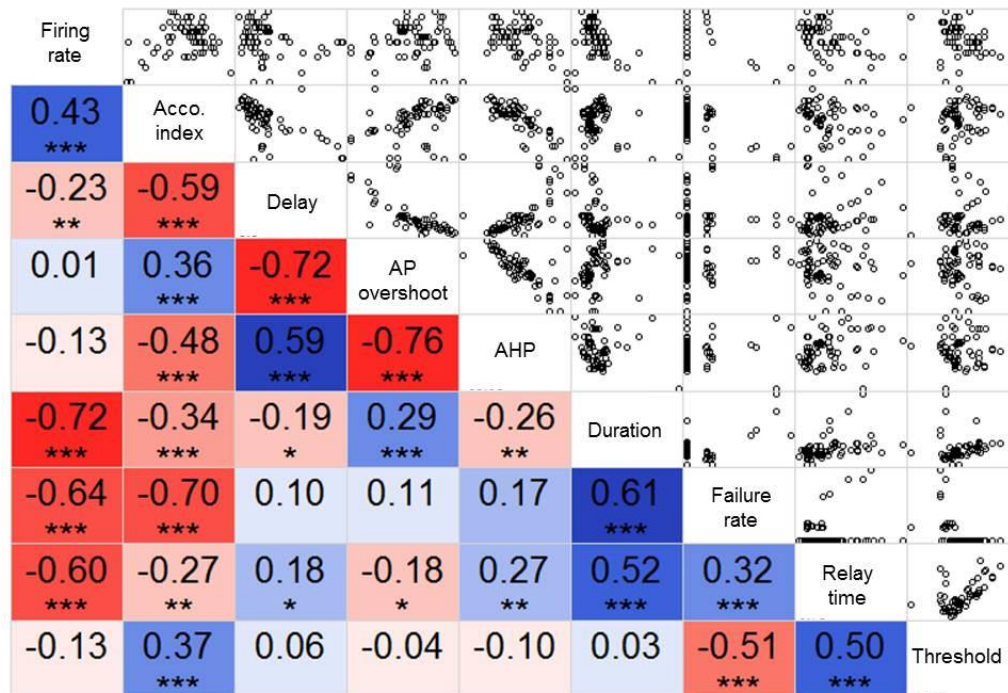


Figure 23 Correlation map of the spiking features and the stimulation thresholds. The upper panels show the scatter plots of different pairs of parameters; the lower panels exhibit the corresponding correlation values, \*:  $p < 0.05$ , \*\*:  $p < 0.01$ , \*\*\*:  $p < 0.001$ .

The thresholds of both solutions (fig. 24b) had the identical trend across all the tested field directions – the peaks were located at  $-150^\circ$  while the minimums were from  $-30$  degree. Although the difference of thresholds between the

solutions varied with the field direction, the absence of any interception seemed to hint that the threshold anisotropy of a single cell is associated with the morphology although the numerical value is under the influence of membrane conductance.

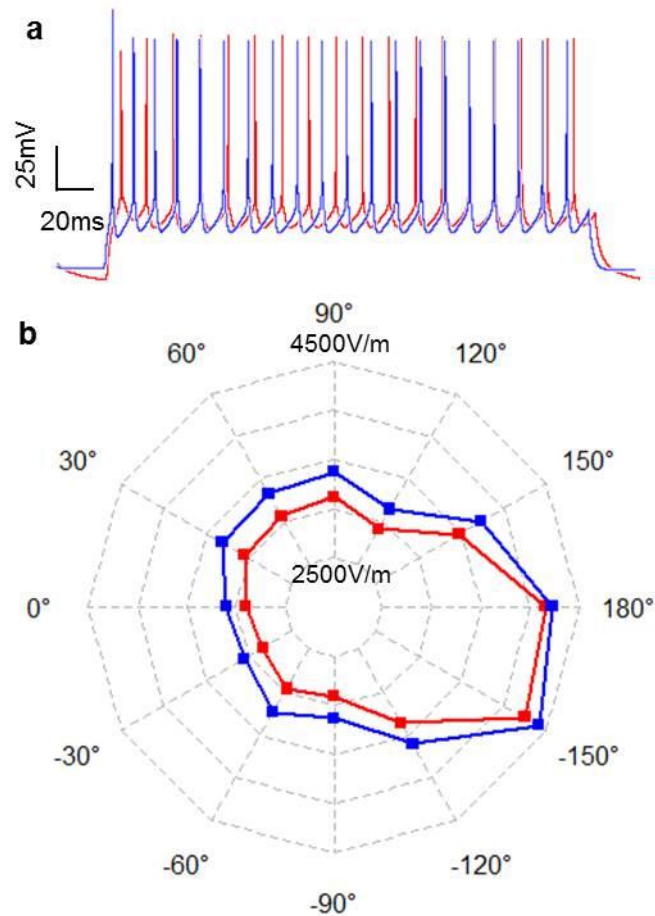


Figure 24 MPs and thresholds of two fittest solutions. (a) MPs of the NBC in response to current injection. (b) The thresholds of the two solutions towards 12 different field directions. As the NBC lacks a clear axon shaft, the 0° is labeled as the opposite of the y axis of the coordinate system in which the morphology was reconstructed.

## **6.6 Discussion**

### **6.6.1 Validity of the optimization approach**

Compared with most of the optimization problems, the searching for the membrane conductance values of a specific cell according to its electrophysiological recordings is unique in many different aspects. To begin with, the fact that the goal of the optimization is a time series signal determines that an error function based solely on either time domain or frequency domain information cannot provide a descriptive assessment of the fitness. Customized metrics which conjugate the time as well as the waveform of the AP are required. Secondly, the initiation process, i.e. sampling parameters from a random variable, can generate lots of invalid solutions in which the calculation of feature-based errors cannot be conducted. For instance, More than three-fourths of the randomly generated individuals would render the cell unable to fire action potential. The calculation of all the error values in this case is of course not applicable. Last but not least, the non-linearity of the search space is much enhanced by the dynamics of and the interplays between the channel-constituting molecules. In fact, it was discovered during the simulation process that a slight alternation of the conductance of a single channel can in many cases totally transform the resultant APs.

To deal with these problem-specific characters, a multitude of additional steps were introduced to the NSGA optimization paradigm. The feature-based error values captured the timing, the waveform and the transmission of APs, and hence providing an assessment scheme of the fitness of individual solutions with improved comprehensiveness. The author also made use of a pre-filtering

process, which ensured that all the individuals in the initial population were valid solutions that could be assessed. This step enabled the search to be performed with a relatively small population hence reduces the computation expense. The employment of local searching following the evolution iterations accelerated the slow converging process characteristic to genetic algorithm.

The validity of this hybrid optimization approach is consolidated by the fact that many of the findings established in biological studies are echoed. For most of the acceptable solutions, a common character, namely a large  $K_{v3.1}$  conductance in axon (Gupta et al., 2000; Markram et al., 2004), can almost always be spotted. The channel is characterized by its fast activation and non-inactivation behavior during APs and can function as reliable rectifier of MP when the neuron is undergoing high frequency firing. As a matter of fact, this channel has been identified as a signature molecule for fast spiking inhibitory cells. The presence of the channel in most of the fit solutions further confirms the validity of the optimization approach in extracting the membrane conductance values with only electrophysiological recordings.

### **6.6.2 Influence of membrane properties and ion channels on thresholds**

The thresholds assessed from the two solutions suggest that the anisotropy is decided by the morphology of the cell. Nevertheless, the unexpected correlation between the threshold and the channels attached to the soma implies that the channel properties distant from the initiation site could also impact the thresholds. Together, these findings reaffirm the aforementioned conclusion that the threshold is influenced by not only the geometry of the initiation site but also the whole electrotonic structure of the neuron.

On the other hand, the high correlation between the threshold and the axon *Pas*, together with its substantial conductance, identifies the very parameter to be the major determinant of the stimulation susceptibility of the cell; the other channels attached to the axon, especially those mediating potassium currents, are also positively correlated to threshold. It seemed that, for neurons that undergo fast spiking, it is crucial for the axon to be able to rectify the depolarization currents and ready the cell for subsequent firings. This character is realized through either high passive membrane conductance or opening of non-activating potassium channels. These properties of the axon would however reduce the susceptibility of the cell and subsequently increase the stimulation thresholds. As a result, the thresholds of the NBC with the fittest solutions to TMS pulses were much higher than that of the PCs.

Interestingly, the spectrum of ion channels in the axon of PTN might be deemed as the mixture of the PCs and the fast spiking inhibitory cells: on the one hand, the passive membrane resistivity is high due to the existence of the myelin sheath; on the other hand, the  $K_v3.1$  channel is attached to enable the cell to have high firing frequency (Ichinohe et al., 2004). According to the correlation values, this unique character of the PTNs would place their thresholds higher than PCs but lower than inhibitory cells, which perfectly explains the high stimulation threshold of the D-wave.

### **6.6.3 Thresholds to paired stimulation**

The slight elevation of the thresholds introduced by paired stimulation stands in contradiction to the previous hypothesis that the SICI effect is realized through accumulation of depolarization effects of the two stimuli in the axon of the inhibitory cells. In fact, the low membrane resistivity of the NBC axon

would reduce the time constant of the neuronal component and predispose the cell to be immune to any of the summation effects. Should there be any cumulative effects of the two pulses, the myelinated axonal compartments of the PCs, which have high membrane conductance and resistance and subsequently time constants, would be the more probable targets. However, as the MTs in SICI experiments are not affected, it might be concluded that the “summation” effect does not take place at the cellular level.

### **6.7 Concluding remarks**

The genetic algorithm successfully optimized the membrane properties and ion channel conductances, which empowered the NBC to have spiking features resembling experimental recordings. The thresholds obtained from the fittest solutions show that, although the anisotropy is largely determined by the cell morphology, the numerical value of the threshold is dependent on the distributions of the ion channels, not only in the axon where the activation is initiated but also in the cell body. The fast-spiking firing pattern of the NBC necessitates high passive conductance and permeability of potassium ion in the axon, which would result in high threshold and render the cell unlikely to respond to stimulation. Application of paired stimuli failed to reduce the stimulation thresholds; the SICI effect is not likely to be realized on the cellular level.



## **CHAPTER 7 Conclusion and recommendation for future work**

### **7.1 Comparison with existing models**

The model described in the present study is distinct from the aforementioned ones in many aspects and a detailed comparison is provided in table. 5. Briefly, the existing models that have placed emphasis on the fidelity of the cell morphology and membrane properties were highly specific – usually one type of cell and its response to a single type of stimulation was examined. Constrained by the implementation strategies, they lacked the extendibility to be applied on a variety of cells for group-level studies. On the other hand, the attempt to include multiple types of cells was based on highly arbitrary cells models, the responses of which are very likely to have significant deviations from the real cells. Moreover, the potential inaccuracies of the model introduced by the simplifications of the adopted cells have not been systematically evaluated; and no substantiation or validation process was employed.

Undertaking the challenge to combine the two approaches, the present model incorporated the procedures for registration of morphological components, quantification of ion channels, and determination of compartment numbers. The resulting model could be applied robustly on a multitude of neurons without compromising the completeness of the cell morphologies or the membrane properties. The simulated results were highly consistent with the measurements obtained from *in vivo* and *in vitro* experiments.

Table 5. Comparison of the present model and the existing ones.

	Present model	Kamitani et al	Pashut et al	McIntyre et al	Salvadore et al
Boundary condition	Sealed	Sealed	Open	N.A.	Sealed
Bifurcation point	Treated	Treated	Untreated	N.A.	No bifurcation
Membrane current	Distributed	Current source	Distributed	Distributed	Distributed
Discretization according to morphology	Yes	No	No	No	No
Morphology	Realistic	Partially realistic	Partially realistic	Partially realistic	Arbitrary
Membrane model	Multiple PCs and inhibitory cells	Specific PC	Specific PC	Specific PC	Simplified
Number of cells tested	Multiple	1	1	1	Multiple
Number of types of cells tested	PC + inhibitory cell	PC	PC	PC	PC + inhibitory
Simulated modality	TMS, tDCS	TMS	circular TMS	DBS	TMS
Stimulation configuration	Multiple	Singular	Singular	Singular	Multiple

## **7.2 Contributions**

Empowered by the unique features, the model may contribute to the neuromodulation research community by producing quantitatively accurate assessment of cellular responses to stimulation. The findings obtained with the model have the potential to clarify some of the long lasting controversies over the stimulation mechanism, e.g. activation point, inter-layer difference, susceptibility of inhibitory cell, etc. The influence of various stimulation factors, such as field direction, pulse waveform, morphological features, and ion channel distributions, may also be explored and consolidated with the model.

## **7.3 Limitations**

In the present study, the author has excluded inputs from intracortical synaptic transmission and intercortical afferent projection during simulation. Results obtained only reflect the responses of quiescent neurons, which could potentially deviate from neurons *in vivo*. However it has been demonstrated that the threshold to trigger I1-wave is largely unaffected by synaptic activities (Lazzaro et al., 2008), and activation of afferent input tends to evoke long latency I-waves (Shimazu et al., 2004), hence our results may still be applicable to analysis of direct cellular responses towards EM stimulation.

A potential source of error roots from the physiological properties utilized in the study. Although the adopted model enables PCs to have distinct firings patterns, the assumption that the distribution of ion channels and membrane properties are always the same is unlikely to hold true. Key membrane

parameters can be different, for cells from the same layer (Molnár et al., 2006), and even for different parts of axon of a single cell (Debanne et al., 2011). The ion channels inserted to the inhibitory channels included nearly all the channels that have been identified in cortical neurons. However, certain highly detailed features were not enclosed in the cell model, such as the fast activating dynamics of the sodium channels at the initial segment of the axon, the localization of calcium channels at the axon terminals, and the differentiation between the subtypes of ion channels. Whether exclusion of these details entails the remaining feature-based errors after the optimization requires further examination.

The direct mediator of TMS- & TES- evoked descending volleys, the PTNs, are not simulated in our study. PTNs have distinct morphologies, membrane dynamics and firing patterns compared with other pyramidal neurons (Chen et al., 1996; Ghosh et al., 1988; Oswald et al., 2013; Suter et al., 2013), which could potentially lead to very different thresholds. As the D-wave can be recruited by high intensity TMS pulses, the thresholds of PTNs might be higher than those of most pyramidal neurons. However, the lack of PTNs has constrained us from providing quantitative measurement of the threshold of the D-wave.

Last but not least, all cortical neurons tested in this study are obtained from rats while TMS induced physiological responses are usually measured from human subjects. Although the author has attempted to eliminate the influence of cell size via manipulation of segment diameters, the discrepancy induced by other factors, such as the distinct ramification, tortuosity, and distribution of ion channels, would remain intractable.

## 7.4 Conclusions

To give a comprehensive investigation of the stimulation-evoked neuronal activation, the author developed a simulation scheme which incorporates highly detailed physiological and morphological properties of pyramidal cells. The model was implemented on a sample of PCs; their thresholds and corresponding activation points with respect to various field directions and pulse waveforms were recorded.

The measurements obtained in simulation intimately resemble recordings in physiological and clinical studies, which confirms the validity of the simulation model. The analysis of initiation points of AP reveals that the cellular excitability might represent the result of the competition between various firing-capable axonal components, each with a unique susceptibility determined by the local geometry. In light of this competition scheme, the L5 PCs have higher susceptibility than L2 PCs due to their larger sizes; the anisotropy of thresholds is marginal as each neuron hosts many axon terminals oriented in various directions; activation at a bending point is difficult to take place since the polarization hosted by the geometry is weak.

The model was further deployed on an inhibitory cell, the membrane properties of which were obtained from an optimization algorithm. The thresholds of the acceptable solutions hint that the high passive conductance and the substantial permeability to potassium ion in the axon – the prerequisite of the fast-spiking pattern – compel the cell to have lower susceptibility than PCs. The inertness of the threshold to paired stimuli further indicates that the SICI effect is unlikely to be realized on the cellular level.

## 7.5 Recommendation for future works

Although rats and humans all belong to the *mammalia* class, it can be expected from their distinct behavioral patterns and brain structures that the physiological features of their cortical neurons are quite different. To what extent could the findings in the present study be applied on human subjects is questionable. The decision to use pyramidal cells harvested from rat somatosensory cortex in the present study originally stems from the scarcity of human data, for when the project started, neither the morphology nor the membrane ion channel distributions is available due to ethical concerns. However, with the new development in mapping neuron morphology and ion channel distributions, extraction of the human neuron model without sacrificing test subjects no longer seemed to be a mission impossible. Should the relevant human data crucial for simulation be made available, the model may be modified to assess the excitability of human neurons.

Due to the limited simulation resources and information on the biological formation of inhibitory neurons, only one of the basket cells was studied in this project. Taking the response of this particular neuron as a representative of the general behavior of inhibitory neurons could be problematic, considering the multiple subtypes of inhibitory neurons and the various firing patterns presented within each subtype. The current approach, in which only the cell morphology together with the corresponding firing features are required to search for the optimal conductance values has the theoretical extendibility to other subtypes, yet the extremely slow searching procedure has severely hindered its adaptability. If the searching process could be refined, batch

extraction of inhibitory neurons' physiological models as well as statistical analysis of their responses to stimulation might become feasible.

Last but not least, the neuronal responses documented in the present study has the potential to be used for interpretation and elucidation of more extensive experimental results, however, without being incorporated into a network context, the explanatory power is still fractioned. By faithfully connecting the neurons with appropriate connectivities and realistic stimulation-evoked activities, a network model might be established in the future to elucidate the working mechanism of EM stimulation.

## References

- Anderson, Charles T., Sheets, Patrick L., Kiritani, Taro, & Shepherd, Gordon M. G. (2010). Sublayer-specific microcircuits of corticospinal and corticostriatal neurons in motor cortex. *Nat Neurosci*, *13*(6), 739-744.
- Anwar, Haroon, Riachi, Imad, Hill, Sean, Schurmann, Felix, & Markram, Henry. (2009). An Approach to Capturing Neuron Morphological Diversity *Computational Modeling Methods for Neuroscientists*: The MIT Press.
- Ardesch, J. J., Buschman, H. P., Wagener-Schimmel, L. J., van der Aa, H. E., & Hageman, G. (2007). Vagus nerve stimulation for medically refractory epilepsy: a long-term follow-up study. *Seizure*, *16*(7), 579-585.
- Arlotti, M., Rahman, A., Minhas, P., & Bikson, M. (2012). Axon terminal polarization induced by weak uniform DC electric fields: a modeling study. *Conf Proc IEEE Eng Med Biol Soc*, *2012*, 4575-4578.
- Ascoli, G. A., Donohue, D. E., & Halavi, M. (2007). NeuroMorpho.Org: a central resource for neuronal morphologies. *J Neurosci*, *27*(35), 9247-9251.
- Baek, K., Chae, J. H., & Jeong, J. (2012). The effect of repetitive transcranial magnetic stimulation on fear extinction in rats. *Neuroscience*, *200*, 159-165.
- Balslev, Daniela, Braet, Wouter, McAllister, Craig, & Miall, R. Chris. (2007). Inter-individual variability in optimal current direction for transcranial magnetic stimulation of the motor cortex. *Journal of Neuroscience Methods*, *162*(1-2), 309-313.
- Barker, A. T., Jalinous, R., & Freeston, I. L. (1985). Non-invasive magnetic stimulation of human motor cortex. *The Lancet*, *325*(8437), 1106-1107.



- Barr, M. S., Farzan, F., Wing, V. C., George, T. P., Fitzgerald, P. B., & Daskalakis, Z. J. (2011). Repetitive transcranial magnetic stimulation and drug addiction. *Int Rev Psychiatry*, 23(5), 454-466.
- Bersani, F. S., Minichino, A., Enticott, P. G., Mazzarini, L., Khan, N., Antonacci, G., . . . Biondi, M. (2012). Deep transcranial magnetic stimulation as a treatment for psychiatric disorders: A comprehensive review. *Eur Psychiatry*.
- Bestmann, S., Baudewig, J., Siebner, H. R., Rothwell, J. C., & Frahm, J. (2003). Subthreshold high-frequency TMS of human primary motor cortex modulates interconnected frontal motor areas as detected by interleaved fMRI-TMS. *Neuroimage*, 20(3), 1685-1696.
- Bibbig, A., Faulkner, H. J., Whittington, M. A., & Traub, R. D. (2001). Self-organized synaptic plasticity contributes to the shaping of gamma and beta oscillations in vitro. *J Neurosci*, 21(22), 9053-9067.
- Brunelin, J., Mondino, M., Haesebaet, F., Saoud, M., Suaud-Chagny, M. F., & Poulet, E. (2012). Efficacy and safety of bifocal tDCS as an interventional treatment for refractory schizophrenia. *Brain Stimul*, 5(3), 431-432.
- Cartee, L.A., & Plonsey, R. (1992). The Transient Subthreshold Response of Spherical and Cylindrical Cell Models to Extracellular Stimulation. *IEEE Trans Biomed Eng*, 39(1), 76-85.
- Chanpattana, W., Chakrabhand, M. L., Buppanharun, W., & Sackeim, H. A. (2000). Effects of stimulus intensity on the efficacy of bilateral ECT in schizophrenia: a preliminary study. *Biol Psychiatry*, 48(3), 222-228.
- Chen, W., Zhang, J. J., Hu, G. Y., & Wu, C. P. (1996). Electrophysiological and morphological properties of pyramidal and nonpyramidal neurons in the cat motor cortex in vitro. *Neuroscience*, 73(1), 39-55.

- Cheung, S. W., & Larson, P. S. (2010). Tinnitus modulation by deep brain stimulation in locus of caudate neurons (area LC). *Neuroscience*, *169*(4), 1768-1778.
- Cincotta, M., Borgheresi, A., Gambetti, C., Balestrieri, F., Rossi, L., Zaccara, G., . . . Cantello, R. (2003). Suprathreshold 0.3 Hz repetitive TMS prolongs the cortical silent period: potential implications for therapeutic trials in epilepsy. *Clin Neurophysiol*, *114*(10), 1827-1833.
- Crank, John, & Nicolson, Phyllis. (1947). A practical method for numerical evaluation of solutions of partial differential equations of the heat-conduction type. *Proc Camb Philos Soc*, *43*, 50-67.
- Cutsuridis, V., Cobb, S., & Graham, B. P. (2010). Encoding and retrieval in a model of the hippocampal CA1 microcircuit. *Hippocampus*, *20*(3), 423-446.
- Daskalakis, Zafiris J, Christensen, Bruce K, Fitzgerald, Paul B, Roshan, Lailoma, & Chen, Robert. (2002). The mechanisms of interhemispheric inhibition in the human motor cortex. *J Physiol*, *543*(1), 317-326.
- Davison, A. P., & Fregnac, Y. (2006). Learning cross-modal spatial transformations through spike timing-dependent plasticity. *J Neurosci*, *26*(21), 5604-5615.
- Deb, K., Pratap, A., Agarwal, S., & Meyarivan, T. (2002). A fast and elitist multiobjective genetic algorithm: NSGA-II. *Evolutionary Computation, IEEE Transactions on*, *6*(2), 182-197.
- Deb, Kalyanmoy, Agrawal, Ram Bhusan, & Agrawal, Ram Bhushan. (1995). *Simulated Binary Crossover for Continuous Search Space*.
- Debanne, D., Campanac, E., Bialowas, A., Carrier, E., & Alcaraz, G. (2011). Axon physiology. *Physiol Rev*, *91*(2), 555-602.

- DeGiorgio, C. M., Shewmon, A., Murray, D., & Whitehurst, T. (2006). Pilot study of trigeminal nerve stimulation (TNS) for epilepsy: a proof-of-concept trial. *Epilepsia*, *47*(7), 1213-1215.
- Di Lazzaro, V. (2004). The physiological basis of transcranial motor cortex stimulation in conscious humans. *Clin Neurophysiol*, *115*(2), 255-266.
- Di Lazzaro, V., Profice, P., Ranieri, F., Capone, F., Dileone, M., Oliviero, A., & Pilato, F. (2012). I-wave origin and modulation. *Brain Stimul*, *5*(4), 512-525.
- Ding, L., Shou, G., Yuan, H., Urbano, D., & Cha, Y. H. (2014). Lasting Modulation Effects of rTMS on Neural Activity and Connectivity as Revealed by Resting-State EEG. *IEEE Trans Biomed Eng*, *61*(7), 2070-2080.
- Druckmann, Shaul, Banitt, Yoav, Gidon, Albert, Schürmann, Felix, Markram, Henry, & Segev, Idan. (2007). A Novel Multiple Objective Optimization Framework for Constraining Conductance-Based Neuron Models by Experimental Data. *Frontiers in Neuroscience*, *1*(1), 7-18.
- Dudley, W. H. C., & Williams, J. G. (1972). Electroconvulsive Therapy in Delirium Tremens. *Comprehensive Psychiatry*, *13*(4), 357-&.
- Esser, Steve K. Hill Sean L. Tononi Giulio. (2005). Modeling the Effects of Transcranial Magnetic Stimulation on Cortical Circuits. *Journal of Neurophysiology*, *94*(1), 622-639.
- Faria, P., Fregni, F., Sebastiao, F., Dias, A. I., & Leal, A. (2012). Feasibility of focal transcranial DC polarization with simultaneous EEG recording: preliminary assessment in healthy subjects and human epilepsy. *Epilepsy Behav*, *25*(3), 417-425.
- Ferbert, A., Priori, A., Rothwell, J. C., Day, B. L., Colebatch, J. G., & Marsden, C. D. (1992). Interhemispheric inhibition of the human motor cortex. *J Physiol*, *453*, 525-546.

Fox, M. D., Halko, M. A., Eldaief, M. C., & Pascual-Leone, A. (2012). Measuring and manipulating brain connectivity with resting state functional connectivity magnetic resonance imaging (fcMRI) and transcranial magnetic stimulation (TMS). *Neuroimage*, *62*(4), 2232-2243.

Fox, M. D., Liu, H., & Pascual-Leone, A. (2012). Identification of reproducible individualized targets for treatment of depression with TMS based on intrinsic connectivity. *Neuroimage*, *66C*, 151-160.

George, M. S., Padberg, F., Schlaepfer, T. E., O'Reardon, J. P., Fitzgerald, P. B., Nahas, Z. H., & Marcolin, M. A. (2009). Controversy: Repetitive transcranial magnetic stimulation or transcranial direct current stimulation shows efficacy in treating psychiatric diseases (depression, mania, schizophrenia, obsessive-compulsive disorder, panic, posttraumatic stress disorder). *Brain Stimul*, *2*(1), 14-21.

George, M. S., Ward, H. E., Jr., Ninan, P. T., Pollack, M., Nahas, Z., Anderson, B., . . . Ballenger, J. C. (2008). A pilot study of vagus nerve stimulation (VNS) for treatment-resistant anxiety disorders. *Brain Stimul*, *1*(2), 112-121.

Ghosh, S., & Porter, R. (1988). Morphology of pyramidal neurones in monkey motor cortex and the synaptic actions of their intracortical axon collaterals. *J Physiol*, *400*, 593-615.

Gilbert, D. L., Sallee, F. R., Zhang, J., Lipps, T. D., & Wassermann, E. M. (2005). Transcranial magnetic stimulation-evoked cortical inhibition: a consistent marker of attention-deficit/hyperactivity disorder scores in tourette syndrome. *Biol Psychiatry*, *57*(12), 1597-1600.

Goldman, R. L., Borckardt, J. J., Frohman, H. A., O'Neil, P. M., Madan, A., Campbell, L. K., . . . George, M. S. (2011). Prefrontal cortex transcranial

direct current stimulation (tDCS) temporarily reduces food cravings and increases the self-reported ability to resist food in adults with frequent food craving. *Appetite*, 56(3), 741-746.

Grant, Peadar F., & Lowery, Madeleine M. (2010). Effect of Dispersive Conductivity and Permittivity in Volume Conductor Models of Deep Brain Stimulation. *IEEE Trans Biomed Eng*, 57(10), 2386-2393.

Grill, W. M., Cantrell, M. B., & Robertson, M. S. (2008). Antidromic propagation of action potentials in branched axons: implications for the mechanisms of action of deep brain stimulation. *J Comput Neurosci*, 24(1), 81-93.

Groiss, Stefan J., Netz, Johannes, Lange, Herwig W., & Buetefisch, Cathrin M. (2012). Frequency dependent effects of rTMS on motor and cognitive functions in Huntington's disease. *Basal Ganglia*, 2(1), 41-48.

Gubellini, P., Salin, P., Kerkerian-Le Goff, L., & Baunez, C. (2009). Deep brain stimulation in neurological diseases and experimental models: from molecule to complex behavior. *Prog Neurobiol*, 89(1), 79-123.

Gupta, Anirudh, Wang, Yun, & Markram, Henry. (2000). Organizing Principles for a Diversity of GABAergic Interneurons and Synapses in the Neocortex. *Science*, 287(5451), 273-278.

Haeusler, S., & Maass, W. (2007). A statistical analysis of information-processing properties of lamina-specific cortical microcircuit models. *Cereb Cortex*, 17(1), 149-162.

Hamill, O. P., Huguenard, J. R., & Prince, D. A. (1991). Patch-clamp studies of voltage-gated currents in identified neurons of the rat cerebral cortex. *Cereb Cortex*, 1(1), 48-61.

- Hay, E., Hill, S., Schurmann, F., Markram, H., & Segev, I. (2011). Models of neocortical layer 5b pyramidal cells capturing a wide range of dendritic and perisomatic active properties. *PLoS Comput Biol*, 7(7), e1002107.
- Hines, M.L., & Carnevale, N.T. (2001). NEURON: a Tool for Neuroscientists. *Neuroscientist*, 7, 123-135.
- Hodgkin, A.L., & Huxley, A.F. (1952). A Quantitative Description of Membrane Currents and Its Application to Conduction and Excitation in Nerve. *J Physiol*, 117, 500-544.
- Hord, E. D., Evans, M. S., Mueed, S., Adamolekun, B., & Naritoku, D. K. (2003). The effect of vagus nerve stimulation on migraines. *J Pain*, 4(9), 530-534.
- Horiuchi, M., Maki, F., Yanagisawa, T., Sugihara, H., Takahashi, Y., Ohashi, K., . . . Nakajima, Y. . (2002). Therapeutic efficacy of transcranial magnetic stimulation for amyotrophic lateral sclerosis and spinocerebellar degeneration. *International Congress Series*, 1235, 525-532.
- Ichinohe, N., Watakabe, A., Miyashita, T., Yamamori, T., Hashikawa, T., & Rockland, K. S. (2004). A voltage-gated potassium channel, Kv3.1b, is expressed by a subpopulation of large pyramidal neurons in layer 5 of the macaque monkey cortex. *Neuroscience*, 129(1), 179-185.
- Jalinous, R. (1991). Technical and practical aspects of magnetic nerve stimulation. *J Clin Neurophysiol*, 8(1), 10-25.
- Kamitani, Y., Bhalodia, V. M., Kubota, Y., & Shimojo, S. (2001). A model of magnetic stimulation of neocortical neurons. *Neurocomputing*, 38-40, 697-703.
- Kammer, T., Beck, S., Thielscher, A., Laubis-Herrmann, U., & Topka, H. (2001). Motor thresholds in humans: a transcranial magnetic stimulation study

comparing different pulse waveforms, current directions and stimulator types. *Clin Neurophysiol*, 112(2), 250-258.

Kandel, E., & Schwartz, J. (2013). *Principles of Neural Science, Fifth Edition*: McGraw-Hill Education.

Kandel, M., Beis, J. M., Le Chapelain, L., Guesdon, H., & Paysant, J. (2012). Non-invasive cerebral stimulation for the upper limb rehabilitation after stroke: A review. *Ann Phys Rehabil Med*, 55(9-10), 657-680.

Karmacharya, R., England, M. L., & Ongur, D. (2008). Delirious mania: clinical features and treatment response. *J Affect Disord*, 109(3), 312-316.

Kerr, C.C., Neymotin, S.A., Chadderdon, G.L., Fietkiewicz, C.T., Francis, J.T., & Lytton, W. (2012). Electrostimulation as a Prosthesis for Repair of Information Flow in a Computer Model of Neocortex. *IEEE Transactions on Neural Systems and Rehabilitation*, 20(2), 153-160.

Klee, R., Ficker, E., & Heinemann, U. (1995). Comparison of voltage-dependent potassium currents in rat pyramidal neurons acutely isolated from hippocampal regions CA1 and CA3. *J Neurophysiol*, 74(5), 1982-1995.

Kohler, M., Hirschberg, B., Bond, C. T., Kinzie, J. M., Marrion, N. V., Maylie, J., & Adelman, J. P. (1996). Small-conductance, calcium-activated potassium channels from mammalian brain. *Science*, 273(5282), 1709-1714.

Kole, M. H., Hallermann, S., & Stuart, G. J. (2006). Single Ih channels in pyramidal neuron dendrites: properties, distribution, and impact on action potential output. *J Neurosci*, 26(6), 1677-1687.

Korngreen, A., & Sakmann, B. (2000). Voltage-gated K<sup>+</sup> channels in layer 5 neocortical pyramidal neurones from young rats: subtypes and gradients. *J Physiol*, 525 Pt 3, 621-639.

- Krieg, T. D., Salinas, F. S., Narayana, S., Fox, P. T., & Mogul, D. J. (2013). PET-based confirmation of orientation sensitivity of TMS-induced cortical activation in humans. *Brain Stimul*, 6(6), 898-904.
- Kujirai, T., Caramia, M. D., Rothwell, J. C., Day, B. L., Thompson, P. D., Ferbert, A., . . . Marsden, C. D. (1993). Corticocortical inhibition in human motor cortex. *J Physiol*, 471, 501-519.
- Lai, H. C., & Jan, L. Y. (2006). The distribution and targeting of neuronal voltage-gated ion channels. *Nat Rev Neurosci*, 7(7), 548-562.
- Lang, S., Dercksen, V. J., Sakmann, B., & Oberlaender, M. (2011). Simulation of signal flow in 3D reconstructions of an anatomically realistic neural network in rat vibrissal cortex. *Neural Netw*, 24(9), 998-1011.
- Langevin, J. P., De Salles, A. A., Kosoyan, H. P., & Krahl, S. E. (2010). Deep brain stimulation of the amygdala alleviates post-traumatic stress disorder symptoms in a rat model. *J Psychiatr Res*, 44(16), 1241-1245.
- Laxton, A. W., & Lozano, A. M. (2012). Deep Brain Stimulation for the Treatment of Alzheimer Disease and Dementias. *World Neurosurg*.
- Lazzaro, Vincenzo Di, Ziemann, Ulf, & Lemon, Roger N. (2008). State of the art: Physiology of transcranial motor cortex stimulation. *Brain Stimul*, 1(4), 345-362.
- Limousin, P., Pollak, P., Benazzouz, A., Hoffmann, D., Le Bas, J. F., Broussolle, E., . . . Benabid, A. L. (1995). Effect of parkinsonian signs and symptoms of bilateral subthalamic nucleus stimulation. *Lancet*, 345(8942), 91-95.
- Lunde, M. E., Lee, E. K., & Rasmussen, K. G. (2006). Electroconvulsive therapy in patients with epilepsy. *Epilepsy Behav*, 9(2), 355-359.



- Magistretti, J., & Alonso, A. (1999). Biophysical properties and slow voltage-dependent inactivation of a sustained sodium current in entorhinal cortex layer-II principal neurons: a whole-cell and single-channel study. *J Gen Physiol*, 114(4), 491-509.
- Mainen, Z.F., & Sejnowski, T.J. (1996). Influence of dendritic structure on firing pattern in model neocortical neurons. *Nature*, 382, 363-366.
- Margoob, M. A., Ali, Z., & Andrade, C. (2010). Efficacy of ECT in chronic, severe, antidepressant- and CBT-refractory PTSD: an open, prospective study. *Brain Stimul*, 3(1), 28-35.
- Markram, H., Toledo-Rodriguez, M., Wang, Y., Gupta, A., Silberberg, G., & Wu, C. (2004). Interneurons of the neocortical inhibitory system. *Nat Rev Neurosci*, 5(10), 793-807.
- McConnell, K. A., Nahas, Z., Shastri, A., Lorberbaum, J. P., Kozel, F. A., Bohning, D. E., & George, M. S. (2001). The transcranial magnetic stimulation motor threshold depends on the distance from coil to underlying cortex: a replication in healthy adults comparing two methods of assessing the distance to cortex. *Biol Psychiatry*, 49(5), 454-459.
- McIntyre, C. C., Grill, W. M., Sherman, D. L., & Thakor, N. V. (2004). Cellular effects of deep brain stimulation: model-based analysis of activation and inhibition. *J Neurophysiol*, 91(4), 1457-1469.
- McNeal, D.R. (1976). Analysis of a Model for Excitation of Myelinated Nerve. *IEEE Trans Biomed Eng*, 23(4), 329-337.
- Merton, P. A., & Morton, H. B. (1980). Stimulation of the cerebral cortex in the intact human subject. *Nature*, 285(5762), 227-227.

- Mills, K. R., Boniface, S. J., & Schubert, M. (1992). Magnetic brain stimulation with a double coil: the importance of coil orientation. *Electroencephalogr Clin Neurophysiol*, 85(1), 17-21.
- Miniussi, C., Cappa, S. F., Cohen, L. G., Floel, A., Fregni, F., Nitsche, M. A., . . . Walsh, V. (2008). Efficacy of repetitive transcranial magnetic stimulation/transcranial direct current stimulation in cognitive neurorehabilitation. *Brain Stimul*, 1(4), 326-336.
- Miranda, P. C., Mekonnen, A., Salvador, R., & Ruffini, G. (2012). The electric field in the cortex during transcranial current stimulation. *Neuroimage*, 70C, 48-58.
- Miyawaki, Yoichi, & Okada, Masato. (2005). Mechanisms of spike inhibition in a cortical network induced by transcranial magnetic stimulation. *Neurocomputing*, 65–66(0), 463-468.
- Molnár, Zoltán, & Cheung, Amanda F. P. (2006). Towards the classification of subpopulations of layer V pyramidal projection neurons. *Neurosci Res*, 55(2), 105-115.
- Monai, H., Omori, T., Okada, M., Inoue, M., Miyakawa, H., & Aonishi, T. (2010). An analytic solution of the cable equation predicts frequency preference of a passive shunt-end cylindrical cable in response to extracellular oscillating electric fields. *Biophys J*, 98(4), 524-533.
- Moreines, J. L., McClintock, S. M., & Holtzheimer, P. E. (2011). Neuropsychologic effects of neuromodulation techniques for treatment-resistant depression: a review. *Brain Stimul*, 4(1), 17-27.
- Mori, F., Codeca, C., Kusayanagi, H., Monteleone, F., Buttari, F., Fiore, S., . . . Centonze, D. (2010). Effects of anodal transcranial direct current stimulation

on chronic neuropathic pain in patients with multiple sclerosis. *J Pain*, 11(5), 436-442.

Nadeem, Mohammad, Thorlin, Thorleif, Gandhi, Om P., & Persson, Mikael. (2003). Computation of Electric and Magnetic Stimulation in Human Head Using the 3-D Impedance Method. *IEEE Trans Biomed Eng*, 50(7), 900-907.

Nagarajan, S. S., Durand, D. M., & Warman, E. N. (1993). Effects of induced electric fields on finite neuronal structures: a simulation study. *IEEE Trans Biomed Eng*, 40(11), 1175-1188.

Neymotin, S. A., Jacobs, K. M., Fenton, A. A., & Lytton, W. W. (2011). Synaptic information transfer in computer models of neocortical columns. *J Comput Neurosci*, 30(1), 69-84.

Nummenmaa, A., McNab, J. A., Savadjiev, P., Okada, Y., Hamalainen, M. S., Wang, R., . . . Raij, T. (2014). Targeting of white matter tracts with transcranial magnetic stimulation. *Brain Stimul*, 7(1), 80-84.

Oswald, M. J., Tantirigama, M. L., Sonntag, I., Hughes, S. M., & Empson, R. M. (2013). Diversity of layer 5 projection neurons in the mouse motor cortex. *Front Cell Neurosci*, 7, 174.

Papadimitriou, G. N., Dikeos, D. G., Soldatos, C. R., & Calabrese, J. R. (2007). Non-pharmacological treatments in the management of rapid cycling bipolar disorder. *J Affect Disord*, 98(1-2), 1-10.

Park, Yong D. (2003). The effects of vagus nerve stimulation therapy on patients with intractable seizures and either Landau–Kleffner syndrome or autism. *Epilepsy & Behavior*, 4(3), 286-290.

Pashut, T., Wolfus, S., Friedman, A., Lavidor, M., Bar-Gad, I., Yeshurun, Y., & Korngreen, A. (2011). Mechanisms of magnetic stimulation of central nervous system neurons. *PLoS Comput Biol*, 7(3), e1002022.

Pelletier, S. J., & Cicchetti, F. (2015). Cellular and molecular mechanisms of action of transcranial direct current stimulation: evidence from in vitro and in vivo models. *Int J Neuropsychopharmacol*, *18*(2).

Perretti, A., De Rosa, A., Marcantonio, L., Iodice, V., Estraneo, A., Manganeli, F., . . . De Michele, G. (2011). Neurophysiological evaluation of motor corticospinal pathways by TMS in idiopathic early-onset Parkinson's disease. *Clin Neurophysiol*, *122*(3), 546-549.

Pinchuk, Dmitry, Vasserman, Maria, Sirbiladze, Konstantin, & Pinchuk, Olga. (2012). Changes of electrophysiological parameters and neuropsychological characteristics in children with psychic development disorders after transcranial direct current stimulation (tDCS). *Polish Annals of Medicine*, *19*(1), 9-14.

Plow, E. B., Pascual-Leone, A., & Machado, A. (2012). Brain stimulation in the treatment of chronic neuropathic and non-cancerous pain. *J Pain*, *13*(5), 411-424.

Popeo, D., & Kellner, C. H. (2009). ECT for Parkinson's disease. *Med Hypotheses*, *73*(4), 468-469.

Quartarone, A., Classen, J., Morgante, F., Rosenkranz, K., & Hallett, M. (2009). Consensus paper: use of transcranial magnetic stimulation to probe motor cortex plasticity in dystonia and levodopa-induced dyskinesia. *Brain Stimul*, *2*(2), 108-117.

Radman, T., Ramos, R. L., Brumberg, J. C., & Bikson, M. (2009). Role of cortical cell type and morphology in subthreshold and suprathreshold uniform electric field stimulation in vitro. *Brain Stimul*, *2*(4), 215-228, 228 e211-213.

Rahman, A., Reato, D., Arlotti, M., Gasca, F., Datta, A., Parra, L. C., & Bikson, M. (2013). Cellular effects of acute direct current stimulation: somatic and synaptic terminal effects. *J Physiol*, *591*(Pt 10), 2563-2578.

Rattay, F. (1999). The basic mechanism for the electrical stimulation of the nervous system. *Neuroscience*, *89*(2), 335-346.

Reddy, R., Horovitz, J., & Roslin, M. (2000). Chronic bilateral vagal nerve stimulation (VNS) changes eating behavior resulting in weight loss in a canine model. *Journal of the American College of Surgeons*, *191*(4(S1)), s27-s28.

Reis, Janine, Robertson, Edwin M., Krakauer, John W., Rothwell, John, Marshall, Lisa, Gerloff, Christian, . . . Cohen, Leonardo G. (2008). Consensus: Can transcranial direct current stimulation and transcranial magnetic stimulation enhance motor learning and memory formation? *Brain Stimul*, *1*(4), 363-369.

Ren, J. Q., Aika, Y., Heizmann, C. W., & Kosaka, T. (1992). Quantitative analysis of neurons and glial cells in the rat somatosensory cortex, with special reference to GABAergic neurons and parvalbumin-containing neurons. *Experimental Brain Research*, *92*(1), 1-14.

Reuveni, I., Friedman, A., Amitai, Y., & Gutnick, M. J. (1993). Stepwise repolarization from Ca<sup>2+</sup> plateaus in neocortical pyramidal cells: evidence for nonhomogeneous distribution of HVA Ca<sup>2+</sup> channels in dendrites. *J Neurosci*, *13*(11), 4609-4621.

Richter, M. M., Ehlis, A. C., Jacob, C. P., & Fallgatter, A. J. (2007). Cortical excitability in adult patients with attention-deficit/hyperactivity disorder (ADHD). *Neurosci Lett*, *419*(2), 137-141.

Rohland, B. M., Carroll, B. T., & Jacoby, R. G. (1993). ECT in the treatment of the catatonic syndrome. *J Affect Disord*, *29*(4), 255-261.

- Roth, Y., Pell, G. S., Chistyakov, A. V., Sinai, A., Zangen, A., & Zaaroor, M. (2014). Motor cortex activation by H-coil and figure-8 coil at different depths. Combined motor threshold and electric field distribution study. *Clin Neurophysiol*, *125*(2), 336-343.
- Rothkegel, H., Sommer, M., Paulus, W., & Lang, N. (2010). Impact of pulse duration in single pulse TMS. *Clin Neurophysiol*, *121*(11), 1915-1921.
- Rudy, B., & McBain, C. J. (2001). Kv3 channels: voltage-gated K<sup>+</sup> channels designed for high-frequency repetitive firing. *Trends Neurosci*, *24*(9), 517-526.
- Rusu, C. V., Murakami, M., Ziemann, U., & Triesch, J. (2014). A model of TMS-induced I-waves in motor cortex. *Brain Stimul*, *7*(3), 401-414.
- Salvador, R., Silva, S., Basser, P. J., & Miranda, P. C. (2011). Determining which mechanisms lead to activation in the motor cortex: a modeling study of transcranial magnetic stimulation using realistic stimulus waveforms and sulcal geometry. *Clin Neurophysiol*, *122*(4), 748-758.
- Schulz, R., Gerloff, C., & Hummel, F. C. (2013). Non-invasive brain stimulation in neurological diseases. *Neuropharmacology*, *64*, 579-587.
- Shimazu, H., Maier, M. A., Cerri, G., Kirkwood, P. A., & Lemon, R. N. (2004). Macaque ventral premotor cortex exerts powerful facilitation of motor cortex outputs to upper limb motoneurons. *J Neurosci*, *24*(5), 1200-1211.
- Siebner, H. R., Filipovic, S. R., Rowe, J. B., Cordivari, C., Gerschlager, W., Rothwell, J. C., . . . Bhatia, K. P. (2003). Patients with focal arm dystonia have increased sensitivity to slow-frequency repetitive TMS of the dorsal premotor cortex. *Brain*, *126*(12), 2710-2725.
- Srinivas, N., & Deb, Kalyanmoy. (1994). Multiobjective optimization using nondominated sorting in genetic algorithms. *Evol. Comput.*, *2*(3), 221-248.

Stokes, M. G., Chambers, C. D., Gould, I. C., English, T., McNaught, E., McDonald, O., & Mattingley, J. B. (2007). Distance-adjusted motor threshold for transcranial magnetic stimulation. *Clin Neurophysiol*, *118*(7), 1617-1625.

Strafella, A. P., Paus, T., Barrett, J., & Dagher, A. (2001). Repetitive transcranial magnetic stimulation of the human prefrontal cortex induces dopamine release in the caudate nucleus. *J Neurosci*, *21*(15), RC157.

Sturm, Volker, Lenartz, Doris, Koulousakis, Athanasios, Treuer, Harald, Herholz, Karl, Klein, Johannes Christian, & Klosterkötter, Joachim. (2003). The nucleus accumbens: a target for deep brain stimulation in obsessive-compulsive- and anxiety-disorders. *Journal of Chemical Neuroanatomy*, *26*(4), 293-299.

Suter, B. A., Migliore, M., & Shepherd, G. M. (2013). Intrinsic electrophysiology of mouse corticospinal neurons: a class-specific triad of spike-related properties. *Cereb Cortex*, *23*(8), 1965-1977.

Svirskis, G., Baginskas, A., Hounsgaard, J., & Gutman, A. (1997). Electrotonic measurements by electric field-induced polarization in neurons: theory and experimental estimation. *Biophys J*, *73*(6), 3004-3015.

Tasset, I., Medina, F. J., Jimena, I., Aguera, E., Gascon, F., Feijoo, M., . . . Tunez, I. (2012). Neuroprotective effects of extremely low-frequency electromagnetic fields on a Huntington's disease rat model: effects on neurotrophic factors and neuronal density. *Neuroscience*, *209*, 54-63.

Thickbroom, G. W. (2011). A model of the contribution of late I-waves to alpha-motoneuronal activation: implications for paired-pulse TMS. *Brain Stimul*, *4*(2), 77-83.

- Thielscher, A., & Kammer, T. (2002). Linking physics with physiology in TMS: a sphere field model to determine the cortical stimulation site in TMS. *Neuroimage*, *17*(3), 1117-1130.
- Thomson, A. M., West, D. C., Wang, Y., & Bannister, A. P. (2002). Synaptic connections and small circuits involving excitatory and inhibitory neurons in layers 2-5 of adult rat and cat neocortex: triple intracellular recordings and biocytin labelling in vitro. *Cereb Cortex*, *12*(9), 936-953.
- Tranchina, D., & Nicholson, C. (1986). A Model for the Polarization of Neurons by Extrinsically Applied Electric Field. *Biophys J*, *50*, 1139-1156.
- Traub, R. D., Contreras, D., Cunningham, M. O., Murray, H., LeBeau, F. E., Roopun, A., . . . Whittington, M. A. (2005). Single-column thalamocortical network model exhibiting gamma oscillations, sleep spindles, and epileptogenic bursts. *J Neurophysiol*, *93*(4), 2194-2232.
- Tsodyks, M., Pawelzik, K. , & Markram, H. . (1998). Neural Networks with Dynamic Synapses *Neural Computation*, *10*, 821-835.
- Tsubokawa, T., Katayama, Y., Yamamoto, T., Hirayama, T., & Koyama, S. (1991). Chronic motor cortex stimulation for the treatment of central pain. *Acta Neurochir Suppl (Wien)*, *52*, 137-139.
- Vacher, H., Mohapatra, D. P., & Trimmer, J. S. (2008). Localization and targeting of voltage-dependent ion channels in mammalian central neurons. *Physiol Rev*, *88*(4), 1407-1447.
- Vanneste, S., Langguth, B., & De Ridder, D. (2011). Do tDCS and TMS influence tinnitus transiently via a direct cortical and indirect somatosensory modulating effect? A combined TMS-tDCS and TENS study. *Brain Stimul*, *4*(4), 242-252.



- Vucic, S., Cheah, B. C., Yiannikas, C., & Kiernan, M. C. (2011). Cortical excitability distinguishes ALS from mimic disorders. *Clin Neurophysiol*, *122*(9), 1860-1866.
- Wagner, Tim, Fregni, Felipe, Eden, Uri, Ramos-Estebanez, Ciro, Grodzinsky, Alan, Zahn, Markus, & Pascual-Leone, Alvaro. (2006). Transcranial magnetic stimulation and stroke: A computer-based human model study. *NeuroImage*, *30*(3), 857-870.
- Wagner, Tim, Fregni, Felipe, Fecteau, Shirley, Grodzinsky, Alan, Zahn, Markus, & Pascual-Leone, Alvaro. (2007). Transcranial direct current stimulation: A computer-based human model study. *NeuroImage*, *35*(3), 1113-1124.
- Wang, Y. , Gupta, A. , Toledo-Rodriguez, M. , Wu, C.Z., & Markram, H. (2002). Anatomical, physiological, Molecular and Circuit Properties of Nest Basket Cells in the Developing Somatosensory Cortex. *Cerebral Cortex*, *12*, 395-410.
- Wassermann, E. M., & Zimmermann, T. (2012). Transcranial magnetic brain stimulation: therapeutic promises and scientific gaps. *Pharmacol Ther*, *133*(1), 98-107.
- Weiler, N., Wood, L., Yu, J., Solla, S. A., & Shepherd, G. M. (2008). Top-down laminar organization of the excitatory network in motor cortex. *Nat Neurosci*, *11*(3), 360-366.
- Werhahn, K. J., Fong, J. K. Y., Meyer, B. U., Priori, A., Rothwell, J. C., Day, B. L., & Thompson, P. D. (1994). The effect of magnetic coil orientation on the latency of surface EMG and single motor unit responses in the first dorsal interosseous muscle. *Electroencephalogr Clin Neurophysiol*, *93*(2), 138-146.

Wongsarnpigoon, A., & Grill, W. M. (2012). Computer-based model of epidural motor cortex stimulation: effects of electrode position and geometry on activation of cortical neurons. *Clin Neurophysiol*, *123*(1), 160-172.

Wu, H., Van Dyck-Lippens, P. J., Santegoeds, R., van Kuyck, K., Gabriels, L., Lin, G., . . . Nuttin, B. (2012). Deep-Brain Stimulation for Anorexia Nervosa. *World Neurosurg*.

Yamamoto, T., & Katayama, Y. (2005). Deep brain stimulation therapy for the vegetative state. *Neuropsychol Rehabil*, *15*(3-4), 406-413.

Yi, G. S., Wang, J., Wei, X. L., Tsang, K. M., Chan, W. L., Deng, B., & Han, C. X. (2014). Exploring how extracellular electric field modulates neuron activity through dynamical analysis of a two-compartment neuron model. *J Comput Neurosci*, *36*(3), 383-399.

Zhong, X. L., Yu, J. T., Zhang, Q., Wang, N. D., & Tan, L. (2011). Deep brain stimulation for epilepsy in clinical practice and in animal models. *Brain Res Bull*, *85*(3-4), 81-88.

Ziemann, U., Wahl, M., Hattingen, E., & Tumani, H. (2011). Development of biomarkers for multiple sclerosis as a neurodegenerative disorder. *Prog Neurobiol*, *95*(4), 670-685.

## **List of publications**

### **International journal articles**

Wu, Tiecheng, Fan, Jie, Lee, Kim Seng, & Li, Xiaoping. (2015). Cortical neuron activation induced by electromagnetic stimulation: a quantitative analysis via modelling and simulation. *Journal of Computational Neuroscience*, 1-14.

Fan, J., Li, J., Li, J., Wu, T., & Li, X. (2015). Magnetic Field Projector for Deep Brain Stimulation. *Magnetics, IEEE Transactions on, PP(99)*, 1-1.

Li, X. P., Xia, Q., Qu, D., Wu, T. C., Yang, D. G., Hao, W. D., . . . Li, X. M. (2014). The Dynamic Dielectric at a Brain Functional Site and an EM Wave Approach to Functional Brain Imaging. *Sci. Rep.*, 4.

Wang, Y., Ng, W. C., Ng, K. S., Yu, K., Wu, T., & Li, X. (2015). An electroencephalography network and connectivity analysis for deception in instructed lying tasks. *PLoS One*, 10(2), e0116522.

Li, Z., Yang, D., Hao, W., Wu, T., Wu, S., & Li, X. (2015). A novel technique for micro-hole forming on skull with the assistance of ultrasonic vibration. *J Mech Behav Biomed Mater*, 57, 1-13.

Ye, Yan, Li, Xiaoping, Wu, Tiecheng, Li, Zhe, & Xie, Wenwen. (2015). Material and physical model for evaluation of deep brain activity contribution to EEG recordings. *Functional Materials Letters*, 08(03), 1540003.

### **International conference papers**

Wu, Tiecheng, Fan, Jie, Lee Kim, Seng, Li, Xiaoping, & Wilder-Smith, E. P. V. (2013, 6-8 Nov. 2013). *Modeling of membrane potential dynamics induced by electromagnetic stimulation*. Paper presented at the Neural Engineering (NER), 2013 6th International IEEE/EMBS Conference; 2013 6-8 Nov. 2013:243-246.

Fan, Jie, Wu, Tiecheng, Ye, Yan, Bui Ha, Duc, & Li, Xiaoping. (2013, 6-8 Nov. 2013). *A magnetic field projector for deep brain modulation*. Paper presented at the Neural Engineering (NER), 2013 6th International IEEE/EMBS Conference; 2013 6-8 Nov. 2013:1214-1217.

Wang, Yue, Ng Wu, Chun, Ng Khoon, Siong, Wu, Tiecheng, & Li, Xiaoping. (2013, 6-8 Nov. 2013). *An EEG source localization and connectivity study on deception of autobiography memories*. Paper presented at the Neural Engineering (NER), 2013 6th International IEEE/EMBS Conference; 2013 6-8 Nov. 2013:468-471.

Fan J, Wu T, Lee KS, Li X. *Magnetically induced deep brain stimulation of neuronal firing for pain relief*. Engineering in Medicine and Biology Society (EMBC), 2012 Annual International Conference of the IEEE; 2012 Aug. 28 2012-Sept. 1 2012: 731-734.